

**A BROAD SPECTRUM NEUTRON SPECTROMETER UTILIZING A HIGH
ENERGY BONNER SPHERE EXTENSION**

A Thesis
Presented to
The Academic Faculty

by

Eric A. Burgett

In Partial Fulfillment
of the Requirements for the Degree
Master of Science in the
School of Nuclear Engineering

Georgia Institute of Technology
May 2008

**A BROAD SPECTRUM NEUTRON SPECTROMETER UTILIZING A HIGH
ENERGY BONNER SPHERE EXTENSION**

Approved by:

Dr. Nolan E. Hertel, Advisor
School of Mechanical Engineering
Georgia Institute of Technology

Dr. Rebecca Howell
School of Radiation Oncology
University of Texas M.D. Anderson Cancer Center

Dr. Chris Wang
School of Mechanical Engineering
Georgia Institute of Technology

Date Approved: 3/28/2008

ACKNOWLEDGEMENTS

I would like to thank first, Dr. Nolan Hertel. Without his patient teaching and motivation, I would have never learned anything about Bonner Spheres, or neutron spectroscopy. For his ever critical eye that continues to drive me to work for near perfection. Lastly, for his outlook and teachings on life, shaping the person I am today. None of this would have been possible without his support.

Next I would like to thank Dr. Rebecca Howell. Who constantly was a voice of reason, and a great motivator and who supported this project emotionally and financially, who never lost faith in the project and was always supportive even when the beam would go down and nothing would work correctly. I greatly appreciate your support and friendship through the entire project.

I would like to thank Steven Kry, Zhonglu Wang, Christina LoBracco, and Jonathan Rosenfield. Without your help, the first measurement trip would have been much more difficult and boring. I would like to thank Jesson Hutchinson and Ryan Lorio for putting up with me during the second measurement trip. You guys made the second trip much more fun. To the LANL support staff, in particular Art Bridge, Dr. Steve Wender, and Dr. Nikolaos Fotiadis, who without their support and expertise, none of the measurements would have been possible.

Lastly, and most importantly I would like to thank Angel, my loving wife. She supported me during the trips to Los Alamos for weeks on end, the long nights processing data, and the stress of grad school.

TABLE OF CONTENTS

	Page
ACKNOWLEDGEMENTS	iv
LIST OF TABLES	vii
LIST OF FIGURES	viii
LIST OF EQUATIONS	xvi
LIST OF SYMBOLS AND ABBREVIATIONS	xviii
SUMMARY	xx
CHAPTER 1 INTRODUCTION	1
Background	1
Bonner Sphere Detection Systems with Passive Detectors	4
Disadvantages of Bonner Sphere Measurement Systems	6
Methods for Improving Energy Response above 20-MeV	7
High Energy Single Detector Rem Meters	8
High Energy Neutron Spectroscopy Systems	10
Current Work – Bonner Sphere Extension for High Energy Structure	11
CHAPTER 2 THEORY	12
Standard Bonner Sphere Response	12
Extended Bonner Spheres for Increased Response above 20MeV	14
Mathematical Deconvolution of Data Measured with Moderators	16
CHAPTER 3 DETECTOR DESIGN	19
Bonner Sphere System with Active Scintillator	19
Bonner Sphere System with Passive Gold Foil	22

High Energy Bonner Sphere Extension	28
Ancillary Equipment Used at LANSCE	35
CHAPTER 4 DETECTOR MODELING	39
Detector Modeling	39
Experimental Setup Modeling	57
CHAPTER 5 EXPERIMENTAL VALIDATION	63
General Experimental Layout	63
The Active LiI(Eu) Detector System	67
The Passive Gold Foil System	69
The HPGe Detector Setup	70
Beam Monitor	73
CHAPTER 6 EXPERIMENTAL RESULTS	78
CHAPTER 7 CONCLUSIONS	97
CHAPTER 8 FUTURE WORK ⁹⁸	
APPENDIX A GOLD FOIL RESPONSE DATA	101
Z-Directional Responses	101
YZ-Directional Responses	105
APPENDIX B LiI(Eu) DETECTOR RESPONSE DATA	111
Z-Directional Responses	111
YZ-Directional Responses	115
APPENDIX C FLUENCE RATE NORMALIZATION	121
APPENDIX D GOLD FOIL RESPONSE COMPARISONS	123
REFERENCES	126

LIST OF TABLES

	Page
Table 1. Air gap spacing for the different spherical shell sets.	41
Table 2. Dimensions of the top spherical shells for the BSE. The small assemblies are the ID sizes of 3, the large assemblies are the 5 inch labels	42
Table 3 Dimensions of the bottom spherical shells for the BSE.	42
Table 4. Physical properties of the spherical shells	43
Table 5. The accelerator operating parameters for the two measurement trips	58
Table 6. The measured mass and ^{198}Au production rate of the gold foils for the unfiltered beam.	80
Table 7. The neutron fluence rates per fission count for the MCNPX model, the unfolded neutron spectrum, and the TOF spectrum.	91
Table 8. The neutron fluence rates per proton for the MCNPX model, the unfolded neutron spectrum, and the TOF spectrum.	92
Table 9. Shown is the ratio of the TOF neutron fluence rate in each bin to the fluence rate of the unfolded spectra.	93

LIST OF FIGURES

	Page
Figure 1. The cross section plot of ${}^6\text{Li}$ for the ENDF-VII evaluation. Shown are the (n,xa), (n,xt) and (n,g) reactions. The x represents any other particle emission in addition to the alpha, or triton.	2
Figure 2. Bonner Sphere Responses for a standard BSS ⁹ .	4
Figure 3. TLD-Bases Bonner System	5
Figure 4. A simplified diagram for the moderate and capture detector method.	14
Figure 5. A simplified diagram for the downscatter, moderate, and capture detector method.	15
Figure 6. A cutaway diagram of the LiI(Eu) detector assembly showing the Plexiglas light pipe and PMT.	20
Figure 7. An example LiI(Eu) spectrum.	21
Figure 8. HPGe detector setup with lead shielding cave and NIM modules for running the detector.	27
Figure 9. A sample gamma ray spectra from the HPGe detector.	28
Figure 10. A diagram of the small and large spherical shell assemblies.	29
Figure 11. A CAD representation of the preliminary BSE design is shown with the shells opening vertically.	30
Figure 12. A CAD representation of the preliminary BSE design is shown with the shells opening vertically. Here a shell set is shown closing to show the alignment of the BSE.	30

Figure 13. The spherical shells during the fabrication process at the Georgia Tech Research Institute (GTRI) machine shop.	31
Figure 14. The 5” spherical shells (large assembly) in early production stages. The first locking lip can be seen cut into the surface.	32
Figure 15. Smelting lead and ladling it into the shell.	34
Figure 16. The beam profile of the typical LANSCE WNR beam as a function of time	36
Figure 18. The LiI(Eu) detector models from MCNPX in the standard poly sphere set. On the left is a closeup of the LiI(Eu) crystal. The image is not to scale.	40
Figure 19. Three inch and five inch tungsten spheres showing the small air gap.	41
Figure 20. The BSE polyethylene holder system. Red is polyethylene, green is the fill material, and yellow is the aluminum.	44
Figure 21. Beam orientation for the generation of the BSS and BSE response matrices.	45
Figure 22. The response of the original BSS system is shown for the Y-direction neutron source.	47
Figure 23. The response of the BSE polyethylene spheres and polyethylene holder is shown for the Y-direction neutron irradiation.	48
Figure 24. The small assembly (three inch inner sphere) BSE spheres gold foil detector response for the Y-direction neutron source.	49
Figure 25. The large assembly (five inch inner sphere) BSE spheres gold foil detector response for the Y-direction neutron source.	50
Figure 26. The BSE gold foil detector system is shown which utilizes both the 3” and 5” shells simultaneously for the Y-direction neutron source.	51

Figure 27. The LiI(Eu) Detector response for the original BSS for the Y-direction neutron field.	52
Figure 28. The response of the BSE polyethylene spheres LiI(Eu) detector is shown for the Y-direction neutron irradiation.	53
Figure 29. The response of 5" BSE (the large set) spheres LiI(Eu) detector is shown for the Y-direction neutron irradiation.	54
Figure 30 The response of 3" BSE (the small set) spheres LiI(Eu) detector is shown for the Y-direction neutron irradiation.	55
Figure 31 The BSE LiI(Eu) detector system is shown which utilizes both the 3" and 5" shells simultaneously for the Y-direction neutron source.	56
Figure 32. The detailed LANSCE tungsten target.	57
Figure 33. Calculated (simplified model) and experimental neutron spectra from LANSCE.	59
Figure 34. Calculated (simplified model) and experimental neutron spectra from LANSCE blown up to highlight the region above 100 keV.	60
Figure 35. Calculated (simplified model) and experimental neutron spectra from LANSCE plotted with collapsed energy groups. The error bars are smaller than the figures.	61
Figure 36. The results of the detailed MCNPX model neutron spectrum at the 86.6 meter experiment location.	62
Figure 37. The experimental LANSCE facility in Los Alamos NM.	63
Figure 38. The experimental facility layout of the WNR LANSCE facility.	64
Figure 39. Flight path 15R facility layout schematic.	65

Figure 40. Experimental setup schematic for the equipment in the 90 meter experiment station	65
Figure 41. Experimental setup for validating the BSE and BSS systems at the 90 m experiment station on the 15 degree right flight path.	66
Figure 42. A LiI(Eu) measured spectra. The area in the red box is the marked ROI. The counts are displayed on both a log scale (pink) and linear scale (blue).	68
Figure 43. The wooden holder set for the YZ-direction which makes the beam incident on the detector at 45 degrees.	69
Figure 44. The energy calibration curve for the HPGe detector used on the WNR LANSCE trips.	70
Figure 45. An example HPGe spectrum from the counting of the gold foils following the irradiation of the 5" tungsten covered sphere. The counts are plotted on a log scale	72
Figure 46. An example beam monitor plot used to normalize the beam up time for the activation measurements.	73
Figure 47. The July 2007 spatial neutron flux profile. The pixel values ranged from 0 to 255.	75
Figure 48. The September 2007 neutron flux profile image.	76
Figure 49. ^{198}Au production rate for the different spheres in the Y-direction irradiation configuration.	79
Figure 50. A comparison between the spectral unfoldings with the the flat and lethergy starting spectra and the best approximation spectrum.	81
Figure 51. A comparison of the calculated and measured neutron fluxes as well as the unfolded neutron flux.	83

Figure 52. A comparison of the calculated and measured neutron fluxes as well as the unfolded neutron flux with respect to fission counts.	84
Figure 53. A comparison of the calculated and measured neutron fluxes as well as the unfolded neutron flux shown blown up from Figure 51.	85
Figure 54.. A comparison of the calculated and measured neutron fluxes as well as the unfolded neutron flux shown blown up from Figure 51 with respect to the number of fission counts.	86
Figure 55. A comparison between spectral unfolding of only the original BSS and the new system with the BSE contributions compared.	87
Figure 56. A comparison between spectral unfolding of only the original BSS and the new system with the BSE contributions compared shown with respect to fission counts.	88
Figure 57. A blown up version of Figure 55 zoomed in on the energies above 100 keV.	89
Figure 58. A blown up version of Figure 55 zoomed in on the energies above 100 keV plotted with respect to the number of fission counts.	90
Figure 59. A comparison of the filtered and unfiltered neutron beams measured by the TOF system.	94
Figure 60. 32.4 cm of poly filtration in the WNR beam. Shown is the TOF, a flat starting spectrum and the best approximation unfoldings.	95
Figure 61. 32.4 cm of poly filtration in the WNR beam blown up above 100 keV. Shown is the TOF, a flat starting spectrum and the best approximation unfoldings.	96

Figure 62. 12” sphere comparison for heavy water, light water and poly spheres. These spectra have the unique feature that they do not tail up at the high end of the spectra.	99
Figure 63. Preliminary responses for small acrylic moderating spheres covering gold foils.	100
Figure 64. The response of the original BSS system is shown for the Z-direction neutron source.	101
Figure 65. The response of the BSE polyethylene spheres and polyethylene holder is shown for the Z-direction neutron irradiation.	102
Figure 66. The small assembly (three inch inner sphere) BSE spheres gold foil detector response for the Z-direction neutron source.	103
Figure 67. The large assembly (five inch inner sphere) BSE spheres gold foil detector response for the Z-direction neutron source.	104
Figure 68. The BSE gold foil detector system is shown which utilizes both the 3” and 5” shells simultaneously for the Z-direction neutron source.	105
Figure 69. The response of the original BSS system is shown for the YZ-direction neutron source.	106
Figure 70. The response of the BSE polyethylene spheres and polyethylene holder is shown for the YZ-direction neutron irradiation.	107
Figure 71. The small assembly (three inch inner sphere) BSE spheres gold foil detector response for the YZ-direction neutron source.	108
Figure 72. The large assembly (five inch inner sphere) BSE spheres gold foil detector response for the YZ-direction neutron source.	109

Figure 73. The BSE gold foil detector system is shown which utilizes both the 3” and 5” shells simultaneously for the Z-direction neutron source.	110
Figure 74. The response of the original BSS system is shown for the Z-direction neutron source for the LiI(Eu) detector.	111
Figure 75. The response of the BSE polyethylene spheres and active LiI(Eu) detector is shown for the Z-direction neutron irradiation.	112
Figure 76. The small assembly (three inch inner sphere) BSE spheres active LiI(Eu) detector response for the Z-direction neutron source.	113
Figure 77. The large assembly (five inch inner sphere) BSE spheres active LiI(Eu) detector response for the Z-direction neutron source.	114
Figure 78. The BSE LiI(Eu) detector system is shown which utilizes both the 3” and 5” shells simultaneously for the Z-direction neutron source.	115
Figure 79. The response of the original BSS system is shown for the YZ-direction neutron source with the active LiI(Eu) detector.	116
Figure 80. The response of the BSE polyethylene spheres and active LiI(Eu) detector is shown for the YZ-direction neutron irradiation.	117
Figure 81. The small assembly (three inch inner sphere) BSE spheres active LiI(Eu) detector response for the YZ-direction neutron source.	118
Figure 82. The large assembly (five inch inner sphere) BSE spheres active LiI(Eu) detector response for the YZ-direction neutron source.	119
Figure 83. The BSE active LiI(Eu) detector system is shown which utilizes both the 3” and 5” shells simultaneously for the Z-direction neutron source.	120
Figure 84. The ratio of the angular response of the low energy spheres.	123

Figure 85. The ratio of the angular response of the intermediate energy spheres.	124
Figure 86. The ratio of the angular response of the high energy spheres.	125

LIST OF EQUATIONS

	Page
Equation 1	16
Equation 2	17
Equation 3. The production rate of isotope x during irradiation.	23
Equation 4 The differential equation describing the time rate of change of the number of atoms of isotope x during irradiation.	23
Equation 5. The decay constant λ as a function of the isotopes half life in seconds.	23
Equation 6. The number of radioactive atoms as a function of time during irradiation.	23
Equation 7. The production rate as a function of time during irradiation in units of activity per second.	24
Equation 8. The activity at some arbitrary time t' after irradiation.	24
Equation 9. The expected count rate at the detector at time t' .	24
Equation 10. the activity at counting time as a function of count rates.	25
Equation 11. The production rate of a given isotope as a function of counts on a gamma spectroscopy system. The m in the denominator is the mass of the foil.	25
Equation 12. The activity at a given time t' for a series production and decay	25
Equation 13. The energy dependant fluence rate per unit area.	122
Equation 14. The energy dependant fluence rate per unit area per fission count.	122
Equation 15. The energy dependant fluence rate per unit area per fission count per unit lethargy.	122
Equation 16. The energy dependant fluence rate per unit area per proton.	122

Equation 17. The energy dependant fluence rate per unit area per proton per unit lethargy.

122

LIST OF SYMBOLS AND ABBREVIATIONS

HPGe	High Purity Germanium Detector
BSS	Bonner Sphere Spectrometer
BSE	Bonner Sphere Extension
TLD	Thermal Luminescent Dosimeter
LANL	Los Alamos National Lab
LANSCE	Los Alamos Neutron Science Center
GeV	Measure of energy in electron volts times 10^9
MeV	Measure of energy in electron volts times 10^6
keV	Measure of energy in electron volts times 10^3
eV	Measure of energy in electron volts
ΔU	Per unit lethargy
LiI(Eu)	The Lithium Iodide Europium doped scintillator
PTB	Physikalisch-Technische Bundesanstalt, the national institute for engineering sciences in Germany.
PMT	Photomultiplier Tube

NIST	National Institute of Standards and Technology
RBE	Relative Biological Effectiveness
\dot{P}_x	Production rate of isotope X.
ENDF	Evaluated Nuclear Data File – version number in roman numerals
MCA	Multi Channel Analyzer
NORM	Naturally Occurring Radioactive Material
GTRI	Georgia Tech Research Institute
TOF	Time Of Flight

SUMMARY

A high energy Bonner Sphere Spectrometer (BSS) and Bonner Sphere Extension (BSE) has been designed, built and tested as a new neutron spectrometer. This system is based on a commercially available detector system, and extends its functionality over 13 decades in energy. The method to produce this detector system, model the detector system, and test the new detector system is provided herein. This system makes use of both active (Li(Eu)) and passive (gold foil) detectors. The system has a nearly isotropic angular response that is capable of measuring many different neutron fields. Using the passive detector, high intensity and pulsed neutron fields can be measured. The active detector can be used in lower intensity neutron fields as well as pulsed neutron fields. The system utilizes a small assembly and large assembly with lead, copper, and tungsten dwonscatter filling materials. The small assembly is designed to fit over the standard 3” Bonner sphere, whereas the large assembly fits over the 5” Bonner sphere. A total of thirty two different detector configurations are able to be made with the current system and an additional five detector configurations were modeled but not fabricated. This system produces energy response structure from below 1 eV to above 1 GeV neutron energies. The energy response matrices were calculated in MCNPX v2.6e, the latest available beta test version of the code for the “as built” spectrometers. The system was tested at the Weapons Neutron Research (WNR) Los Alamos Neutron Science Center (LANSCE) high energy neutron facility. MCNPX models were made of the test facility. Spectral measurements were made and unfolded. The data from the unfolded neutron

spectra agree reasonably with the available experimental time of flight (TOF) data and the MCNPX modeled data.

CHAPTER 1

INTRODUCTION

Background

Since neutrons are neutral particles, they are detected by secondary charged particles created in neutron nucleus reactions. Neutron fields are present over a broad range of applications ranging from nuclear reactors to spent nuclear fuel storage to unwanted contamination of high energy x-ray and proton radiotherapy beams. These neutron fields each have unique energy spectra that range over several orders of magnitude. Neutrons produced in reactors have energies ranging from fractions of eV to a maximum of approximately 17-MeVⁱ. Neutrons produced in high energy x-ray radiation therapy facilities can have energies up to the energy of the accelerator which can be as high as 25-MeVⁱⁱ. These neutrons resemble a Gaussian evaporation spectrum. Neutrons produced in high energy proton accelerators span the largest energy range with a maximum energy determined by the proton beam which typically is 80-MeV to 250-MeV in radiotherapy facilities and higher at high energy facilities. These wide energy ranges result in unique challenges for accurate neutron spectral measurements. Neutron spectrum measurements are essential to determine the effects of the neutrons regardless of their energies. For example, radiation protection quantities and quality factors used for evaluating neutron dose to biological tissues are energy dependent.

Bonner Sphere Detection Systems with Active Detectors

Many neutron detectors are highly sensitive to thermal neutrons but have very low sensitivity to higher energy neutrons. The higher energy neutrons can be moderated to low energies and detected using thermal neutron detectors. By using different sized moderators the system can be used to reconstruct neutron spectra. Moderating techniques are necessary because existing detectors have large neutron absorption cross sections at thermal energies and significantly smaller absorption cross sections at higher energies, see Figure 1.

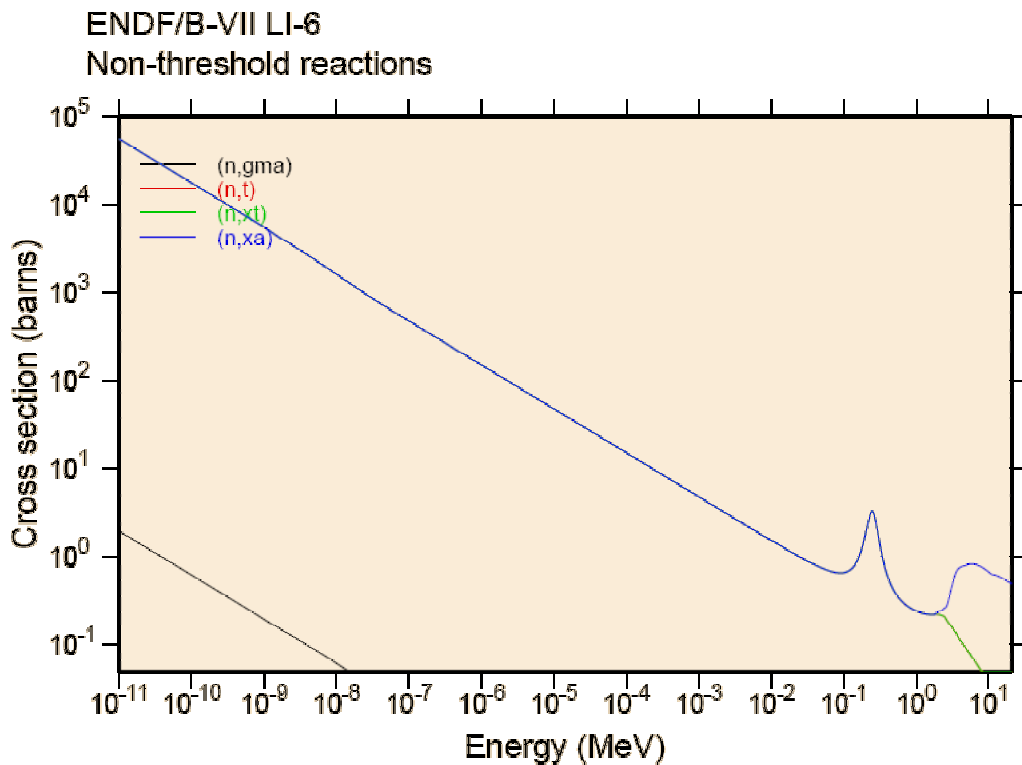


Figure 1. The cross section plot of ${}^6\text{Li}$ for the ENDF-VII evaluationⁱⁱⁱ. Shown are the (n,xa), (n,xt) and (n,g) reactions. The x represents any other particle emission in addition to the alpha, or triton.

A moderated thermal neutron detector that has found widespread use was first introduced in 1960 by Bramblet, Ewing, and Bonner^{iv}. The system used a ${}^6\text{LiI}$ detector in a series of polyethylene moderating spheres, or Bonner spheres, ranging in size from 2 to 12 inches in diameter. The spherical geometry of the Bonner spheres generally yields an isotropic response. The system works on the moderate and capture method of detection. Incident neutrons interact in the hydrogenous polyethylene surrounding the thermal neutron detector through elastic scattering with hydrogen and carbon as well as inelastic scattering off of hydrogen. As the neutrons scatter from the hydrogen and carbon they lose energy and thermalize in the material and/or leak out of the moderator. Some of these moderated thermal neutrons interact with in the detector via the ${}^6\text{Li}(n,\alpha){}^3\text{H}$ thermal neutron absorption. By varying the thickness of this moderating material, the detector sensitivity changes as a function of neutron energy.

In the original BSS design, the scintillator was selected to have a small diameter and small volume to minimize the gamma ray response^{iv}. The current commercially available designs^{v,vi} have been optimized to increase the surface to volume ratio of the lithium iodide scintillator. This is because most of the neutrons are absorbed in the outer few millimeters of scintillator. Other designs use a ${}^3\text{He}$ gas filled spherical detector to minimize the gamma contribution to the count rate^{vii}.

Bonner Sphere data does not directly provide neutron spectra. The energy dependence of each detector-moderator combination results in a different response to a given neutron energy spectrum. A deconvolution (“unfolding”) of the Bonner Sphere counts is required to determine an appropriate neutron spectrum. The response of each Bonner sphere and detector combination can be calculated and used to unfold the

measured data to provide an estimate of the spectrum. Many different evaluations of the response have been calculated with the responses binned into many energy groups from 31 groups^{viii} to 174 groups^{ix}. One such response by Hertel and Davidson^{ix} is shown in Figure 2.

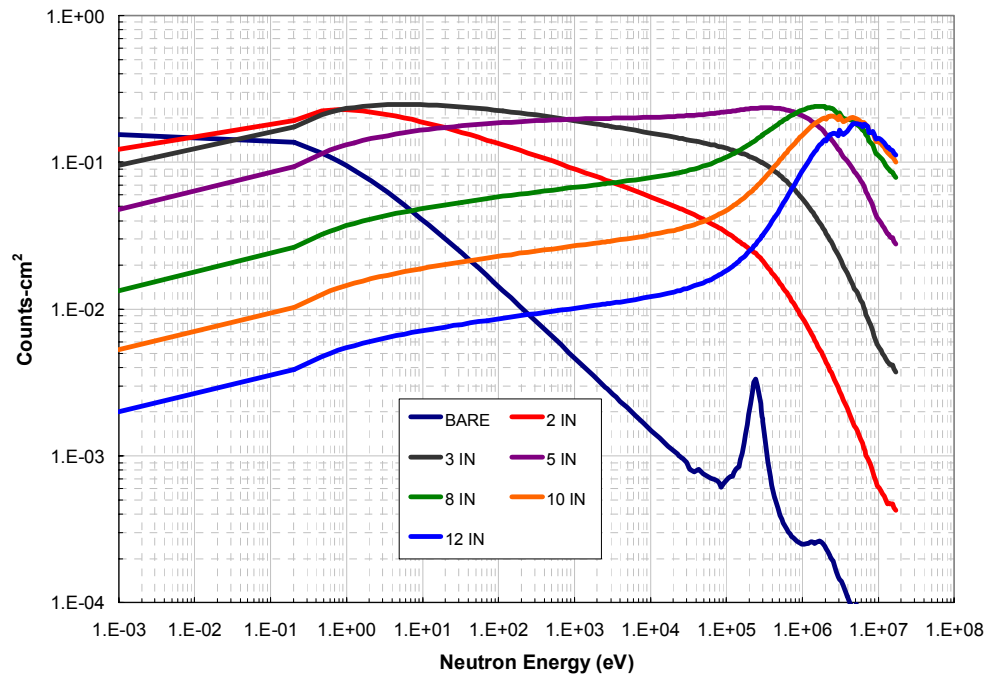


Figure 2. Bonner Sphere Responses for a standard BSS^{ix}.

Bonner Sphere Detection Systems with Passive Detectors

Active detectors are susceptible to pulse pile-up especially in intense or pulsed fields. In these situations passive detection techniques are preferred. Thermoluminescent Detectors (TLDs) and activation foils have both been used with Bonner sphere systems(BSS). TLDs are especially useful for measurements in n fields with high gamma contaminations. Two different types of TLDs are utilized for these measurements, one sensitive to both photons and thermal neutrons and the other only sensitive to photons. The neutron component can then be determined by the difference in

the response in the two types of materials. The TLDs used for these types of measurements are made of LiF. The thermal neutron response depends on the isotopic content of Li. ${}^6\text{Li}$ has a thermal neutron (n,α) reaction cross section of 940 barnsⁱⁱⁱ. LiF TLDs enriched to 95.62% ${}^6\text{Li}$ isotope are referred to as TLD-600s. LiF TLDs enriched to 99.93% ${}^7\text{Li}$ isotope are referred to as TLD-700s^x. Both TLD-700s and TLD-600s are sensitive to gamma radiation and since they have the same atomic number, they should have equivalent gamma-ray responses.

A TLD-based BSS was developed by Sweezy et al.^{xi} at the Georgia Institute of Technology. The system uses a TLD holder which has dimensions similar to the ${}^6\text{LiI}$ scintillator, see Figure 3.

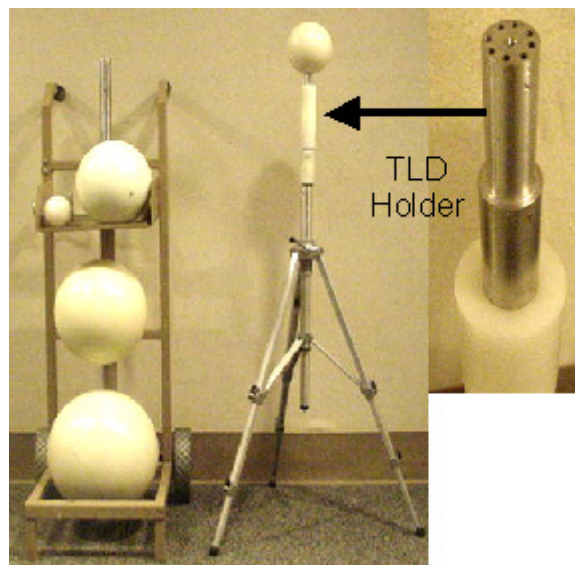


Figure 3. TLD-Bases Bonner System

Systems which use TLDs have two main limitations: (1) extended processing time and (2) saturation at doses in excess of 10-Gy combined neutron and gamma dose. Passive detectors which are not susceptible to saturation at high neutron doses are

activation foils. BSSs have been designed on foil activation methods using gold or indium foils^{xii,xiii}. These systems have the distinct advantage that they can be completely insensitive to photon radiation. Wang et al. further modified the Sweezy TLD system to activation foils, specifically ^{197}Au . ^{197}Au has a reasonably high thermal neutron cross-section and is activated via $^{197}\text{Au}(n,\gamma)^{198}\text{Au}$, which decays in a β - γ cascade with emission of 411 keV γ -rays ($T_{1/2} = 2.7$ days). The 411-keV gamma-ray photopeak can be measured using a high-purity germanium detector (HPGe). This system was validated in NIST traceable reference neutron fields and shows good agreement^{xiv}. When using a HPGe detector to count activation foils, they can become completely insensitive to photon radiation. This is due to the unique reaction pathway. It is possible for the foil to undergo exotic reactions such as (γ,n) , $(n,2n)$, $(n,3n)$, (n,p) etc. however, each pathway produces a unique progeny. With careful selection of activation foils, particularly those who have only one naturally occurring isotope, each pathway is unique and each progeny can be uniquely identified by its emitted photon radiation.

Disadvantages of Bonner Sphere Measurement Systems

While there are many advantages to BSSs, there are some limitations. Since each spheres sensitivity peaks at a different energy, they become less efficient at detecting some neutron energies. As the moderator thickness increases, the probability of capture in the LiI(Eu) crystal decreases because leakage increases. Because of this additional leakage, the larger spheres have decreasing efficiencies, with the 12” sphere having an efficiency of $\sim 0.1\%$ at 20-MeV^{xv} which can be seen in Figure 2. Higher efficiencies can be achieved with a proton recoil detector to measure neutron scatters off of hydrogen. However, proton recoil detectors are also susceptible to angular dependence. A second

limitation of BSSs is low resolution through the entire energy spectrum, particularly in the 1eV to 100 keV region. In this region, there is no unique response structure to resolve spectral data. In this region, unless outside constraints are imposed on the unfolding process, artifacts from the similar response matrices will remain producing what is commonly referred to as the “Bonner Dip”. Work had been done to produce a spherical shell detector made from ^{10}B that would add structure to this region for unfolding but fabrication was cost prohibitive^{xvi}. Another disadvantage of the traditional neutron BSS system is the loss of structure and decreased sensitivity above 20-MeV. The large standard Bonner spheres (10” and 12”) all respond in a similar fashion to neutron energies above 20-MeV which can be seen in Figure 2. Additionally, the responses are very low at these high energies. Since there is no unique information above this level, no unique information can be unfolded from the responses of the detectors.

Methods for Improving Energy Response above 20-MeV

There are three main methods for improving the sensitivity to neutrons above the 20-MeV sensitivity decline. The first is by the use of threshold reactions in materials are used to produce greater response and structure in this region to be used in unfolding. Historically this was one of the first methods for detecting neutrons above 1 MeV^{xvii}. For threshold reaction detectors, isotopes are selected on the basis of creation of a radioactive isotope that has a half life long enough for so it can be counted after removal from the field but short enough that a high activity can be achieved in a reasonable amount of time. In addition, the isotope should be selected such that it has a large cross section for the reaction and that the radioactive product emits an easily detected ionizing particle^{xviii,xix}. Another method for measuring neutron spectra at higher energies is the

use of a proton recoil detector which is usually an organic scintillator with trade names such as NE213 or BC501A. Above 20 MeV, the use of ordinary plastic scintillators such as BC408 plastic can be used. In these systems, the detector is placed in the beam and through the (n,2n) reaction in ^{12}C producing ^{11}C , it can be counted outside the radiation field. This is particularly useful in pulsed beam applications where a shutter can be used to stop the beam. Another class of detectors can be made from gas filled detectors such as the ROESPEC^{xx}, a series of proton recoil detectors and ^3He detectors of various sizes on a rotating table. Another detector design with high energy measurement capabilities incorporates the original BSS concept with an added downscattering material e.g. lead which was the starting point for this work.

High Energy Single Detector Rem Meters

One objective in radiation detection is to create a single neutron detector whose response closely resembles the energy response function of a unit of importance such as a unit for converting between fluence rates and dose rates. One such response function of particular importance over the years has been the fluence to ambient dose conversion coefficient for neutrons. This was originally observed with the eight inch sphere of the BSS. Modifications to this design produced a series of neutron detectors whose responses were similar to these response functions. Modifications on these detector configurations produced an energy response very similar to the fluence to effective dose conversion coefficients specified in technical reports such as ICRP Publication 74^{xxi}. More specifically, the detector's neutron response function is expressed in terms of counts per unit neutron fluence versus neutron energy; whereas the ICRP neutron fluence to effective dose conversion coefficients are expressed in terms of Seiverts (or rem) per

unit neutron fluence vs. neutron energy. Therefore, if the detector's response is similar to that of the ICRP conversion coefficients, then counts would be directly proportional to Sieverts (or rem), which makes the detector a neutron rem-meter.

One such detector is the LINUS rem-meter which consists of a single sphere of lead encased in polyethylene^{xxii}. As the incident neutrons pass through the lead can lose significant amounts of energy through inelastic scattering off the high Z material or via (n,xn) reactions off the high Z material. In the (n,xn) reaction, one neutron causes multiple neutrons to be ejected from the high Z material all with lower neutron energies.

Similar rem-meter designs to the LINUS, such as the WENDI^{xxiii} and SWENDI (Smart WENDI) have incorporated tungsten to produce single systems with energy responses that are similar to those of the fluence to dose conversion coefficients. Here, approximately 10.16 cm of moderator surround a high Z downscatter material and a ³He gas filled proportional counter which produces an energy response very similar to the fluence to effective dose conversion coefficients recommended in ICRP Publication 74^{xxi}. This is a modification on the eight inch moderate and capture detector used in the BSS. The original detector over-responded in the low energy region and under-responded above 8 MeV. To improve the energy response and make the detector more closely follow the ICRP specified ambient dose equivalent fluence conversion coefficients, the detector was wrapped in a cadmium cover with several holes to decrease the low energy response. To improve the high energy response of the LINUS and similar rem-meters, the detectors were also encased in a high Z downscatterer which increased the high energy response. Another detector system used proton recoil detectors and activation scintillators to produce a similar single detector rem-meter with a response that closely

follows the recommendations in ICRP Publication 74. The PRESCILLA, an acrylic (PMMA) and scintillator sandwich detector using the $\text{ZnS(Ag)}^{\text{xxiv}}$ scintillator material, harnesses both proton recoil and silver activation as a means for neutron detection. This detector provided a slow response to pulsed neutron beams which proved useful at high energy accelerator facilities.

A last, unique detector uses the concept of a tissue equivalent proportional counter (TEPC) as a detector. This detector, known as the REM500^{xxv}, uses a 5.08 cm A-150 plastic spherical detector and a helical anode wire filled with tissue equivalent propane gas at a very low pressure simulating 2 μm of tissue. As recoil protons pass through the gas, they produce a charge proportional to the dose delivered to the simulated 2 μm of tissue. Internal software folds this with lineal energy conversion coefficients and gives a direct readout of ambient dose equivalent or other dose equivalent value depending on selection of the lineal energy conversion coefficients. All of these detectors have successfully been used as single detector rem-meters for high energy neutron detection.

High Energy Neutron Spectroscopy Systems

In work done at PTB, a similar multisphere system called NEMUS was produced^{xxvi}. Lead and copper shells were used as high Z downscatter materials to produce unique responses up to 10 GeV neutron energies. NEMUS consists of a ^3He -filled proportional counter, 12 polyethylene spheres having diameters from 3" to 18", and four polyethylene spheres which contain copper or lead inlets and the high Z materials are embedded within an additional polyethylene shell. This system has been successfully used to measure high energy neutron spectra. Yet, it employs an active detector which is

not useful for measurements in intense or pulsed radiation fields where dead time losses can arise from pulse pile-up. This specialized system is expensive and produces only four additional response curves in the high energy region.

Current Work – Bonner Sphere Extension for High Energy Structure

The current work investigated and constructed a cost-effective multisphere system inspired by the NEMUS system. However, it incorporates both passive and active detection technique capabilities. Specifically, ^{197}Au activation foils and a standard ^6LiI scintillator are used as detectors. This system responds to neutron energies from 0.001 eV through 1 GeV. The design builds on the original design which too responded in these energy regions, just lacking structure and sensitivity above 30 MeV. The spectrometer described herein uses more spheres than NEMUS to further enhance the energy sensitivity and response structure in the high energy region compared to existing systems. This system of extended spheres builds on the original BSS and is, in this text, referred to as the Bonner Sphere Extension (BSE). The BSE uses combinations of spheres having also the same materials and a series of different radii. The system is further described in on page 29. Briefly, high Z downscatter materials surround an inner 3" or 5" Bonner sphere and can be encased in outer polyethylene covers. A total of 24 sphere combinations are possible, providing unique responses and improved energy structure in the measured spectra. To gain structure in the region below 100 keV through 1 keV, responses for additional spheres of radius 3.5", 3.25", 3.5", 3.75", 4", and 4.5" were computed. Since the primary focus however was to start with a commercially available off the shelf BSS, the responses of the 3.25", 3.5", 3.75", 4", and 4.5" spheres were not constructed.

CHAPTER 2

THEORY

Standard Bonner Sphere Response

The original BSS system was designed around a moderate and capture detector in which a thermal neutron detector is placed in the center of a polyethylene moderator. The detector is a small LiI(Eu) crystal mounted to a light guide and then coupled to a photomultiplier tube (PMT). When a fast neutron impinges on the Bonner sphere, the incident neutron loses some fraction of its initial energy primarily through elastic scattering from the carbon and hydrogen in the polyethylene. A neutron can lose a significant amount of energy, especially through elastic scatter with hydrogen in which it can lose up to 50% its initial kinetic energy in a single scatter. Maximum energy loss from elastic scatter off carbon is approximately 28% of its initial energy^{xxvii}. After losing energy via elastic scattering events, the probability of the neutron undergoing an (n, α) reaction in the LiI crystal increases because the cross section for this type of interaction increases with decreasing neutron energy. The cross section for (n, α) absorption can be seen in Figure 1.

After undergoing multiple interactions, the neutrons, if they have not escaped the system, are slowed to thermal or near thermal energies. In this energy range there is a high probability that the neutron will be captured; the capture reaction has a cross section of 941 barns for thermal neutrons whereas at higher energies around 1-MeV it is considerably lower, 0.3 barnsⁱⁱⁱ.

Spheres of different diameters are used to provide different amounts of moderation of the incident spectrum. Small spheres offer minimal moderation and so

their response is largely to lower energy neutrons incident on the sphere. Large spheres offer substantial neutron moderation, and the detector response has is most sensitive to relatively high-energy neutrons incident on the sphere which can be seen in Figure 2. By varying the neutron moderator thickness, the response of a given diameter sphere becomes stronger in a different energy region. A simplified diagram of the moderate and capture detector is shown in Figure 4. In Figure 4, the thermal neutron detector is shown in red. In Figure 4A, a detector having a strong response to low energy neutrons is shown. In a detector designed for low energy neutrons, few scatters are required for a neutron to thermalize and be captured. In Figure 4B a system designed to have a high energy neutron radiation response is shown. In this detector configuration, multiple scatters are required to thermalize the high energy neutrons.

The size of the moderator has a direct impact on the detection efficiency. As the moderator size increases, the overall efficiency drops. Each sphere's energy response decreases as energy increases. Above about 23 cm of radial moderating material (an 18" ball), the efficiency drops substantially as well as the detector becoming too cumbersome to use. The 18" sphere weighs approximately 47 kg and is too heavy for some experimenters to place on the detector delicately. This 18" sphere produces a peak around 18 MeV and no more unique energy structure information above ~25 MeV. For higher energy responses, new detection systems are required to increase the sensitivity and produce more energy response structure.

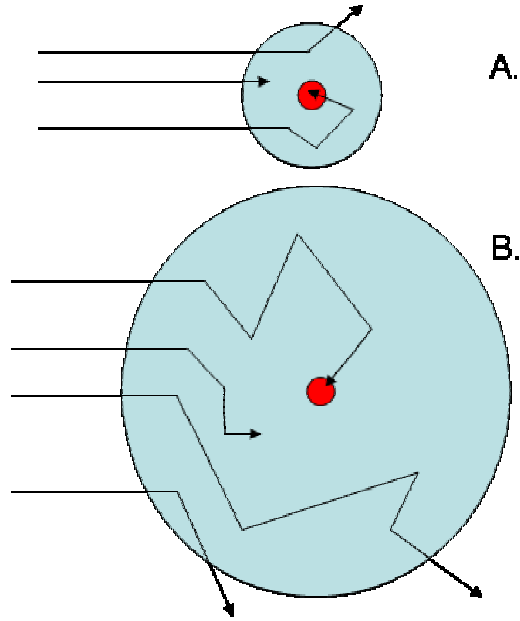


Figure 4. A simplified diagram for the moderate and capture detector method.

Extended Bonner Spheres for Increased Response above 20MeV

Several research groups have investigated the use of high atomic number (Z) shells placed within polyethylene spheres to increase the high energy response. These high Z materials have large (n,xn) cross sections for high energy neutrons and thus function as high energy neutron multipliers.³⁻⁶ Neutrons can lose a significant portion of energy through the (n,n') reaction, and can produce multiple exiting neutrons through $(n,2n)$, $(n,3n)$, and (n,xn) reactions where the x is a number greater than 3 that has an associated distribution as a function of energy for a given isotope. One of the first detectors to incorporate this was the LINUS rem-meter. In the LINUS rem-meter system, a borated inner shell is used to help match the detector response as a function of energy to the suggested fluence to effective dose conversion coefficients^{xxviii}. This produced a single sphere that closely mimicked the energy response to neutrons as that of the suggested fluence to effective dose conversion coefficients. Seeing this, the researchers

at PTB produced one of the first spectrometers to use this system and the end result was the NEMUS system^{xxix}, a system which can be used for spectra measurements, makes use of copper (Cu) and lead (Pb) spheres to form concentric shells around a ^3He detector. A polyethylene core is needed to help thermalize the inelastically scattered neutrons from the downscatter shell. The general design of the downscatter, moderate, and capture detector system can be seen in Figure 5.

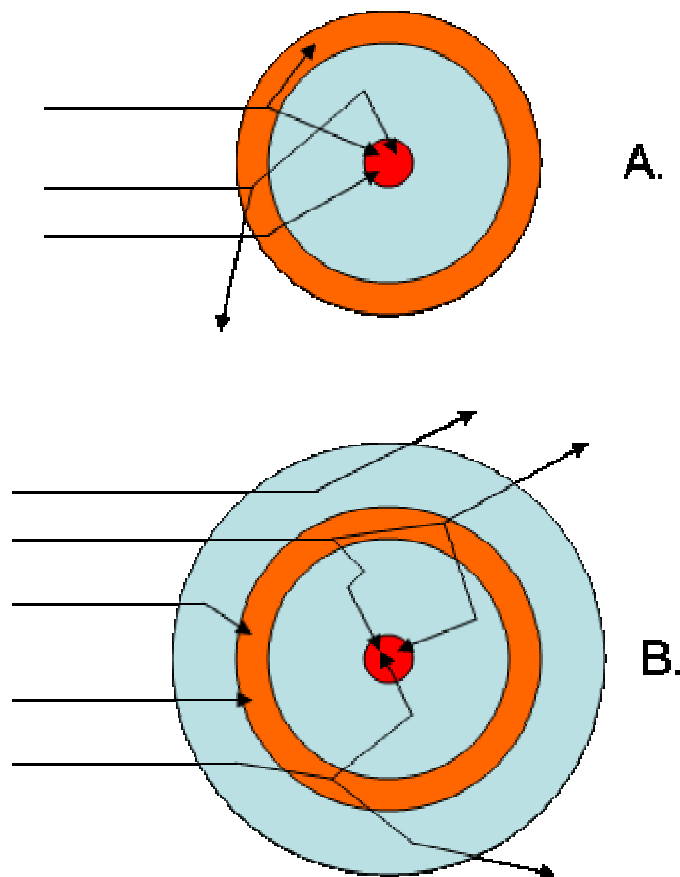


Figure 5. A simplified diagram for the downscatter, moderate, and capture detector method.

In Figure 5, the thermal neutron detector is shown in red. In Figure 5A a detector optimized for neutron energies between 20 and 100 MeV is shown. In this scenario, after

down scattering, relatively few elastic scatter events are required for a neutron to thermalize and be captured. In Figure 5B a system optimized for very high energy neutron radiation with energies in excess of 100 MeV through the GeV range is shown. The detector responses for these systems will be shown later in Chapter 5. In this detector configuration, multiple scatter events are required to thermalize the high energy neutrons. The addition of an outer polyethylene sphere and larger inner sphere can push the energy response very high for energies in excess of 200 MeV. The moderating spheres and downscatter shells are selected such that each detector-moderator combination results in a unique response to the incident neutron spectrum.

Mathematical Deconvolution of Data Measured with Moderators

The output from Bonner Spheres does not directly provide neutron spectra. The output is merely a count of the number of (n, α) reactions in the scintillator over a given exposure time period or total activity obtained over a given exposure time period. An example of this can be seen in Chapter 5. The response of a Bonner Sphere to a given neutron spectrum is given by the first order Fredholm integral equation of the first kind, namely the count rate is:

$$C_i = \int_0^{\infty} R_i(E)\phi(E)dE \quad i = 1,2,3 \rightarrow N$$

Equation 1

where C_i = count rate for the i^{th} detector arrangement (counts per second)

$R_i(E)$ = response function for the i^{th} detector at energy E (counts per unit neutron fluence)

$\varphi(E)$ = energy-dependent neutron flux (n/cm²-sec)

Equation 1 is reduced to a matrix equation for solution

$$C_i = \sum_{g=1}^G R_{i,g} \varphi_g$$
$$i = 1,2,3 \rightarrow N$$

Equation 2

where φ_g = group flux between E_g and E_{g+1} which is the total measure of neutron fluence between the upper bound energy E_{g+1} and the lower energy bound E_g .

and R_{ig} = multigroup form of the i^{th} detector response.

It is desirable to produce an output spectrum of with many energy groups. However, the system of equations, namely the number of unknown energy groups and the number of equations (detector arrangements) are such that the matrix equation is underdetermined e.g. there is no unique solution to this equation because the total number of energy groups is typically larger than the number of detectors. This is especially true when trying to unfold into the higher energy regions where there are limited unique data points in the response data. The group fluxes, φ_g are often chosen to have boundaries that closely mimic points of interest such as resonances and dosimetry quality factor evaluation points. Since the system is underdetermined; an iterative solution process is sought which requires initiate process^{xxx}. There are a number of computer codes available for solving this system of equations. Two in particular are noted here. The first code, GRV_FC33 is a least squares fitting iterative algorithm based on the SAND-II code^{xxxii}. Here the iterative routine tries to minimize the deviation of the least squared fit

of the solution spectrum from one iteration to another. This iterative method guarantees a non-negative flux. The second code, MXD_FC33 is based on a maximum entropy iteration routine^{xxxii}. This code was written specifically for the unfolding of BSS data^{xxxiii}. In this method, the impact of the error in a measurement is considered and fitting routine is run to minimize the overall error not only from the measured responses but also the spectral fit. By using this method, the impact of each sphere can be carried forward and used to predict the total uncertainty of the measurements^{xxxiv}. A detailed derivation of the mathematics involved in the unfolding process can be found in references xxx-xxxiv.

CHAPTER 3

DETECTOR DESIGN

Bonner Sphere System with Active Scintillator

The active BSS system is nearly identical to the design by Bramblett, Ewing, and Bonner^{iv}. The current design makes use of a 4 mm tall by 4 mm outside diameter LiI(Eu) crystal. This commercially available detector is sold by Ludlums Inc¹. This crystal is coupled to a 1” diameter photomultiplier tube (PMT) through a stepped acrylic light pipe. The crystal is optically coupled to the light pipe and the light pipe and optically coupled to the PMT using optical silicone grease. The detector is in an aluminum housing. The PMT was wrapped in a MuMetal (a metallic conductive shield for lowering background electronic noise) and then wrapped and soldered the overlap in a thin copper foil. This modification was performed by the author at Georgia Tech to ensure the detector would not be susceptible to high frequency electromagnetic noise that is at accelerator facilities. The addition proved to be highly beneficial in tests at electron accelerator facilities. When used experimentally at the WNR LANSCE facility, very little electronic noise was present. A diagram of the detector can be seen in Figure 6.

¹ The LiI(Eu) probe is sold under the part number 47-1505. The model used in these experiments is called a 42-5 Neutron Ball Cart from Ludlum Inc. Sweetwater, Texas.

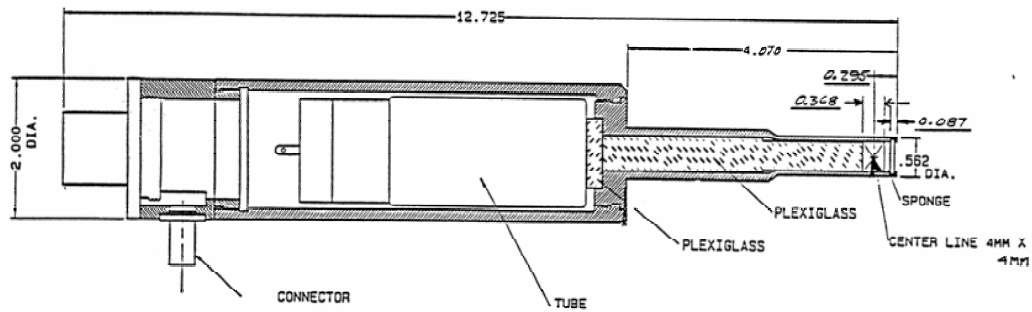


Figure 6. A cutaway diagram of the LiI(Eu) detector assembly showing the Plexiglas light pipe and PMT.^{xxxv}

Two methods exist for recording the pulses from the LiI(Eu) scintillator. The first method is the use of a single channel analyzer (SCA). This system counts pulses from the detector that fall into the SCA energy “window”. Here gross counts can be recorded. By subtracting the background count rate in a purely gamma environment, net counts can be produced as a function of time in the neutron gamma field. A second method uses a multi-channel analyzer in which pulses are binned according to their pulse height in volts. In this work, a multi-channel analyzer (MCA) was used to record the pulses. This allows for a finer background subtraction of gamma ray noise in the residual spectrum than the SCA energy window method. As gamma rays interact in the crystal, they produce recoil electrons. These recoil electrons typically have ranges larger than the crystal. This is the reason the crystals are kept quite small. Since the electrons don’t fully deposit their energy, they produce a Compton recoil electron spectrum. Even though the crystal has a very small diameter, there is still considerable gamma ray background that is present in the measurements. An example of the spectra obtained on an MCA can be seen in Figure 7. Shown in pink is the spectrum plotted on a logarithmic scale, and the blue on a linear

scale. A Compton continuum can be seen below the large (n, α) peak. Since the area is not perfectly rectangular under the continuum and the continuum varies as a function of incident gamma ray energy, the MCA provides a superior background subtraction method. A line can be drawn between the endpoints of the (n, α) peak and the area under that curve can be subtracted from the area under the (n, α) peak producing a true net count rate.

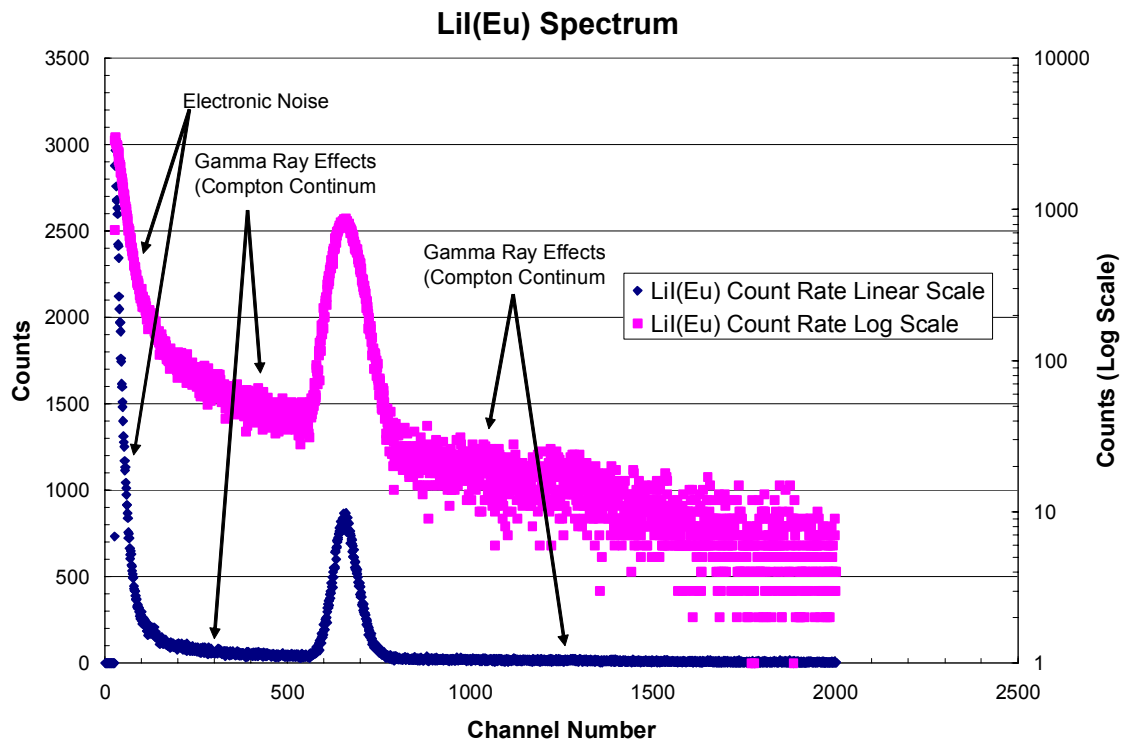


Figure 7. An example Lil(Eu) spectrum.

The Ludlum Bonner spheres are made out of high density polyethylene with an average density of 0.95 g/cc. The spheres are drilled out to fit over the detector shown in Figure 6. The Ludlum set is comprised of 2", 3", 5", 8", 10" and 12" diameter spheres. In other systems such as NEMUS, 3.5", 4", 4.5" and 6" spheres^{xxxvi} are also used. This is

because the NEMUS system uses an SP9 spherical proton recoil detector which is larger than the LiI(Eu) detector. The SP9 spherical proton recoil detector has a 3” diameter. During the initial design investigations additional spheres of 2.5”, 3.25”, 3.5”, 3.75”, 4”, and 4.5” were included in the modeling studies. However, the added energy structure of the 2.5” and 6” sphere did not provide a significant increase in structure and was discarded. Since the objective was to extend the commercially available systems to have increased sensitivity to neutrons above 20-MeV, these spheres were never manufactured, Their responses were still calculated and machining drawings were created for future work.

Bonner Sphere System with Passive Gold Foil

The passive detector system was built to mimic the specifications of the LiI(Eu) scintillator housing in shape. The foil holder was turned from a single piece of high density polyethylene by hand in the departmental machine shop. The probe was designed to hold a gold foil at a location that corresponds to the crystal centerline in the LiI scintillator. This requires that a small air gap be left above the polyethylene holder when it is inserted into the Bonner spheres i.e. the holder is slightly shorter than the bored opening in the Bonner spheres. It is important for the activation foil to be at the centerline of the Bonner sphere to attain a nearly isotropic angular response.

The starting data for unfolding foil activation data is the production rate of the isotope to be counted during the measurement. The steps in obtaining that quantity follow and are based on the discussion in Knoll^{xxxvii}. The Production rate (atoms/sec) of isotope x in a foil of volume V is:

$$\dot{P}_x = \varphi \sigma_x V$$

Equation 3. The production rate of isotope x during irradiation.

In Equation 3, the σ_x is the energy dependant microscopic cross section for the reaction to produce isotope x. φ is the energy dependant fluence rate of neutrons through volume V . During irradiation, the rate of change of atoms of isotope x is shown Equation 4 where λ is described as the decay constant shown in Equation 5.

$$\frac{dN_x}{dt} = \dot{P}_x - \lambda N_x$$

Equation 4 The differential equation describing the time rate of change of the number of atoms of isotope x during irradiation.

$$\lambda = \frac{\ln(2)}{t_{1/2}}$$

Equation 5. The decay constant λ as a function of the isotopes half life in seconds.

All of these equations assume a constant production rate. Simplifying Equation 4 the number of radioactive atoms at time t can be represented by

$$N_x(t) = \frac{\dot{P}_x}{\lambda} (1 - e^{-\lambda t})$$

Equation 6. The number of radioactive atoms as a function of time during irradiation.

It is more frequently useful to have the production rate in terms of activity produced per second (Bq/s). In this case, Equation 6 simplifies to Equation 7.

$$A_x(t) = \dot{P}_x(1 - e^{-\lambda t})$$

Equation 7. The production rate as a function of time during irradiation in units of activity per second.

After the foil is activated and removed from the radiation field, the foil only decays. The activity at some time t' after irradiation can be described by Equation 8.

$$A_x(t') = \left[\dot{P}_x(1 - e^{-\lambda(t_o - t_i)}) \right] e^{-\lambda(t_i - t')}$$

Equation 8. The activity at some arbitrary time t' after irradiation.

Here, t_o is the start irradiation time, t_i is the stop irradiation time, and t' is the time after irradiation. The activity of the foil is counted using a gamma-ray spectrometer. When this foil is then counted on the spectrometer, the count rates expected by the integral under the photopeak obtained by the detector can be described by Equation 9.

$$C_x(t') = \varepsilon B_R \left[\dot{P}_x(1 - e^{-\lambda(t_o - t_i)}) \right] e^{-\lambda(t_i - t')} + B$$

Equation 9. The expected count rate at the detector at time t' .

In Equation 9, the ε variable is the counter efficiency for a given radiation emitted, B_R is the branching ratio or percent emission of that particular radiation type, and B is the background count rate. This is routinely programmed into the computer, in any standard gamma spectroscopy program. GammaVision² software was used to analyze the MCA

² GammaVision is a gamma spectroscopy computer package available from E.G. & G. Ortec.

data from the HPGe^{xxxviii}. The activity is calculated at the start time of counting by hand using Equation 10.

$$A_x(t') = \frac{C_x(t')\lambda}{\varepsilon B_R [\dot{P}_x (1 - e^{-\lambda(t_o - t_i)})] e^{-\lambda(t_i - t')}}}$$

Equation 10. the activity at counting time as a function of count rates.

In this case, the overall desired quantity is the production rate \dot{P}_x , it is possible to calculate that by inserting Equation 9 into Equation 10, the production rate, for a given isotope from a given target can then be found. Later, in Chapter 4, this unit will be required since the response matrices are calculated in these units of production rate.

$$\dot{P} = \frac{A_x(t')\lambda}{(1 - e^{-\lambda(t_o - t_i)})m}$$

Equation 11. The production rate of a given isotope as a function of counts on a gamma spectroscopy system. The m in the denominator is the mass of the foil.

A unique problem exists however if the production rate is not constant. This occurs if the beam is pulsed with long durations between pulses or if the neutron field suddenly stops, starts, or changes in intensity. In these cases, the activity at t' can be found as a summation of production and decay runs. In this case, Equation 8 becomes:

$$A_x(t') = \frac{C_x(t')\lambda}{\varepsilon B_R \left[\sum_{n=1}^N \dot{P}_{x,n} (1 - e^{-\lambda(t_{o,n} - t_{i,n})}) e^{-\lambda(t_{i,n} - t')} \right]}$$

Equation 12. The activity at a given time t' for a series production and decay

In this work to use the passive system, the gold foils are irradiated and the 411 keV photopeak line was counted offline usually with a High Purity Germanium (HPGe)

detector. A vertical PopCap style HPGe was selected for ease of use³. For the best results, measurements with an HPGe should be carried out in a low background environment. To reduce the background, a small cave was built around the active volume of the crystal out of low background lead and then wrapped in clean virgin copper. The copper was used to cut off the low energy photon emission of the Naturally Occurring Radioactive Material (NORM) in the lead bricks. Lead contains naturally occurring ²⁰⁴Pb which is radioactive as well as lead that was above ground during the years of atmospheric testing contains trace quantities of ²⁰⁵Pb which can also be produced through cosmic ray interactions in the lead. The primary photons emitted from these isotopes are below 20 keV and are easily shielded with a layer of copper. The detector cave is shown in Figure 8.

³ An Ortec HPGe in a PopCap[®] detector with an efficiency of 18% to that of a 3"x3" right circular cylinder NaI(Tl) detector for the ⁶⁰Co gamma rays was used. Data was recorded using the GammaVision software package.



Figure 8. HPGe detector setup with lead shielding cave and NIM modules for running the detector.

The electronics configuration for the HPGe was as follows: the HPGe was attached to a spectroscopy amplifier and then to a TRUMP-8k MCA card, and data was collected in 8,096 channels, with the peak of interest located at 411 keV. The count rate of the 411 keV peak was used to determine the production rate of ^{198}Au following Equation 12. Shown in Figure 9 is a sample HPGe spectrum. In this spectrum, the 411 keV (n,γ) reaction is shown. Also, the $(n,2n)$ peak is present. Lastly, the 1.4 MeV ^{40}K peak from NORM at Los Alamos is present.

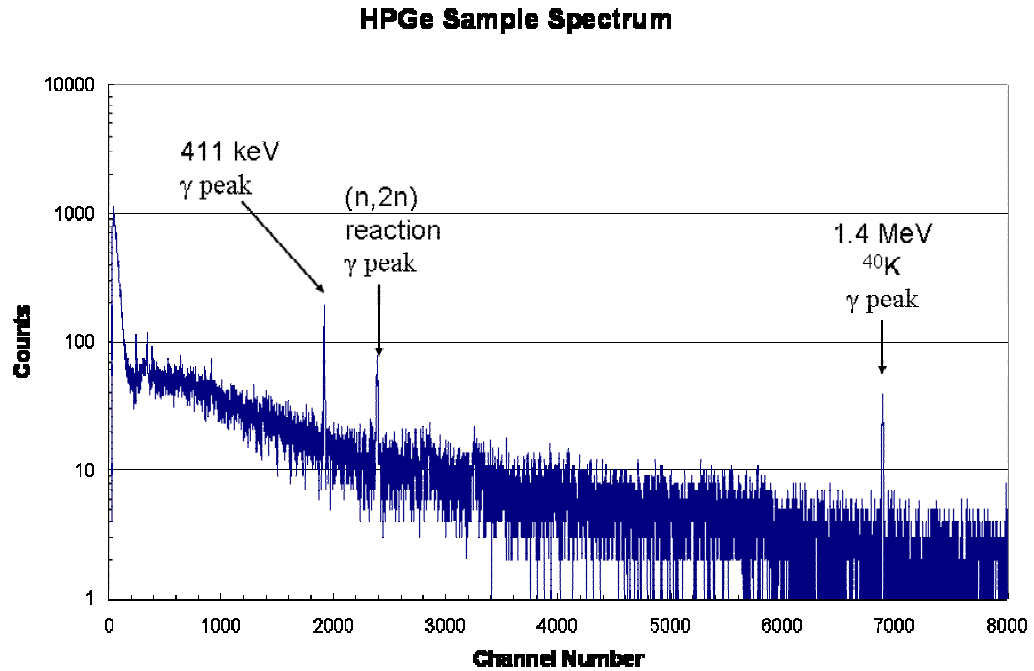


Figure 9. A sample gamma ray spectra from the HPGe detector.

High Energy Bonner Sphere Extension

To produce the spherical shells, aluminum shells were needed. The high energy extension component was built around the existing 3" and 5" polyethylene spheres. Using the 3" and 5" Bonner spheres as cores, aluminum shells were fabricated⁴. Two sizes of shells were fabricated from 12 gauge aluminum sheet: (1) shells with three inch inside diameters were made to be used with aluminum shells with 5" outside diameters and (2) aluminum shells with 5" inside diameters were made to coincide with shells with 7" outside diameters. These two shells are referred to as the small assembly and large assembly. This can be seen in Figure 10.

⁴ The shells were produced by Century Metal Spinning in Bensenville Illinois 60106

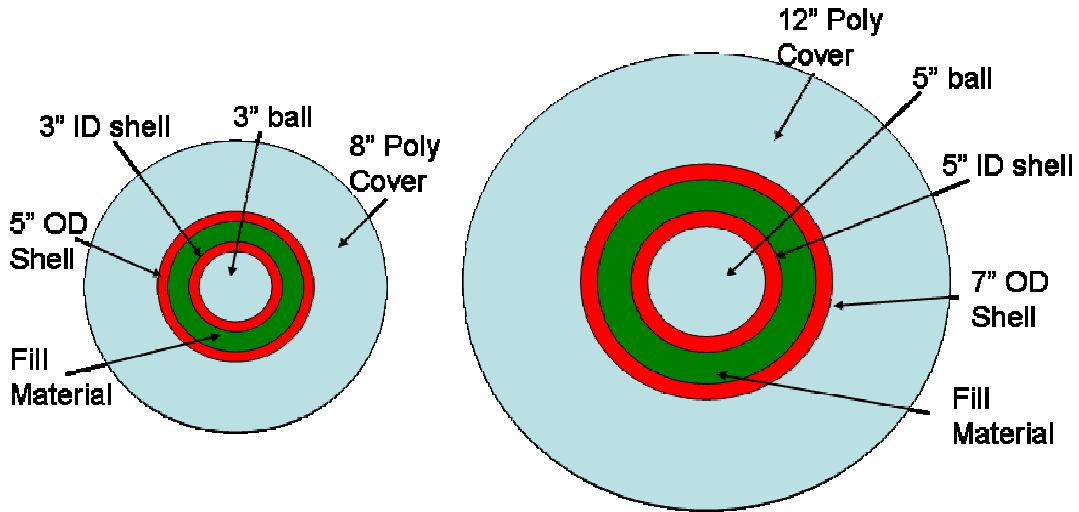


Figure 10. A diagram of the small and large spherical shell assemblies.

Copper, lead, bismuth, and tungsten were investigated as potential high Z fill materials for the small and large assemblies. In the end, the copper, lead and tungsten was chosen as the filler. The copper was purchased in a 98% purity with a granular size of ~ 1 micron⁵. This fine copper powder had only slight impurities of aluminum and nickel. Tungsten pellets were taken from preexisting spherical shell at Georgia Tech. The granular size of the tungsten was measured and found to have an average of ~ 100 microns. The lead was melted and cast into the shells.

Early designs had the shells open along the vertical with respect to the detector chassis, an optimized design for a side-on irradiation field. CAD drawings of these designs can be seen in Figure 11 and Figure 12. Due to fabrication costs, this design was abandoned in for a simpler and cost effective design in which the spheres open horizontally (perpendicular to the detector chassis). This design is optimized for a top down radiation field, but is equally suited for a side-on radiation field.

⁵ This is assumed to be a distribution of sizes with an average value of 1 micron.

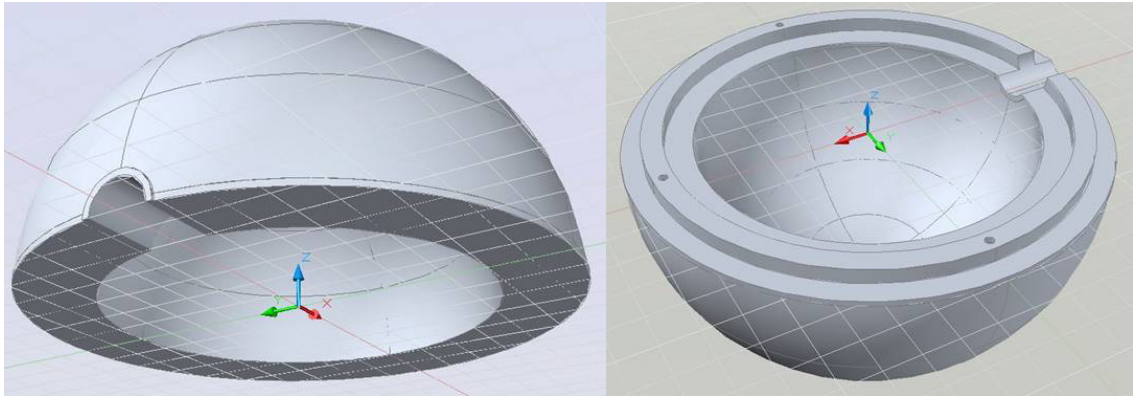


Figure 11. A CAD representation of the preliminary BSE design is shown with the shells opening vertically.

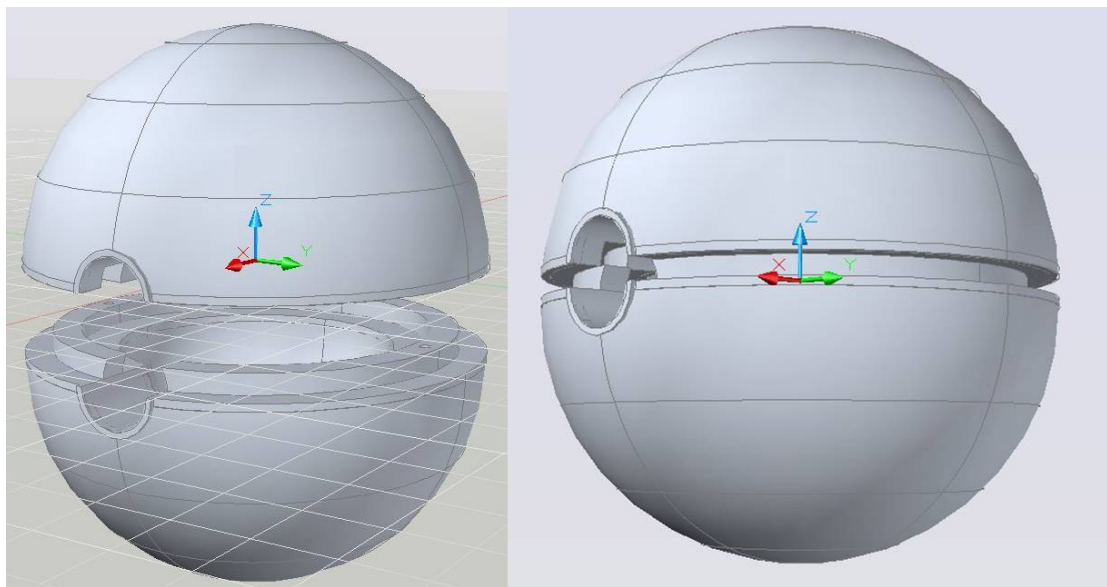


Figure 12. A CAD representation of the preliminary BSE design is shown with the shells opening vertically. Here a shell set is shown closing to show the alignment of the BSE.

The 3" sphere, the 3" ID and 5" OD shells (small assembly) were welded together with an aluminum ring with a butt weld inside and out. A small locking lip was turned as well as drilled and tapped a 1/8" fill hole. Three small assemblies were made totaling 6 hemispherical shells. Three sets of the large assembly shells (5" ID and 7" OD shells)

were similarly constructed. A 3" sphere and 5" sphere will fit inside the small and large assemblies respectively. Shown in Figure 13 are the spherical shells early in the fabrication process. The filler hole and the unfinished butt weld are visible.



Figure 13. The spherical shells during the fabrication process at the Georgia Tech Research Institute (GTRI) machine shop.



Figure 14. The 5” spherical shells (large assembly) in early production stages. The first locking lip can be seen cut into the surface.

Once shell fabrication was complete, the filling process began. Since not all of the materials could be cast into the shells due to very high melting points, and the machining of bulk materials was too costly and wasteful, powdered high Z materials were used as a cost effective alternative⁶. One difficulty with using the powdered materials is the packing ratio, or how close to theoretical solid density one can achieve with this type of system. To measure the density of the powdered fill material, volume and mass

⁶ Alfa Aesar was used as the provider of the bulk powdered copper.

measurements were made for each shell prior to filling. Each shell was assigned a specific serial number. The shells were individually weighed on a calibrated and NIST traceable scale. Each shell was then filled with water using a graduated burette and the fill volume was recorded (water was poured out and spheres were allowed to dry). Once the volume of each shell was known, matching pair of shells was then filled with one of the high Z fill material. Shells were matched according to their fit, since as they were machined, they were machined to match each other in pairs with slightly different locking lip radii to prevent the mixing up of the shell sets. An iterative process involving shaking and filling as well as compaction through the fill hole was used to ensure a high density filling. The spheres were then allowed to settle and then topped off with even more material. The lead spheres were filled with molten lead. To ensure no air pockets or void spaces were present, the spheres were then baked in a high temperature oven for 2 hours to reliquefy the lead. The filling procedure can be seen in Figure 15.



Figure 15. Smelting lead and ladling it into the shell.

To ensure complete filling and no void pockets, each shell was imaged using the electronic imaging system and a 6-MV x-ray beam from a medical linac at The Emory University Radiation Oncology Department. High energy imaging was essential because low kilovolt x-ray energies are insufficient to penetrate high Z-materials. No void pockets or density changes were found in any of the spheres. Upon completion of the filling and imaging, each sphere was weighed on a precision scale. Knowing the mass difference, and the volume, a volume averaged density was calculated. In Table 4, the measured densities for the powders in the filled shells are given. These data were used for

detailed simulations of the detector systems. Finally, the shells were sanded repeatedly with 1000 grit sand paper to polish the surface to increase the esthetic beauty of the spheres.

Ancillary Equipment Used at LANSCE

For the measurements at LANSCE, a time of flight (TOF) system was used to measure the neutron spectra at the location where the BSE would be tested. This system utilizes a series of optically thin ^{238}U foils in a fission chamber configuration. The TOF chamber is filled with argon gas at just over 1 ATM. The fission chamber records counts as the fast neutrons cause fissions in the ^{238}U . The TOF detector does not count neutrons below 1 MeV because there is an approximate 1 MeV threshold for the fission reaction. The detailed construction and operation of this fission chamber system are described in the literature^{xxxix}. A T_0 pulse or zero timing pulse is produced from the “gamma flash” of the initial protons striking the tungsten target. The following events that occur through neutron interactions are then recorded as a function of time. The time between the gamma flash and the neutron induced counts are used to compute the neutron energy. The LANSCE accelerator was operating between 40 and 60 Hz delivering macropulses during these experiments and the flight path for this experiment is located 90-m from the target. A diagram of the beam timing and intensity is shown in Figure 16.

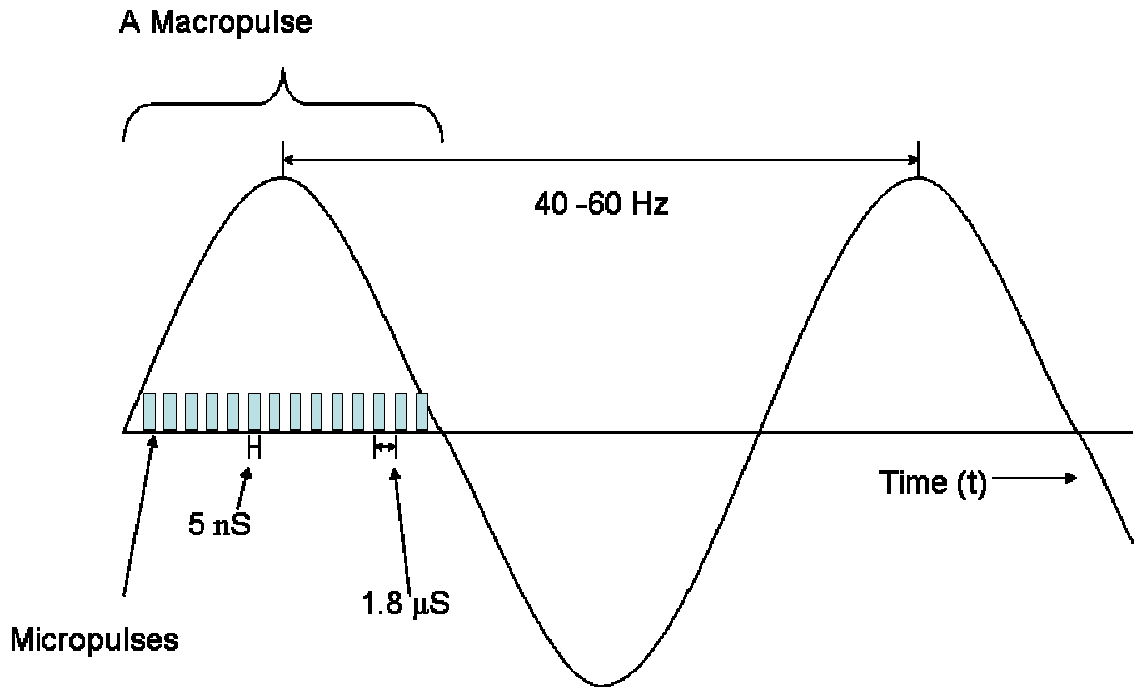


Figure 16. The beam profile of the typical LANSCE WNR beam as a function of time^{x1}

Due to the high frequency of the micropulses, the neutrons from the previous micropulse would still be traveling down the flight path when the next pulse arrives, which is known as pulse wrap around. Because of the pulse wrap around, the lowest distinctly identifiable neutron energy at the measurement station was 20 MeV with the lowest reading of any statistical certainty approximately equal to 35 MeV.

LANSCE is a multi user pulsed neutron beam driven by a high power proton linac and therefore can experience rapid electromagnetic field fluctuations, ranging from a complete loss of beam pulse to a beam with very high neutron fluence rate usually caused by another experimental facility such as Lujan going offline. Knowledge of the production rate is important. A beam monitor was utilized to continuously monitor the neutron flux within the area of the experiment. The monitor consisted of a ^3He tube moderated by a large acrylic block. The 30.48 cm thick, 60.96 cm by 60.96 cm block

thermalized the neutron beam to allow detection by the ^3He thermal detector tube. The probe was placed immediately behind the sphere, and was shadowed by the sphere. This is acceptable since this monitor was only looking for the relative beam intensity, not an absolute measure. This was used to normalize the time that each measurement was made for. The location of the beam monitor inside the measurement area at LANCE is depicted in Figure 41. This scaler⁷ was then connected to the data logging computer in the beam line. So 1 second averaged neutron fluxes could be monitored throughout the experiments from outside the beam area. The electronics for beam monitor are depicted in Figure 17.

⁷ The tube was connected to a Ludlum 2200 series scalar/ratemeter.

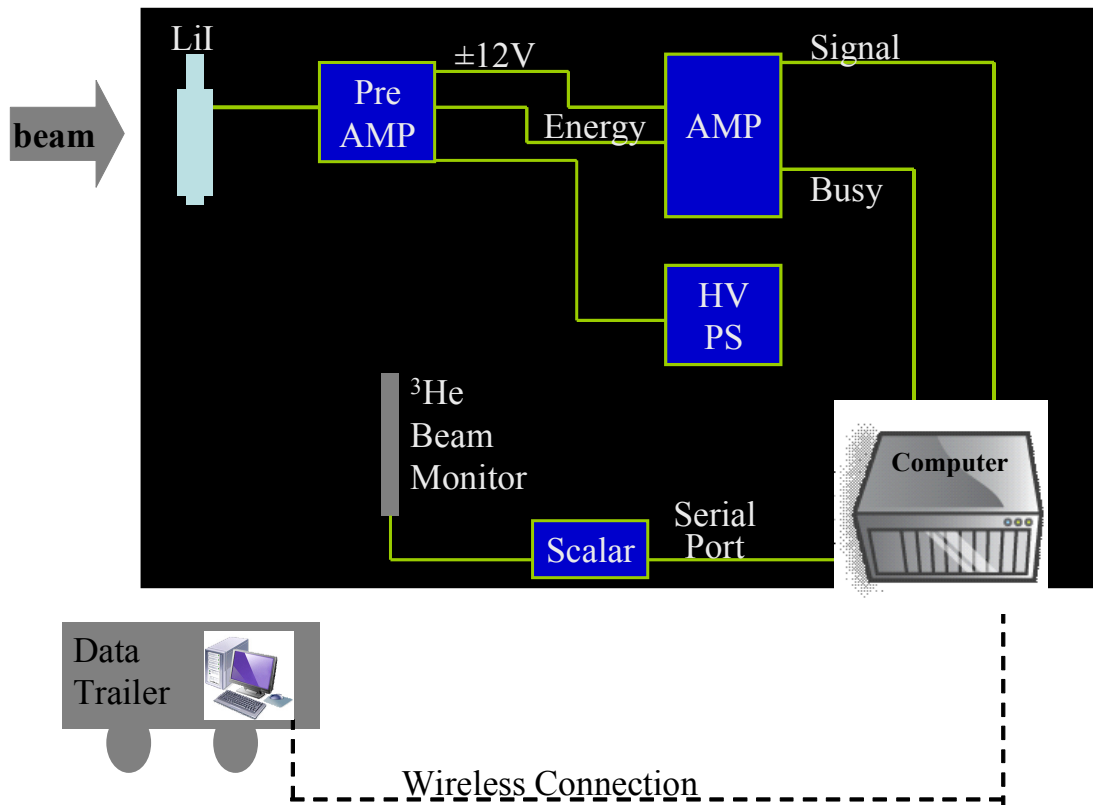


Figure 17. A simplified schematic for the data acquisition system used at the LANSCE facility.

Finally, image plates were used to assess the beam profile at the experiment station. The beam images were taken on storage-phosphor image plates that were 8" x 8" and are commercially available from the Fuji Photo Film Company. Due to the large beam area, two to four image plates were pieced together.

CHAPTER 4

DETECTOR MODELING

In order to better understand the response of the new detector assemblies, a series of computer simulations were made of the BSS BSE systems for the testing facility at LANSCE. For coupled neutron and proton radiation transport only a few codes have the capability of producing accurate results. These codes are GEANT4 radiation simulation toolkit^{xli-xliii} based on C++, MARS^{xliiii}, FLUKA^{xliv-xlv}, and MCNPX^{xlvi}. MCNPX^{xlvii} was selected for use in this project because of its robust nature. MCNPX offers versatility, the ability to use physics models as well as tabular cross sections for protons^{xlviii}, and variance reduction tools. Using the newest beta test version MCNPX 2.6e available, the detector and experimental facilities were modeled in as much detail as was available.

Detector Modeling

The detectors were modeled in detail using the “as built” details, including the standard Bonner spheres (2”, 3”, 5”, 8”, 10” and 12” spheres), the additional low energy spheres, and the extended spheres. The additional spheres that are not typically a part of the BSS system were modeled which include the 3.25”, 3.5”, 3.75”, 4”, 4.5”, 15” and 18” spheres. The extended spheres (designed for this work) can be used to produce many different shell and polyethylene cover combinations. These different combinations were modeled. Both the active (LiI(Eu) version) and passive detector (poly holder with gold foil) systems were modeled. The MCNPX model of the LiI(Eu) detector can be seen in Figure 18. The physical dimensions of the sphere sets can be found in Table 2 and Table 3. The corresponding MCNPX models of the system can be seen in Figure 20.

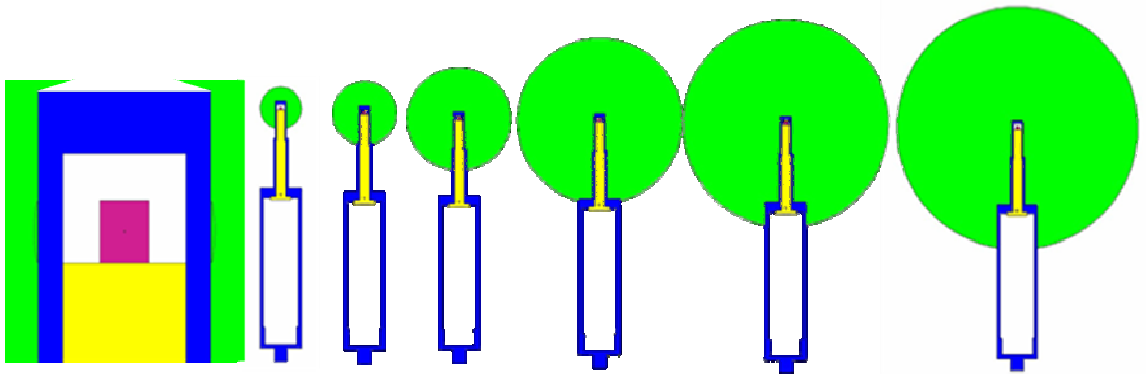


Figure 18. The LiI(Eu) detector models from MCNPX in the standard poly sphere set. On the left is a closeup of the LiI(Eu) crystal. The image is not to scale.

The details for the LiI(Eu) probe model were taken from drawings provided by Ludlum Inc. The dimensions and physical details for the model were taken from these machining drawings^{xlix}. When creating the pure polyethylene version, the physical dimensions of the LiI(Eu) probe were used with the exception of the air gap. The air gap remained present in the model.

The detailed models of the geometry of the BSE took into account the slight imperfections which resulted during fabrication. One imperfection was a slight air gap between the aluminum rings that held the two shell halves together. This air gap originated from overheating the aluminum ring while TIG welding the spheres to it. This caused the aluminum ring to warp slightly resulting in an air gap. The slight air gap for the three inch spherical shell and five inch spherical shell that had the largest gap can be seen in Figure 19. A table listing the measured gaps can be found in Table 1.

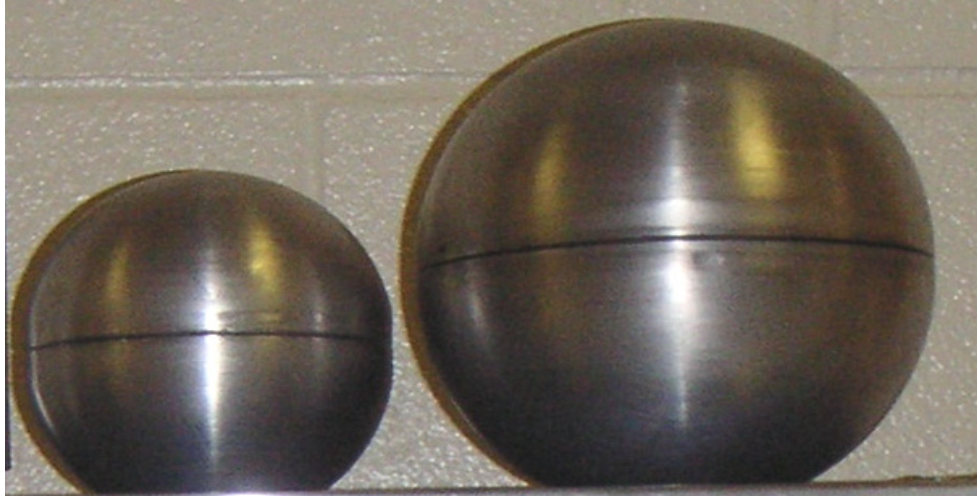


Figure 19. Three inch and five inch tungsten spheres showing the small air gap.

Table 1. Air gap spacing for the different spherical shell sets.

Material	ID Size (In)	Measured Air Gap (mm)
Cu	3	2.5
	5	0
Pb	3	0
	5	0
W	3	1.5
	5	0.5

Table 2. Dimensions of the top spherical shells for the BSE. The small assemblies are the ID sizes of 3, the large assemblies are the 5 inch labels

Material	ID Size (In)	Outside Edge (mm)	Inside Edge (mm)	Ridge depression (mm)
Cu	3	4.5	2.5	2
	5	4	1.5	2.5
Pb	3	5	3	2
	5	6	5	1
W	3	4	2	2
	5	4	2	2

Table 3 Dimensions of the bottom spherical shells for the BSE.

Material	ID Size (In)	Outside Edge (mm)	Inside Edge (mm)	Ridge height (mm)
Cu	3	6.5	4.5	2
	5	4	6	2
Pb	3	3	5	2
	5	5	6	1
W	3	3.5	4.5	1
	5	1.5	4	2.5

Table 4. Physical properties of the spherical shells

Densities of the shells of the BSS Extension

Material	Size	Hemispherical Shell	Initial mass (kg)	Final mass (kg)	Net mass (g)	Volume (cm ³)	Density (g/cm ³)
Copper	3"	Top	0.175	1.70	1525	380	4.01
		Bottom	0.192	1.75	1558	367	4.25
	5"	Top	0.348	3.725	3377	820	4.12
		Bottom	0.361	4.70	4339	818	5.30
Lead	3"	Top	0.177	4.35	4173	371	11.25
		Bottom	0.193	4.30	4107	362	11.35
	5"	Top	0.366	9.70	9334	825	11.31
		Bottom	0.351	9.45	9099	820	11.10
Tungsten	3"	Top	0.179	4.90	4721	366	12.90
		Bottom	0.193	4.70	4507	379	11.89
	5"	Top	0.348	10.20	9852	820	12.01
		Bottom	0.362	10.25	9888	824	12.00
HDPE	small		2.85		2850	3341	0.853
	big		10.45		10450	11710	0.892

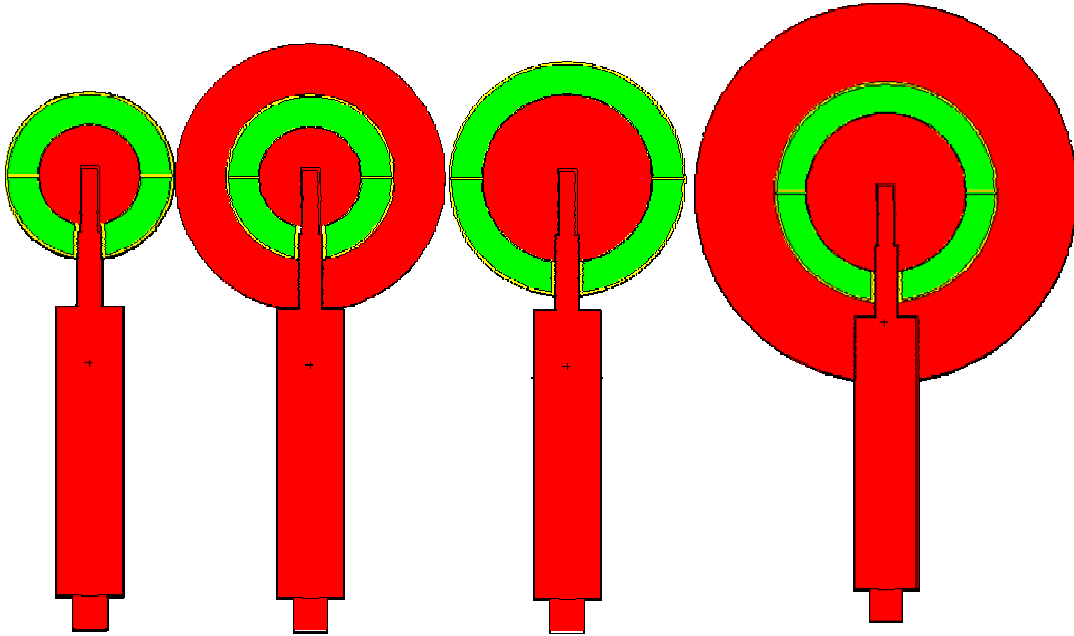


Figure 20. The BSE polyethylene holder system. Red is polyethylene, green is the fill material, and yellow is the aluminum.

When fabricating the BSE spherical shells, one goal was to achieve a nearly isotropic angular response. The system's angular response was modeled by making three different parallel beam geometries. One of these geometries is parallel to the detector chassis which will be called the Z-direction. The second direction is perpendicular to the detector chassis which will be called the Y-direction. The last geometry was with the parallel beam of neutrons incident on the detector at a 45 degree angle between the Y-direction and the Z-direction which will be called the YZ-direction. This can be shown graphically for the 5" sphere with the 12" polyethylene cover in Figure 21.

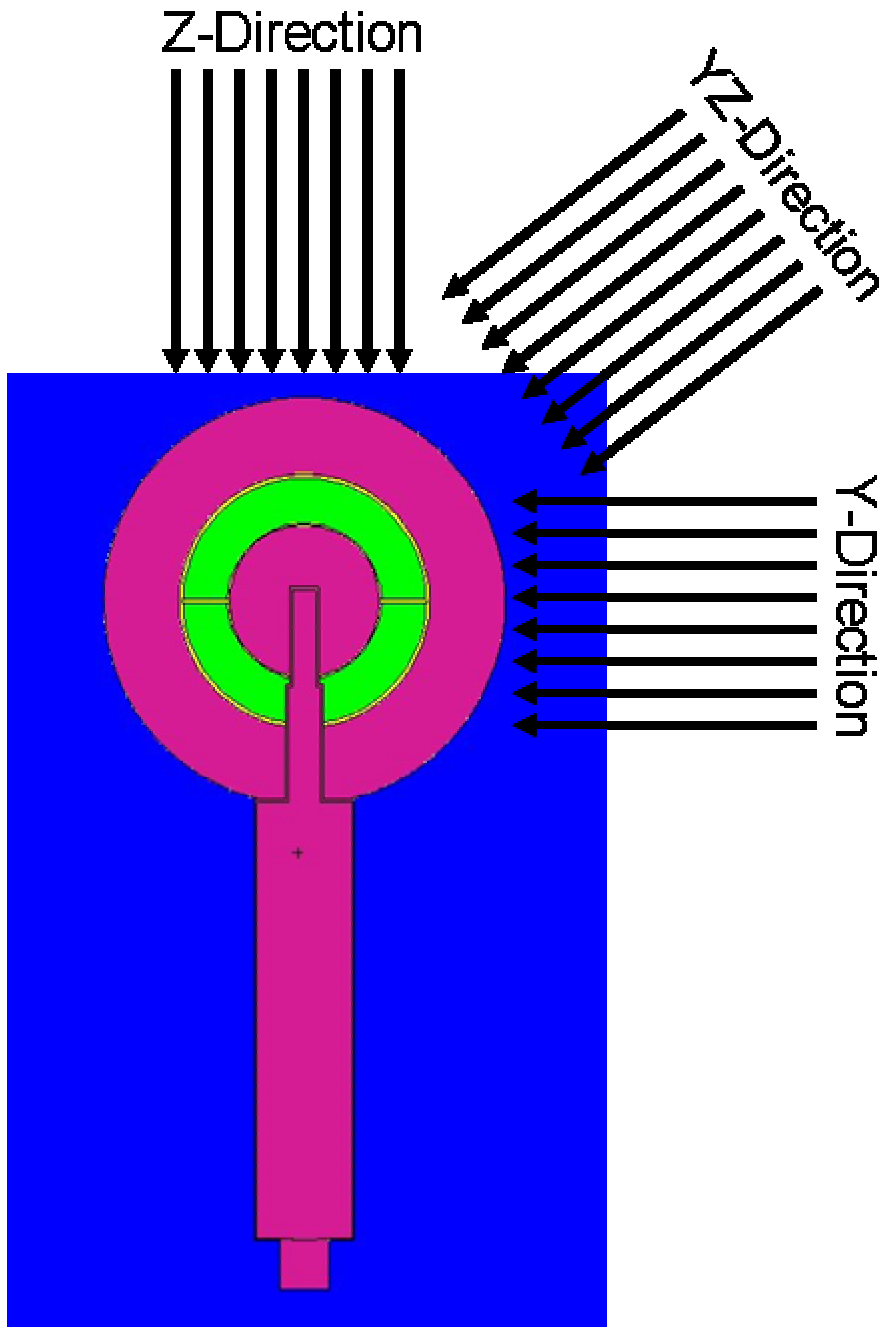


Figure 21. Beam orientation for the generation of the BSS and BSE response matrices.

The response matrix was produced based on 500 equally spaced energy bins in the natural logarithm of the energy; this produces a response matrix with 10 bins per decade in energy. This response matrix can be collapsed to any bin structure the user prefers. The response functions for the standard Bonner spheres using the polyethylene holder with a gold foil are shown in Figure 22. The BSE spheres response for the polyethylene holder and gold foil can be seen in Figure 23. The response functions for extended sphere small assembly (with the 3 inch inner sphere) BSE system response can be seen in Figure 24 and large assemble (five inch inner sphere) are provided in Figure 24 and Figure 25, respectively. In the figures, the term covered means that the polyethylene cover was modeled in place. The polyethylene cover for the small sphere set is 8" in diameter and the large cover is 12" in diameter. As indicated, Figure 22 through Figure 26 correspond to the response functions of incident neutrons in the Y-direction. The remaining two direction's responses for the gold foil detector can be found in Appendix A.

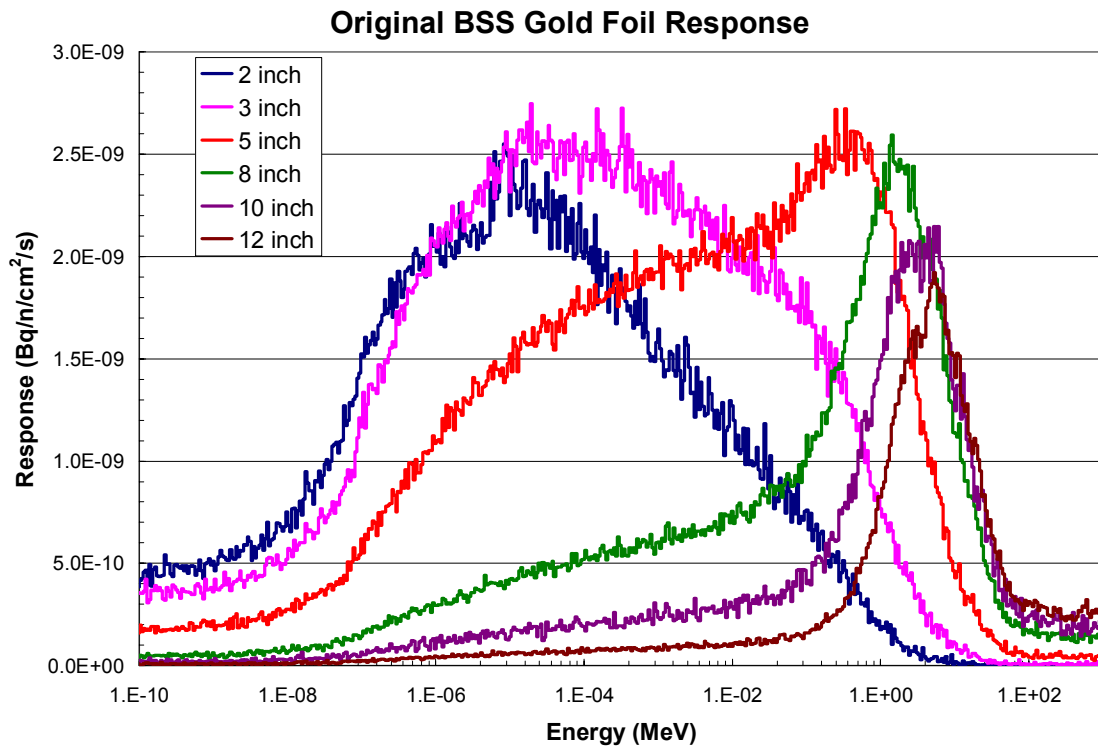


Figure 22. The response of the original BSS system is shown for the Y-direction neutron source.

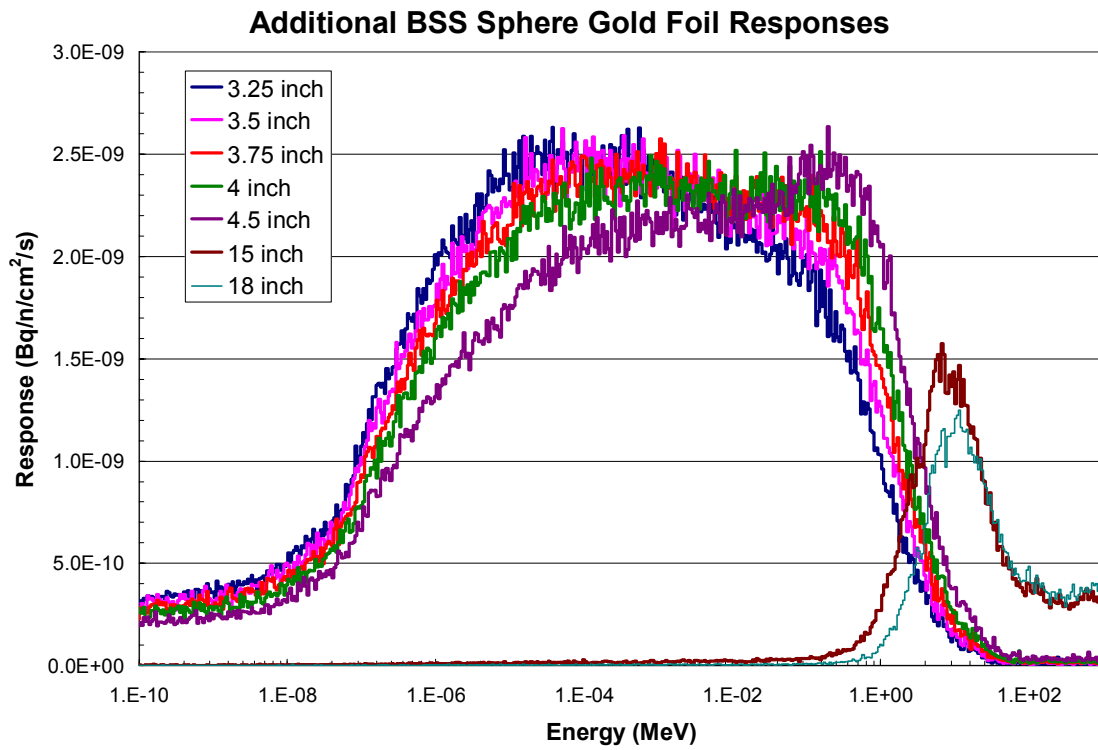


Figure 23. The response of the BSE polyethylene spheres and polyethylene holder is shown for the Y-direction neutron irradiation.

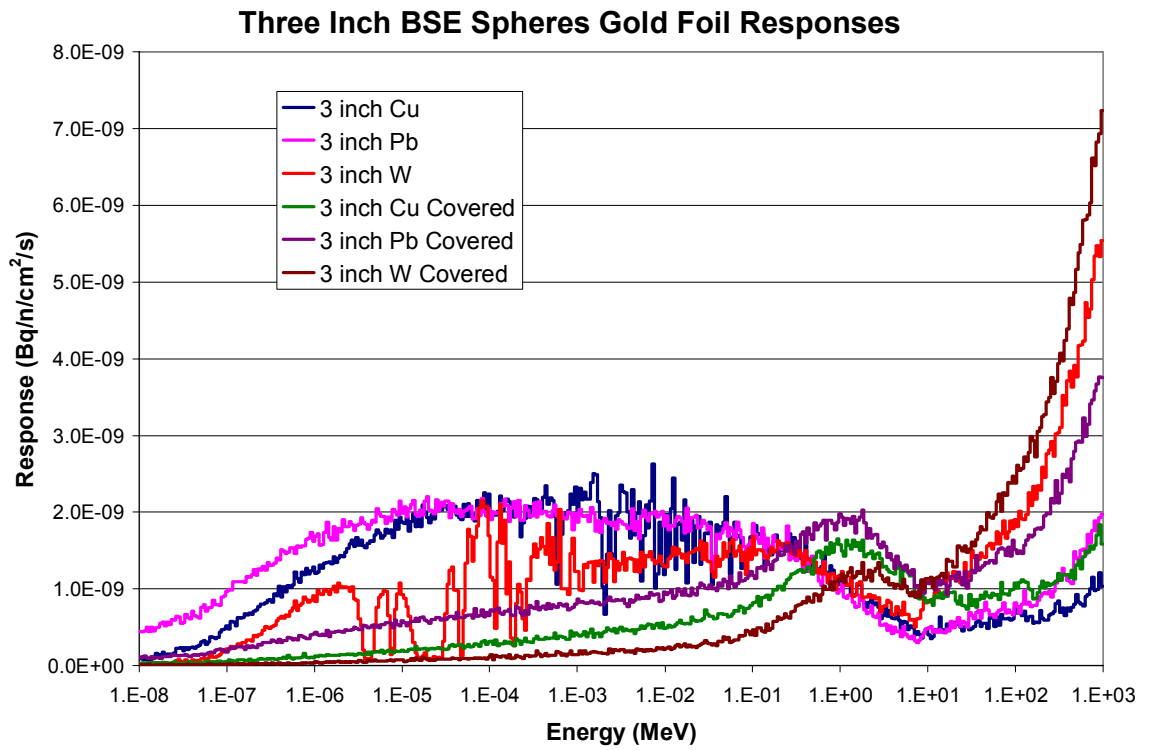


Figure 24. The small assembly (three inch inner sphere) BSE spheres gold foil detector response for the Y-direction neutron source.

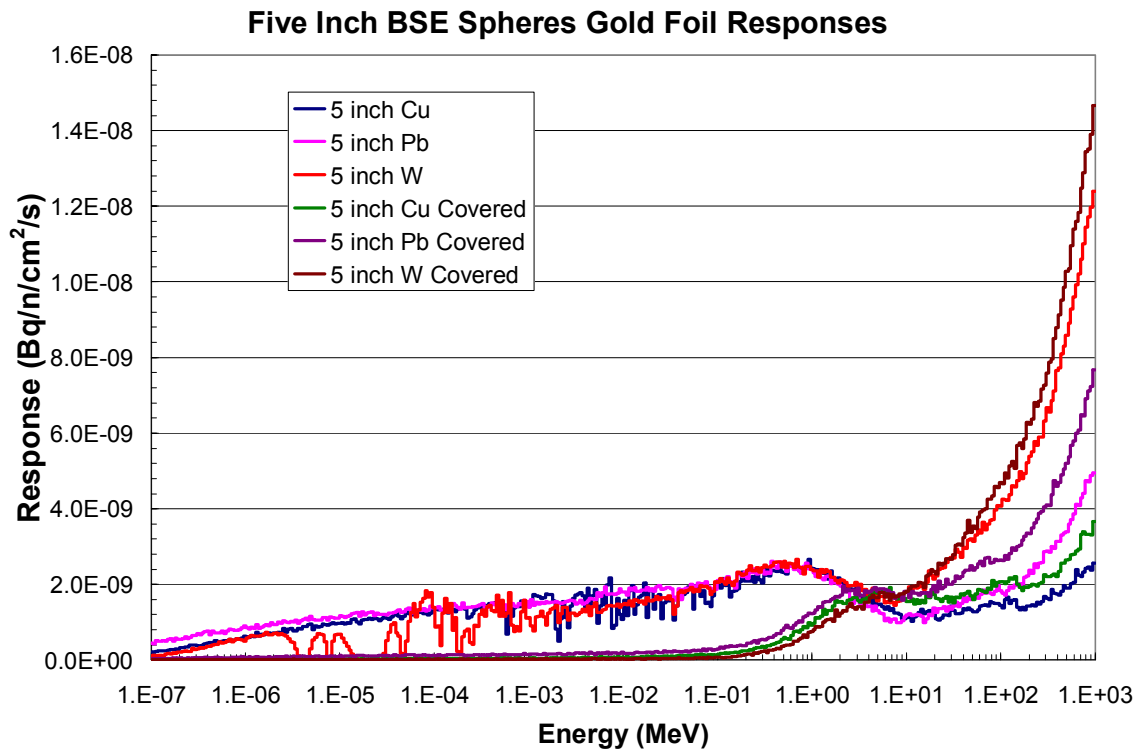


Figure 25. The large assembly (five inch inner sphere) BSE spheres gold foil detector response for the Y-direction neutron source.

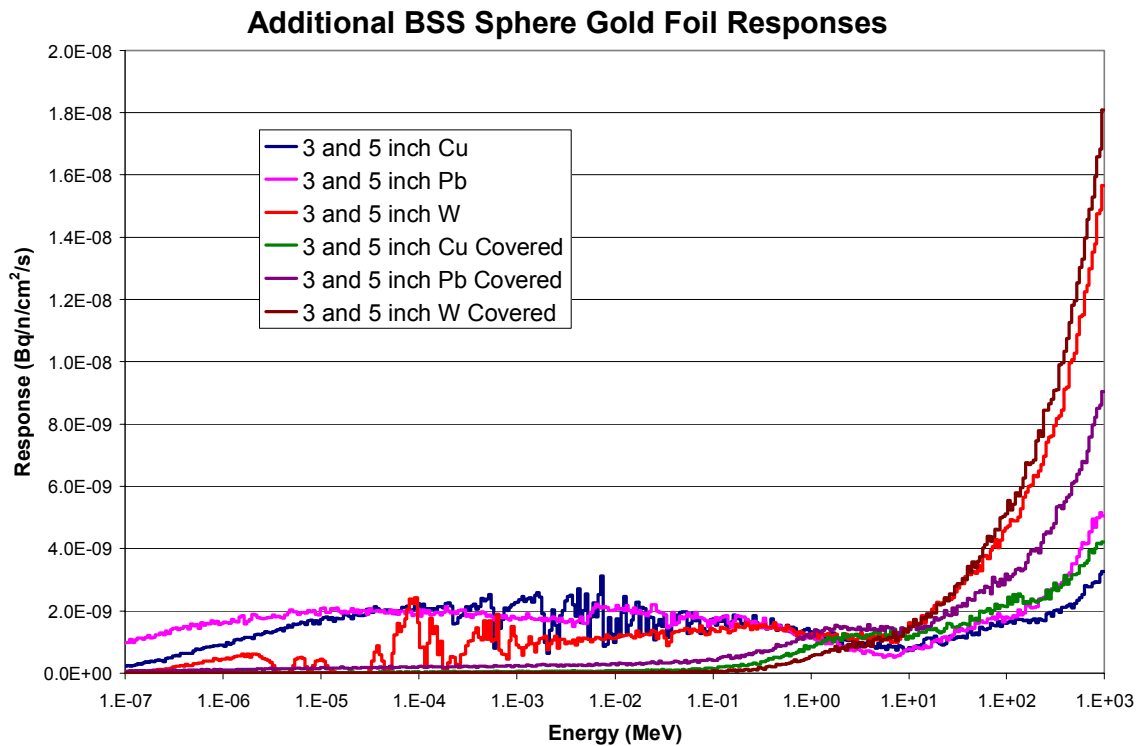


Figure 26. The BSE gold foil detector system is shown which utilizes both the 3” and 5” shells simultaneously for the Y-direction neutron source.

The following section shows the active LiI(Eu) detector system response. The LiI(Eu) crystal is significantly larger than the gold foil is. In addition, since one can measure the direct response of the (n,α) reaction, the irradiation time can considerably shorter to achieve the same statistical uncertainty in the measurement as the gold foil system. As before, shown in Figure 27 through Figure 31 are the corresponding response functions for the five moderator/downscatter combinations for the Y-direction neutron field. The LiI(Eu) detector was also modeled using the three radiation fields. The remaining LiI(Eu) detector responses for the other directions can be seen in Appendix B.

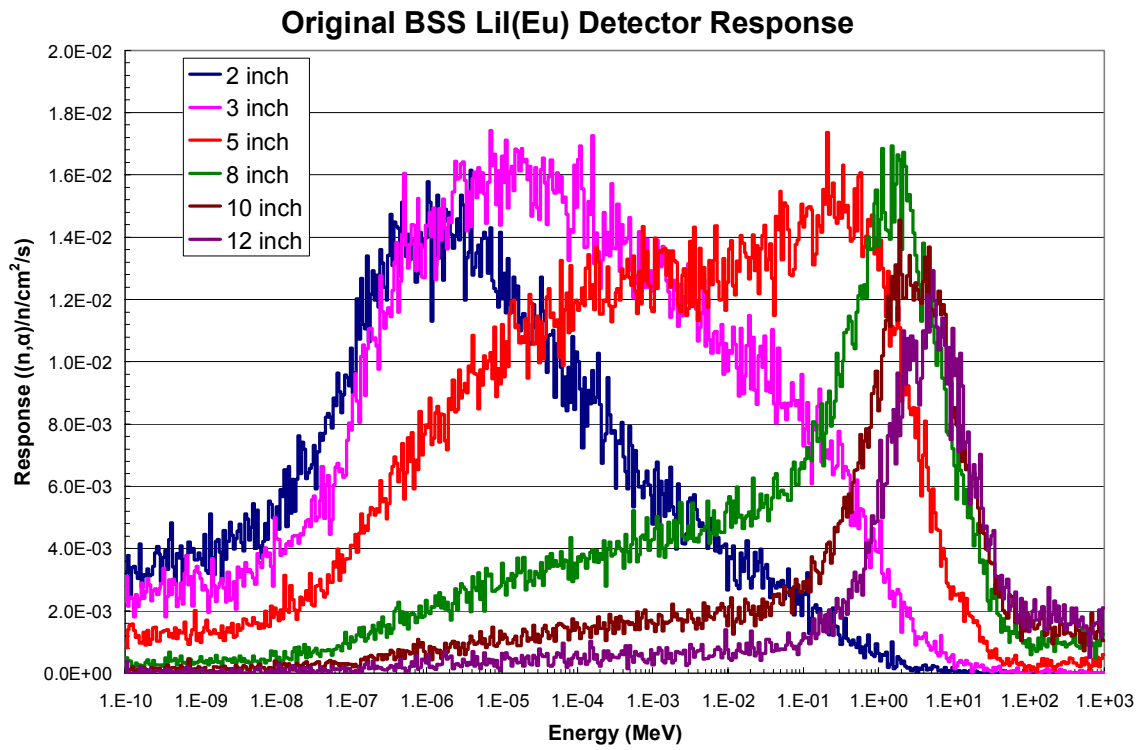


Figure 27. The Lil(Eu) Detector response for the original BSS for the Y-direction neutron field.

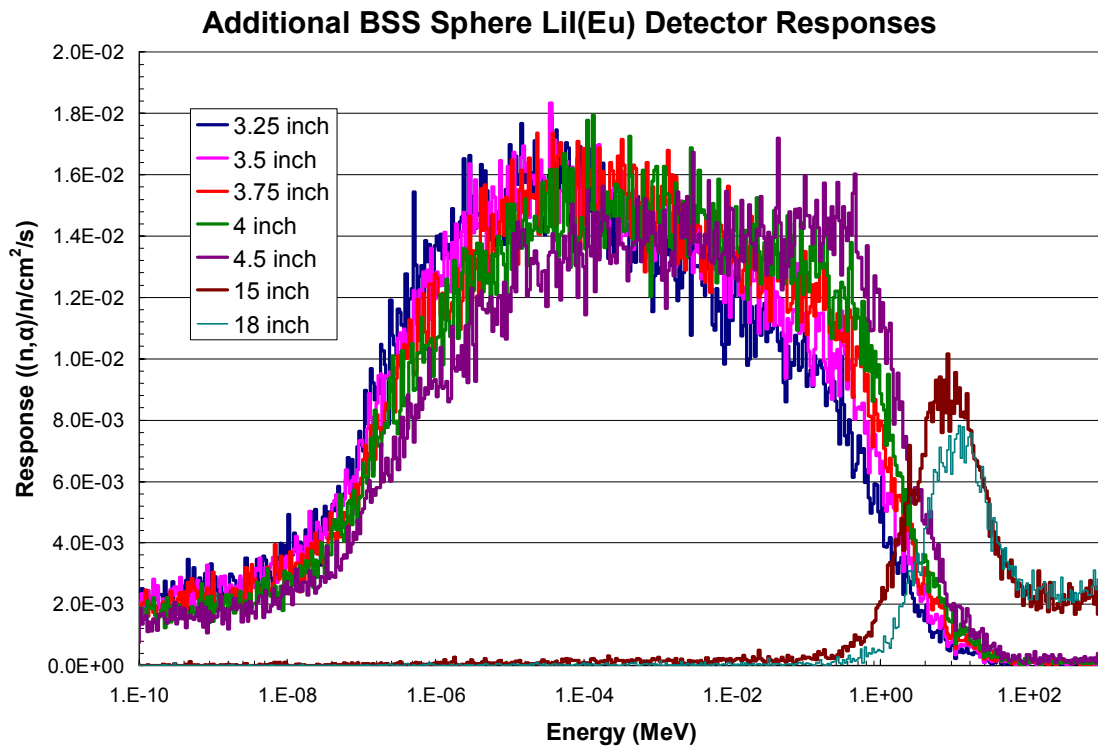


Figure 28. The response of the BSE polyethylene spheres LiI(Eu) detector is shown for the Y-direction neutron irradiation.

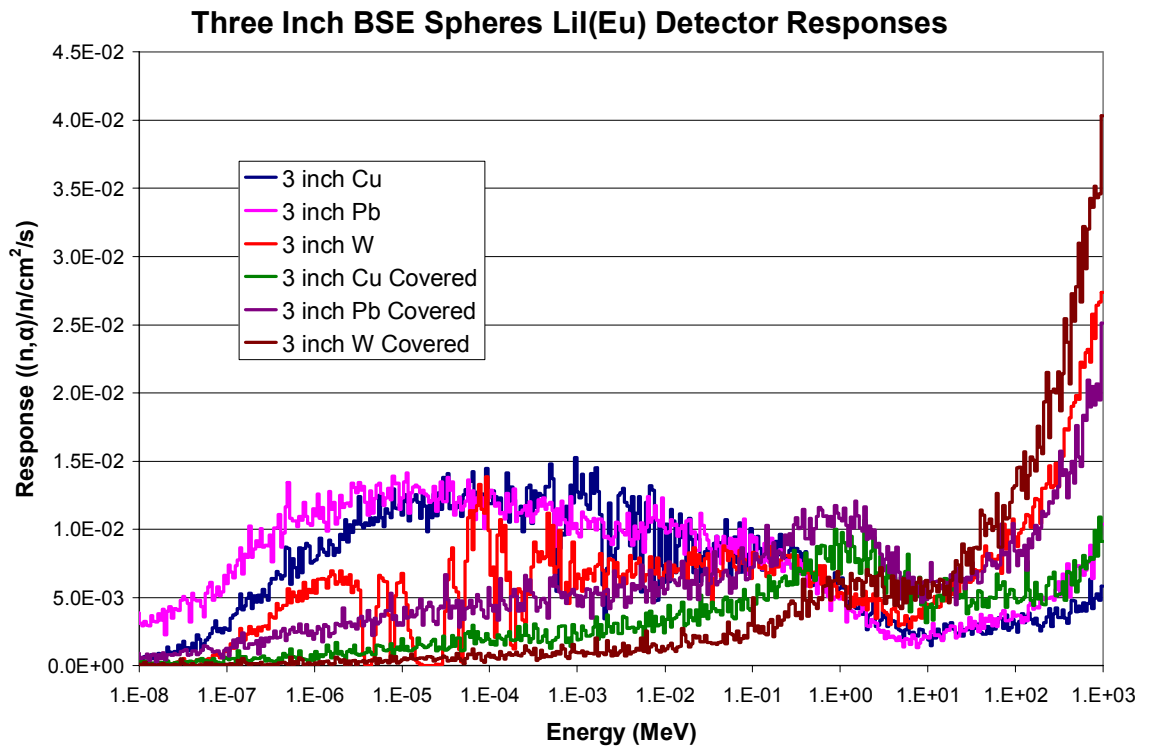


Figure 29. The response of 5” BSE (the large set) spheres LiI(Eu) detector is shown for the Y-direction neutron irradiation.

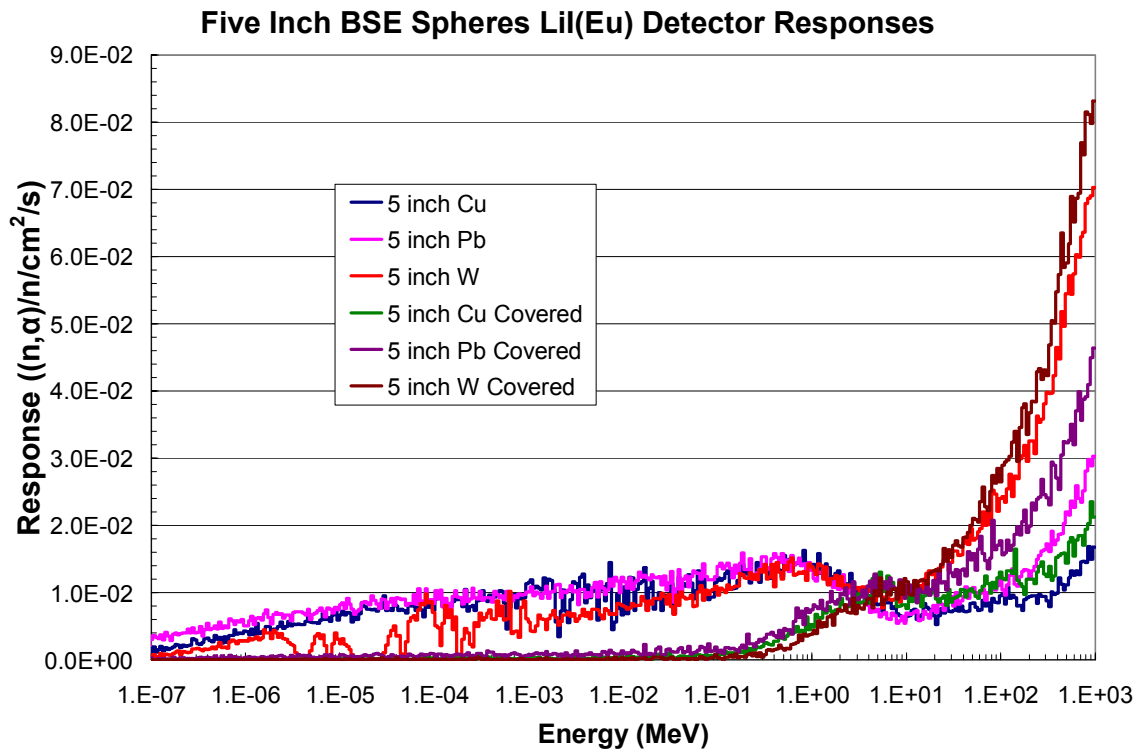


Figure 30 The response of 3” BSE (the small set) spheres LiI(Eu) detector is shown for the Y-direction neutron irradiation.

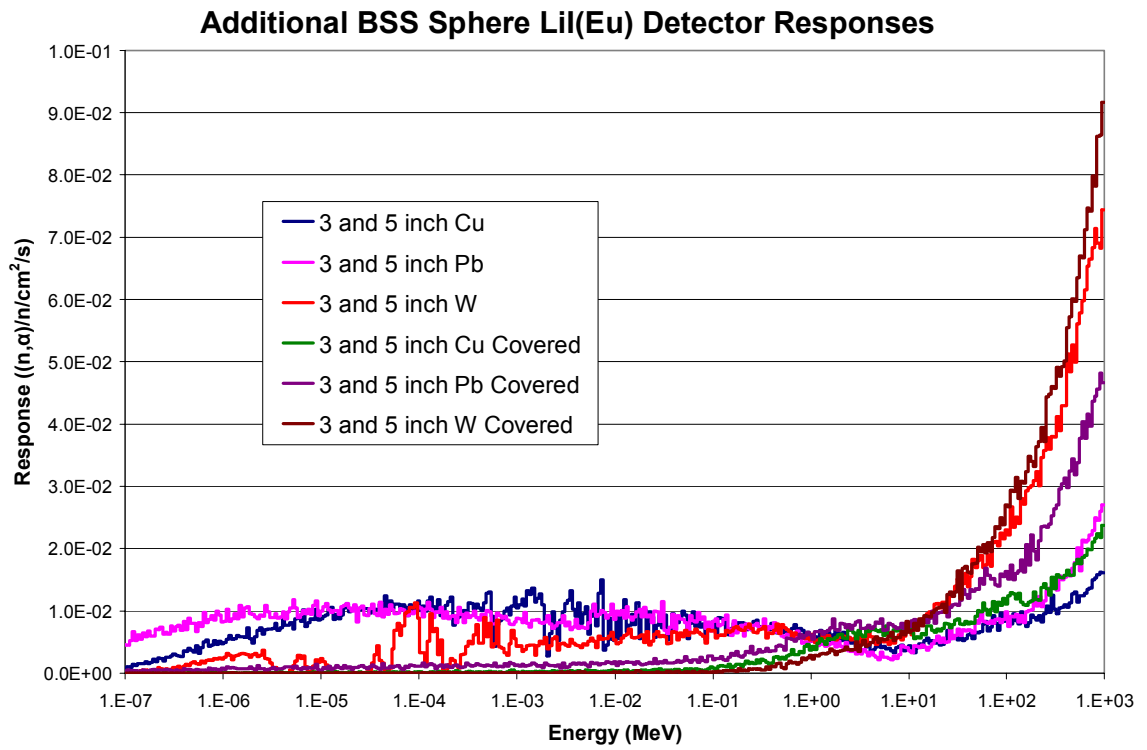


Figure 31 The BSE LiI(Eu) detector system is shown which utilizes both the 3” and 5” shells simultaneously for the Y-direction neutron source.

Experimental Setup Modeling

The BSS and BSE system responses were tested at the WNR LANSCE facility in Los Alamos National Laboratory. The LANSCE neutron source is produced by impinging 800 MeV protons onto a tungsten alloy target (target 4). This target is water cooled and in a vacuum vessel. A picture of the simplified target can be seen in Figure 32. The target has an 8.25 degree upward angle from horizontal which is not shown in the picture. This is so the proton beam which is transported through the target 2 room can clear the target 2 beam lines. The model of the experimental facility was done in two parts, a simplified model in which only the target was modeled in an air atmosphere, and a detailed model in which beam pipes, experimental facilities and collimation was modeled. The simplified model used two cones to subtend an area centered on 15 degrees that opened to 0.1 degrees at 86.6 meters from the center of the target.

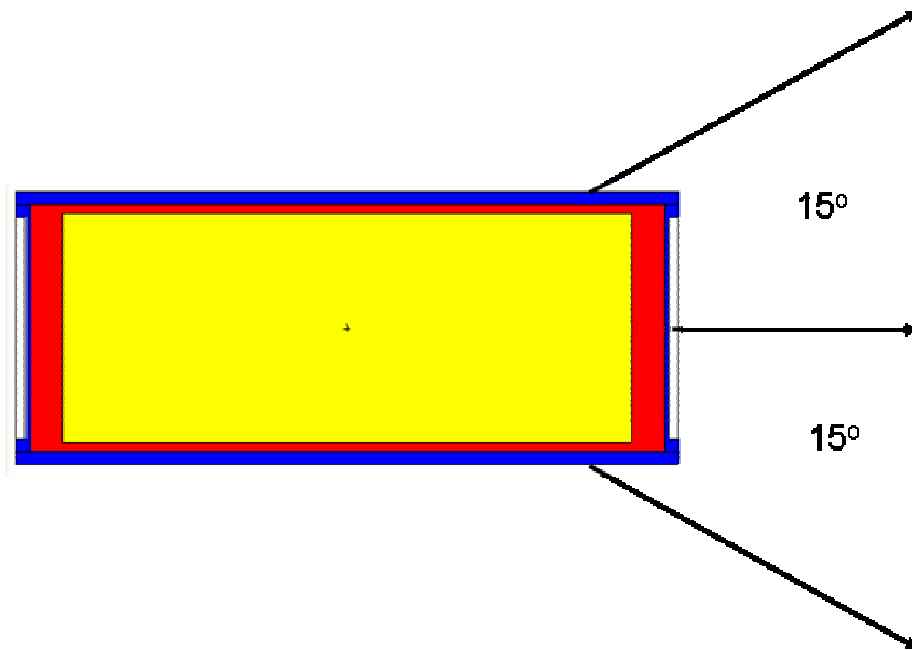


Figure 32. The detailed LANSCE tungsten target.

A surface tally using the surface between the two cones at 86.6 meters was used to determine the neutron energy spectrum at 86.6 meters from the center of the source. The simulation was performed in an atmosphere of standard dry air¹ at an appropriate density for the altitude at Los Alamos. A comparison of the calculated neutron spectrum (from this model) to the neutron spectrum measured with the TOF detector can be seen in Figure 33. In Figure 35, a comparison of the calculated spectrum to that measured in September of 2007 TOF data is shown. The TOF data is normalized to the number of protons incident on the target. This normalization used the data shown in Table 5 and assumes less than 2% beam loss between target 2 and target 4^{li}.

Table 5. The accelerator operating parameters for the two measurement trips

Operating Parameter	July 2007	September 2007
Beam Frequency (Hz)	40-60	40-60
Macropulse Length (μ s)	625	625
Micropulse Spacing (μ s)	1.8	1.8
Beam Current at target 2 (μ A)	1.6-1.8	1.6-1.8
Protons / micropulse (10^8)	2-3	2-3

Neutron Energy Distribution from LANSCE

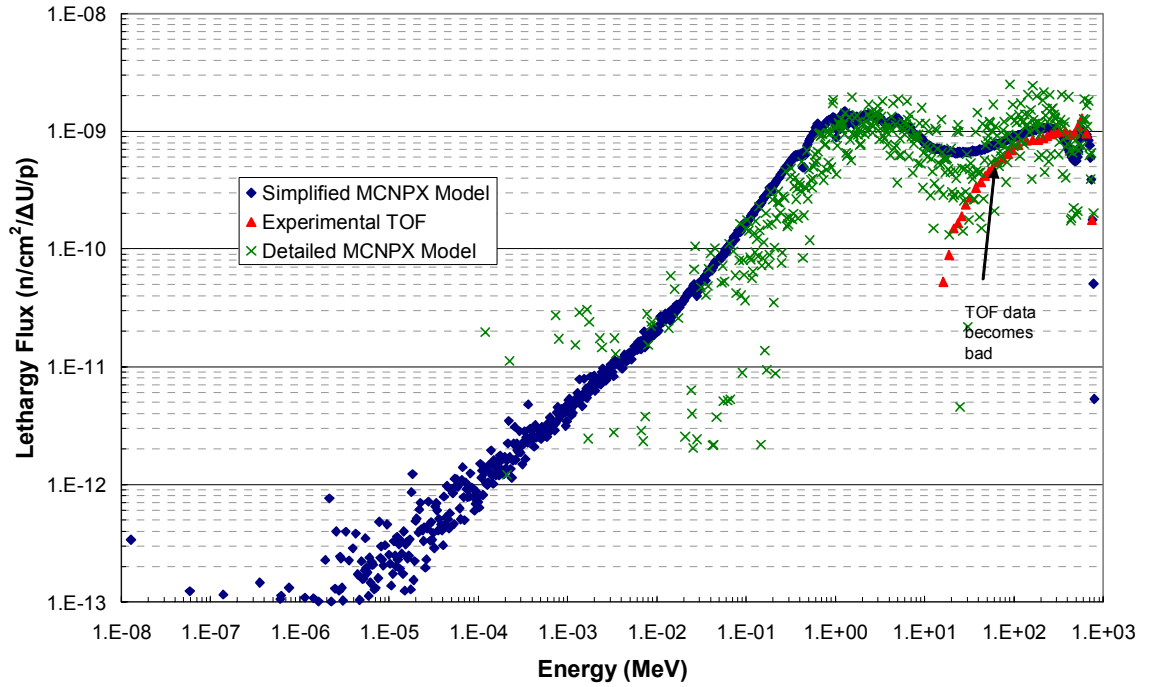


Figure 33. Calculated (simplified model) and experimental neutron spectra from LANSCE.

Neutron Energy Distribution from LANSCE

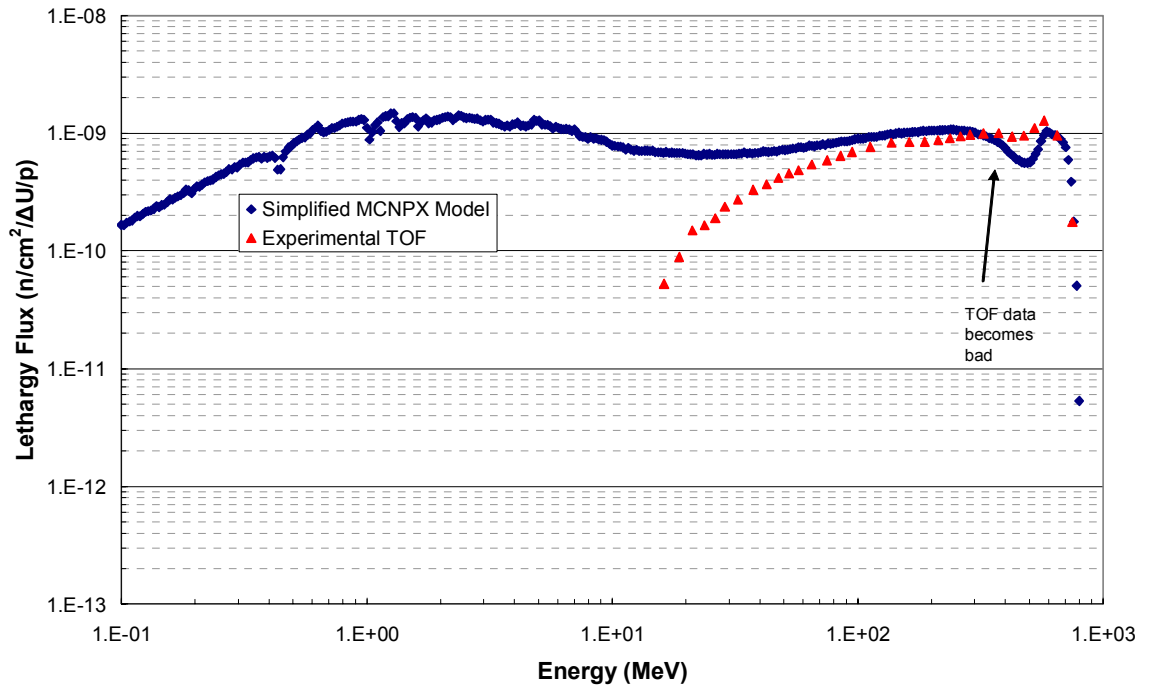


Figure 34. Calculated (simplified model) and experimental neutron spectra from LANSCE blown up to highlight the region above 100 keV.

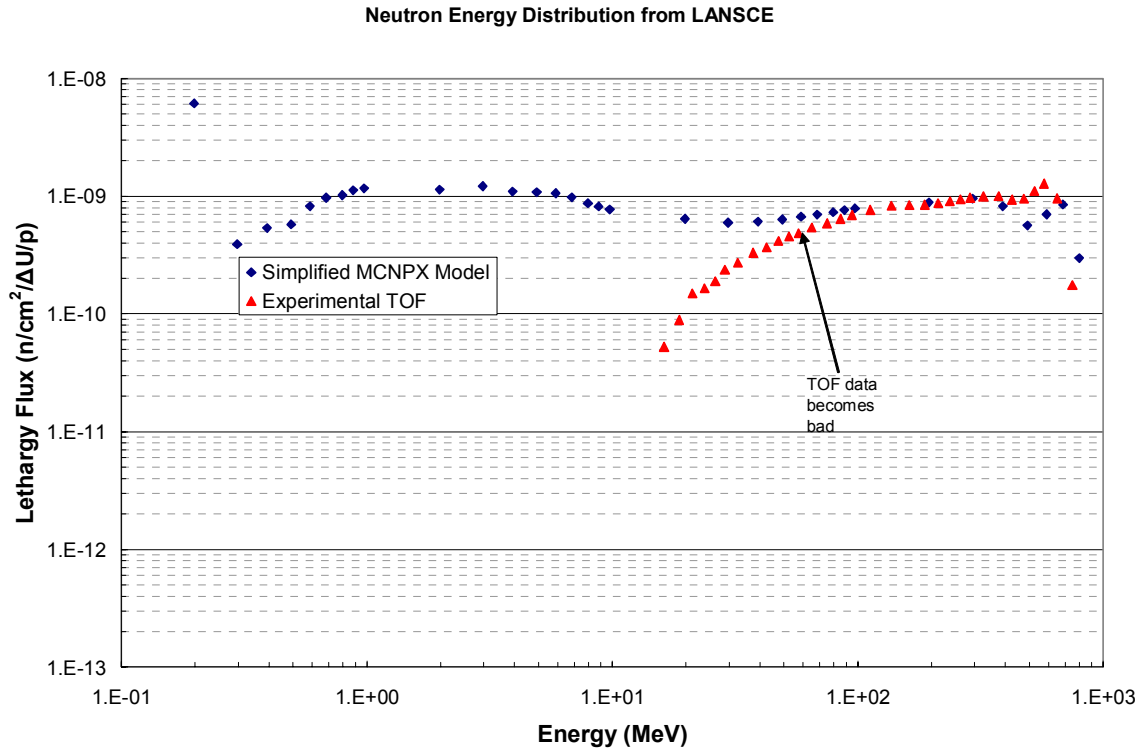


Figure 35. Calculated (simplified model) and experimental neutron spectra from LANSCE plotted with collapsed energy groups. The error bars are smaller than the figures.

In addition to the simplified model, a fully detailed model was produced. The fully detailed model attempted to add the collimation that was present in the experimental setup. This model attempts to add the details of the experimental setup discussed in detail in Chapter 5, Experimental Validation. A diagram of this setup can be seen in Figure 39 and Figure 40 with the corresponding spectrum provided in Figure 36 and Figure 51.

Neutron Energy Distribution from LANSCE

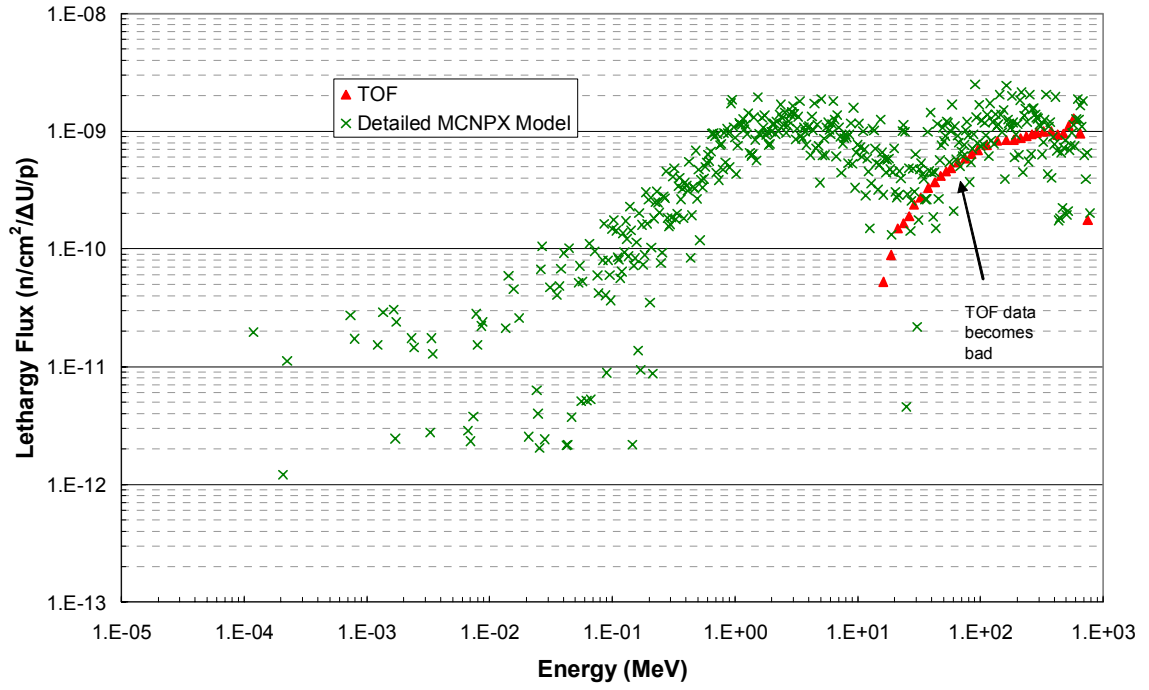


Figure 36. The results of the detailed MCNPX model neutron spectrum at the 86.6 meter experiment location.

CHAPTER 5

EXPERIMENTAL VALIDATION

General Experimental Layout

To validate the calculated responses of the detector systems, the BSS and BSE measurements were performed at the WNR LANSCE facility and tested at the 90 meter experiment station on the 15 degree right flight path. An overview of the WNR facility can be seen in Figure 38.



Figure 37. The experimental LANSCE facility in Los Alamos NM.^{lii}

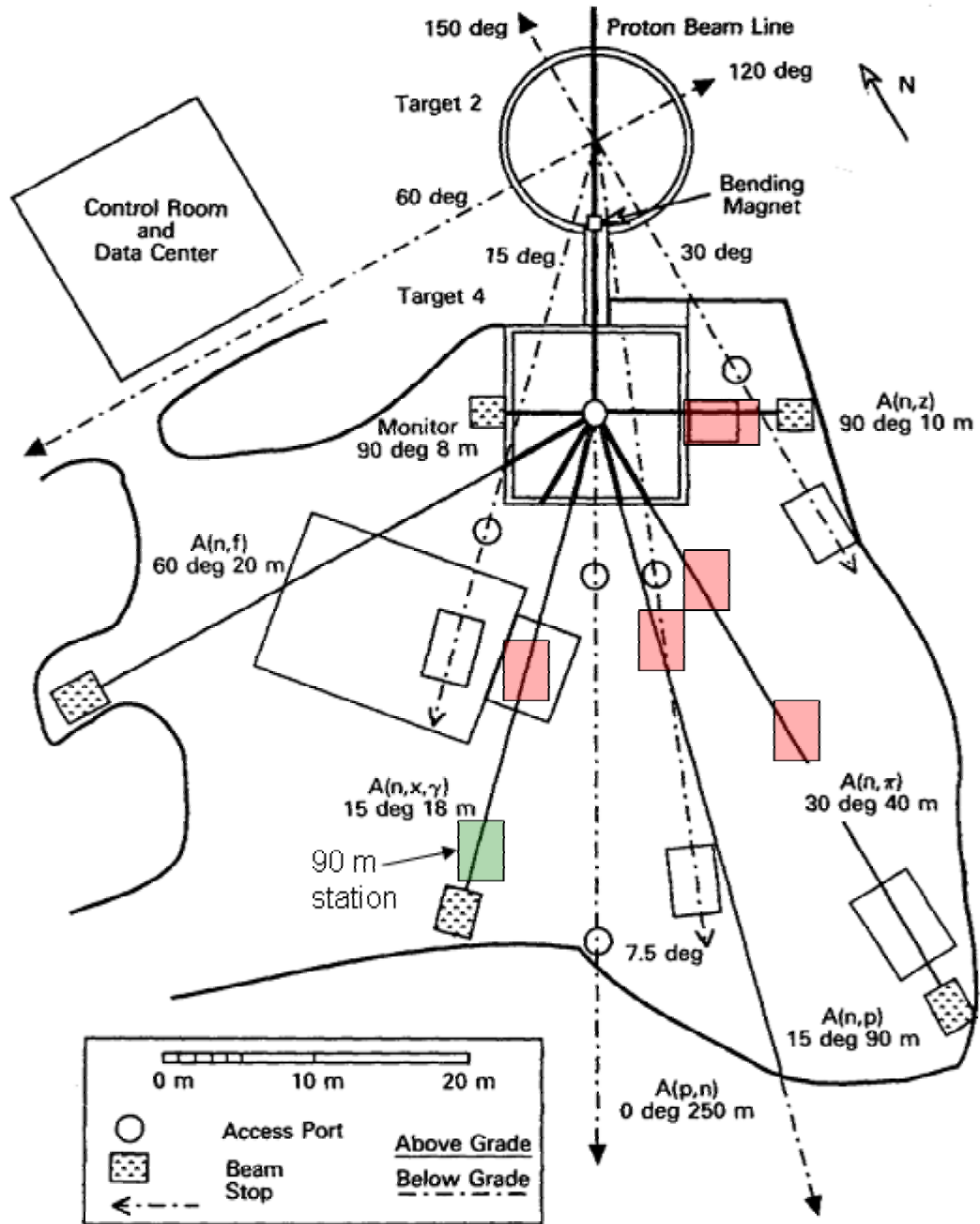


Figure 38. The experimental facility layout of the WNR LANSCE facility.^{liii}

The experimental facility diagram can be seen in Figure 39 and Figure 40. Several experimental components were needed to obtain the required information needed to validate the BSE system. These components included the active LiI(Eu) detector

system, the passive gold foil detector system, the time of flight system, a HPGe detector for counting the gold foils, and a beam monitor. A picture of the experimental setup can be seen in Figure 41.

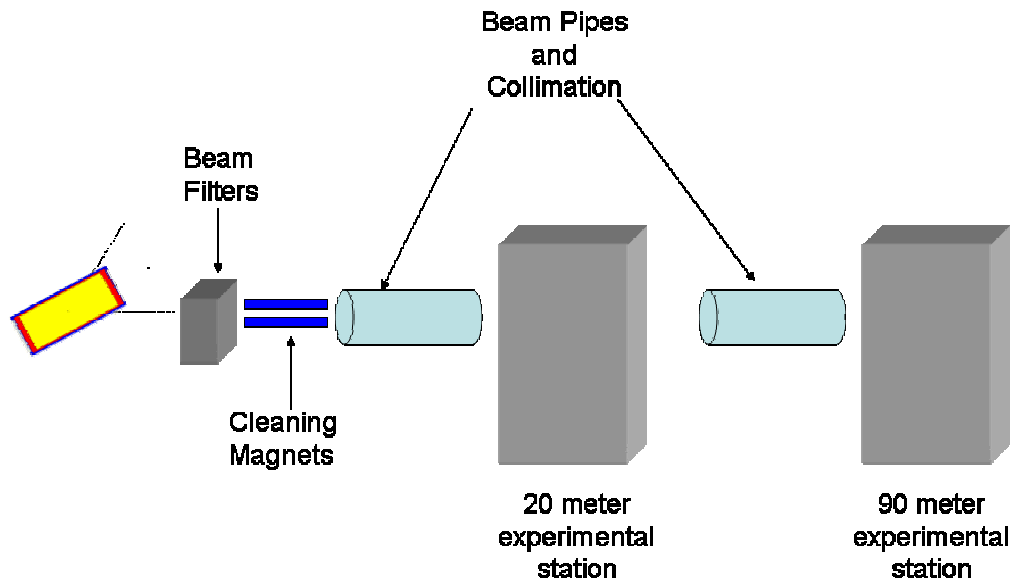


Figure 39. Flight path 15R facility layout schematic.

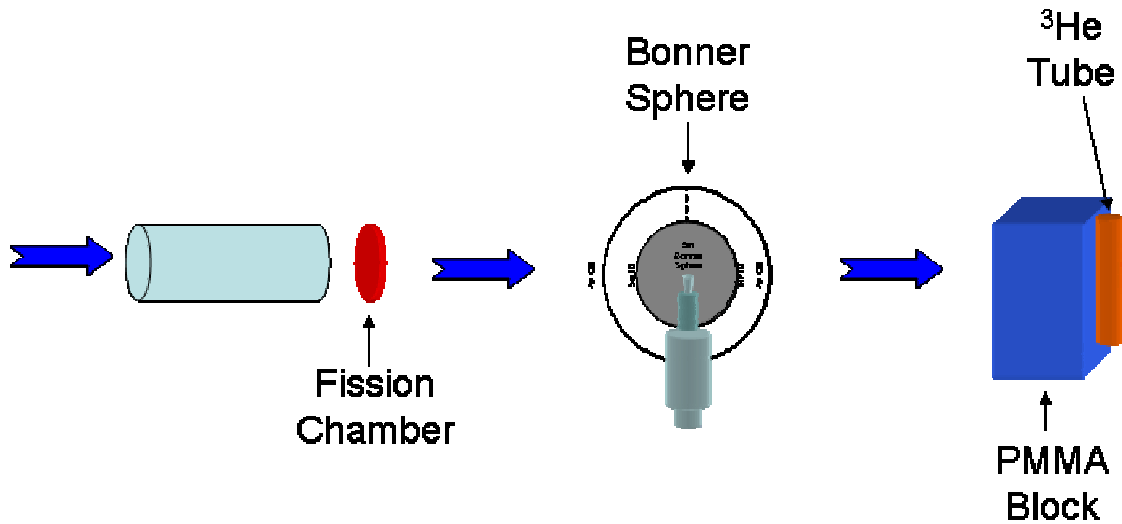


Figure 40. Experimental setup schematic for the equipment in the 90 meter experiment station

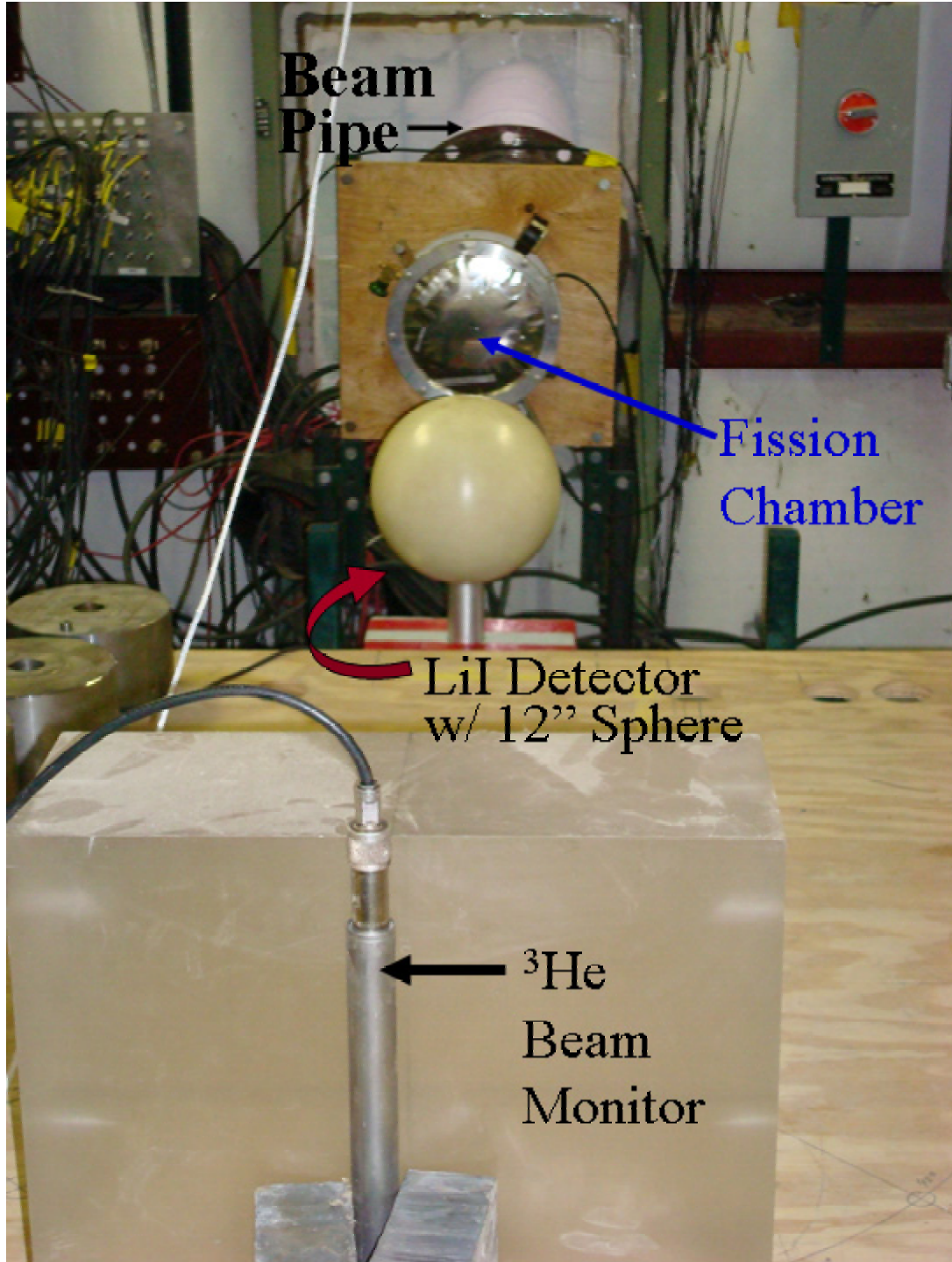


Figure 41. Experimental setup for validating the BSE and BSS systems at the 90 m experiment station on the 15 degree right flight path.

The Active LiI(Eu) Detector System

The active LiI(Eu) detector system is comprised of the LiI(Eu) scintillator and supporting equipment. The nominal operating voltage for the LiI(Eu) detector was 800 V. This is a detector specific parameter and was determined by gamma discrimination ability and desired pulse amplification. The detector is connected by a single SHV cable to the preamplifier. The high voltage was supplied through an Ortec model 142-IH preamplifier which decouples the signal from the high voltage supply. The preamp signal was routed through an electrically shielded coax cable bundle to an Ortec model 572A amplifier. The amplified output was then brought into a TRUMP 2k MCA card in a Pentium –IV computer. The computer, NIM module, high voltage power supply, and amplifier were located below the beam line behind a large shielding wall of steel and concrete. The computer was operated from the measurement trailer by use of a small *ad-hoc* computer network and VNC. In an attempt to limit the pulse pile up problems encountered in a high flux location, the busy signal was used off of the amplifier to the TRUMP card (see Figure 40). The output of the TRUMP card was a spectrum as seen by the PMT. The essential detail of this spectrum is the (n,α) reaction peak from the ${}^6\text{Li}$.

One of these peaks can be seen in Figure 42. In this high count rate ball, a small fraction of pulse pileup was observed. This was minimized using the busy circuit on the amplifier. The existence of pulse pileup after the inclusion of the busy circuit is usually indicative of simultaneous light emissions being collected in the PMT. The net area of this peak was then used to measure the amount of (n,α) reactions as a function of beam on time and live time.

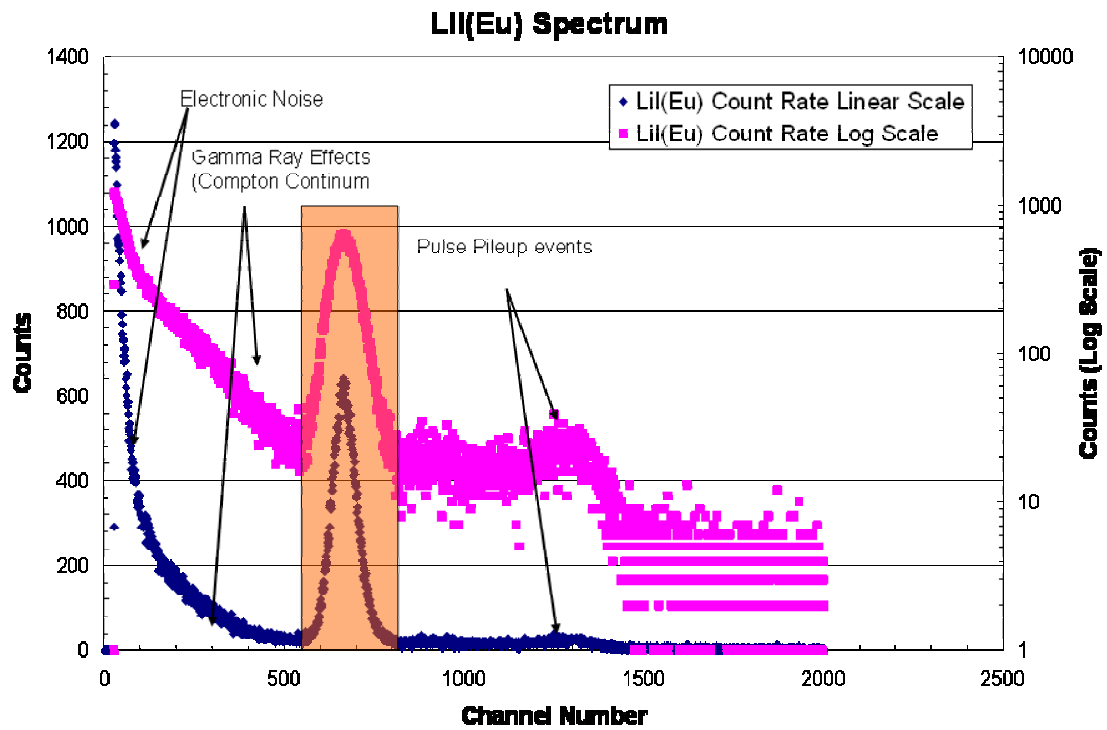


Figure 42. A LiI(Eu) measured spectra. The area in the red box is the marked ROI. The counts are displayed on both a log scale (pink) and linear scale (blue).

The Passive Gold Foil System

The passive system places a gold foil on top of the polyethylene holder and is then inserted into the sphere. The foils were held in place by a piece of cellophane tape. The detectors were positioned for the Y-direction irradiations by a styrofoam block. The styrofoam block was kept below the beam and due to its low density has very little impact on the measurement. For the Z-direction and YZ-direction, a wooden holder was built to support the LiI(Eu) and polyethylene holders. The wooden holder was capable of supporting the detectors at both 45 and 90 degrees to the beam. This holder can be seen in Figure 43. Once the foils have been irradiated (typically 1-5 hours), they need to be counted to determine the activity of the foil. This was done using a HPGe detector as seen on page 19.

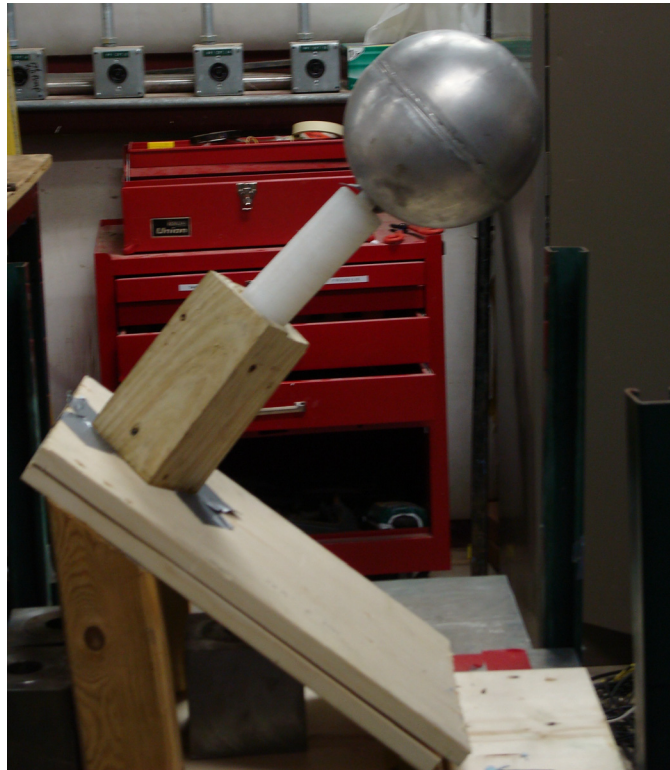


Figure 43. The wooden holder set for the YZ-direction which makes the beam incident on the detector at 45 degrees.

The HPGe Detector Setup

The HPGe detector was set up inside the measurement trailer to provide a low background counting environment. This was described in Chapter 3. Refer to Figure 8. The detector was calibrated using a NIST traceable multi-line gamma ray point source. This was obtained by taking an hour long count of the NIST point source. After the acquisition was complete, the integral of the counts registered in the photopeak was compared to that of the number of photons emitted during that hour. The energy calibration curve can be seen in Figure 44.

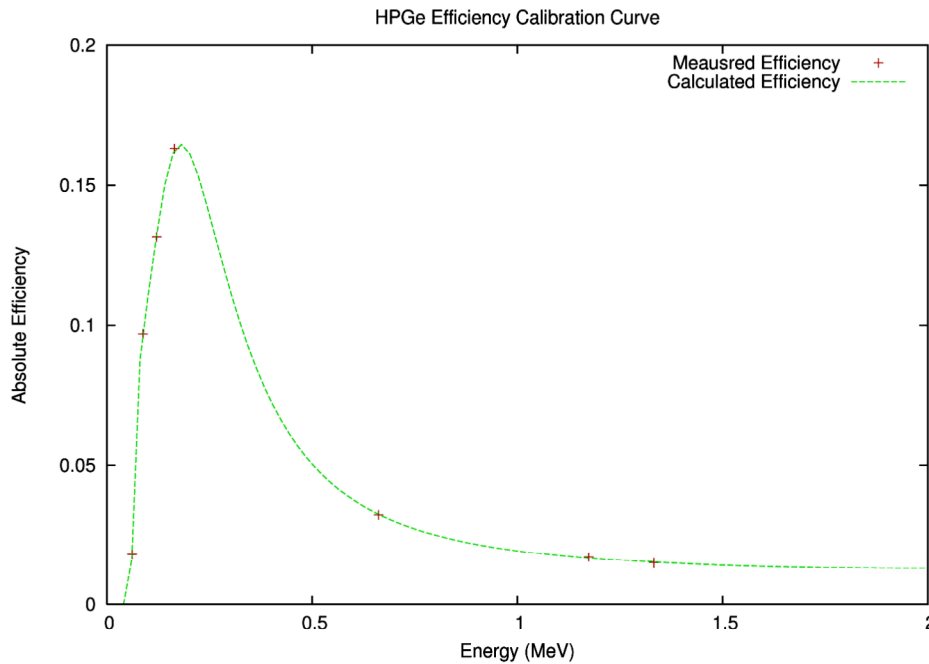


Figure 44. The energy calibration curve for the HPGe detector used on the WNR LANSCE trips.

The detector was found to have a constant response over the detector area that is subtended by the foil. A paper with a circular outline of the foil was taped on the top of the detector to insure proper foil placement. Measurements at Georgia Tech for the HPGe detector were made to determine if a position correction was needed. Several measurements across the foils surface position were made. Due to the constant response of the detector over the foil area, no surface area correction is needed. Also, since the gold foils counted on the HPGe are thin, there is little self attenuation of the emitted radiation. There is no volume correction for self attenuation was needed. Additionally, there is no self-shielding correction to thermal neutrons since the foils are thin in comparison to the mean free path in the gold detector material. The HPGe was controlled by a TRUMP 8k card and a Pentium – IV computer. This computer was also integrated into the *ad hoc* computer network and controlled remotely. The TRUMP card produced a spectrum that was used to determine the activity of the gold foil. To do this, the 411-keV peak was integrated to determine the gamma emission rate at the time of counting. Shown in Figure 45 is a typical spectrum of an activated gold foil.

HPGe Sample Spectrum

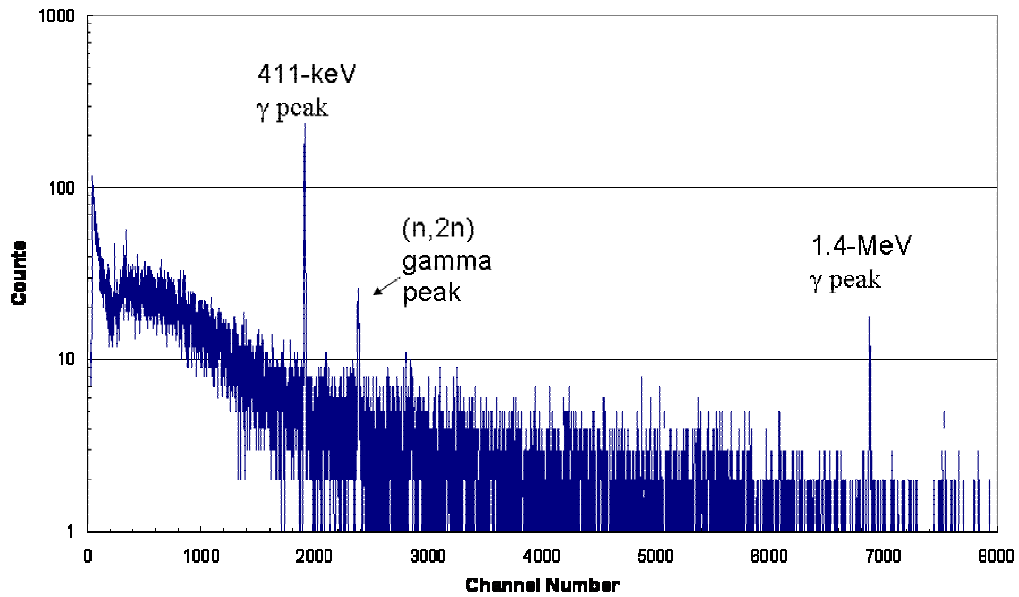


Figure 45 An example HPGe spectrum from the counting of the gold foils following the irradiation of the 5” tungsten covered sphere. The counts are plotted on a log scale

During the two experimental periods lasting seven days each, the detector was checked daily to ensure the detector had not gain shifted over the course of the day. A continual 1.4-MeV gamma ray line was present in most spectra. This is due to the high ^{40}K background level in the experimental area. This peak provided a secondary reference for a long counting period.

Beam Monitor

The beam monitor was used to insure that the beam intensity was known as a function of time during the irradiation period. Both the active and passive systems rely on an accurate knowledge of the beam intensity. The beam monitor used in this work was fully described in Chapter 3. Using software provided by Ludlum, the scalar was set for 1 second integration periods. This list was used to determine the beam on time and relative beam intensity. Since the beam monitor was set behind the BSS or BSE sphere, it relied on scattered and transmitted neutrons to produce counts. The beam monitor was shadowed by the sphere. For this reason, only the relative intensity during a run was able to be recorded. This however was sufficient data record beam fluctuations. An example beam monitor plot is shown in Figure 46.

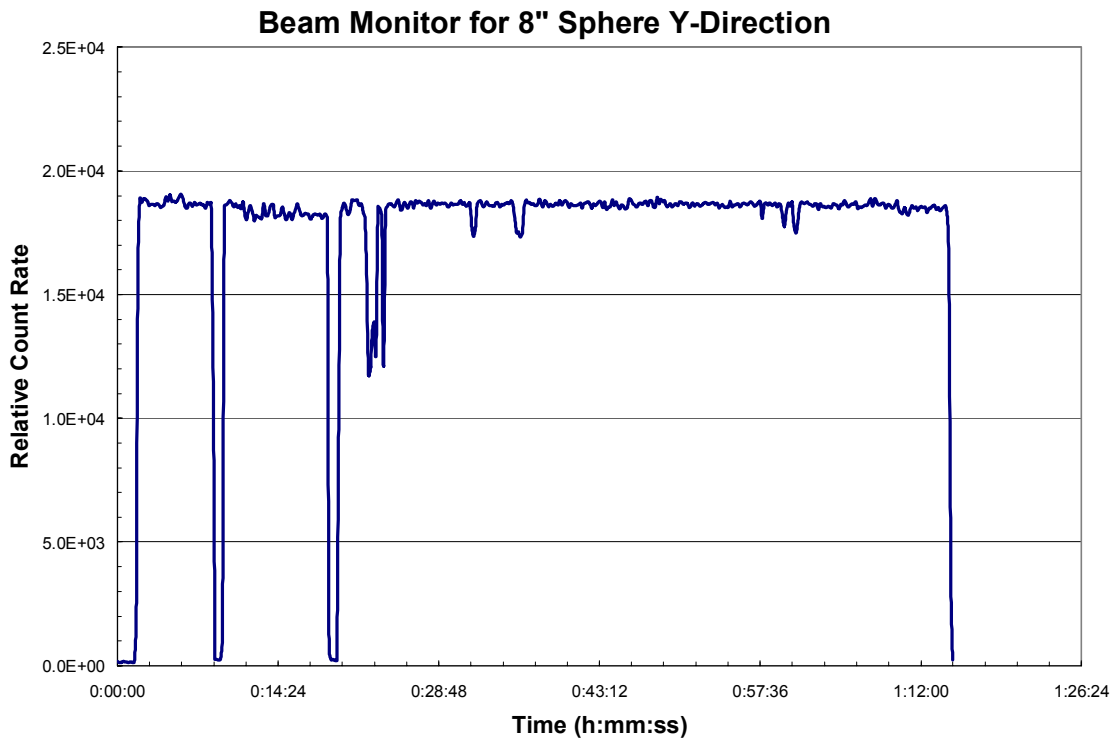


Figure 46. An example beam monitor plot used to normalize the beam up time for the activation measurements.

In Figure 46, there are several drops in the relative count rate. This was due to beam fluctuations. On this day of the experiment, users of the proton radiograph (PRAD) facility were making proton shots. During these times, the entire LANSCE beam was diverted to PRAD and shut down the beam for several seconds. These up and down times were used with Equation 12 to determine the activity. Due to the long half life, this improved the uncertainty of the measurements but did not have a drastic effect on the production rate.

Time of Flight Data

A time-of-flight (TOF) detector system was provided by WNR serviced to monitor the neutron beam during the experiments. The TOF detector is described in detail in Chapter 3. The lowest energy the TOF system could read was 30 MeV. This was due to the long flight path and the very fast timing of the accelerator. In addition TOF data having energies between 30 MeV and 60 MeV had low statistical certainty. Above 60 MeV, the statistical uncertainty was below 1%. Therefore, TOF data above 60-MeV can be accurately used to determine the high energy neutron flux. The TOF spectra are previously shown in Figure 33 and Figure 35

Beam Area Imaging

The neutron image plates were used to determine the spatial profile of the neutron spectra. Two main image plate images were used in the analysis of the data. The spatial flux profile from the July 2007 measurement can be seen in Figure 47, while the image from the September 2007 measurement can be seen in Figure 48. The fission chamber for the September 2007 measurement was aligned more closely to the center of the neutron field than during the July 2007 measurements. The black circle was drawn by

hand as a reference to the inside of the retaining ring of the fission chamber to aid in the integration. A correction factor of 0.887 was used since part of the active foil area was outside the useful beam.

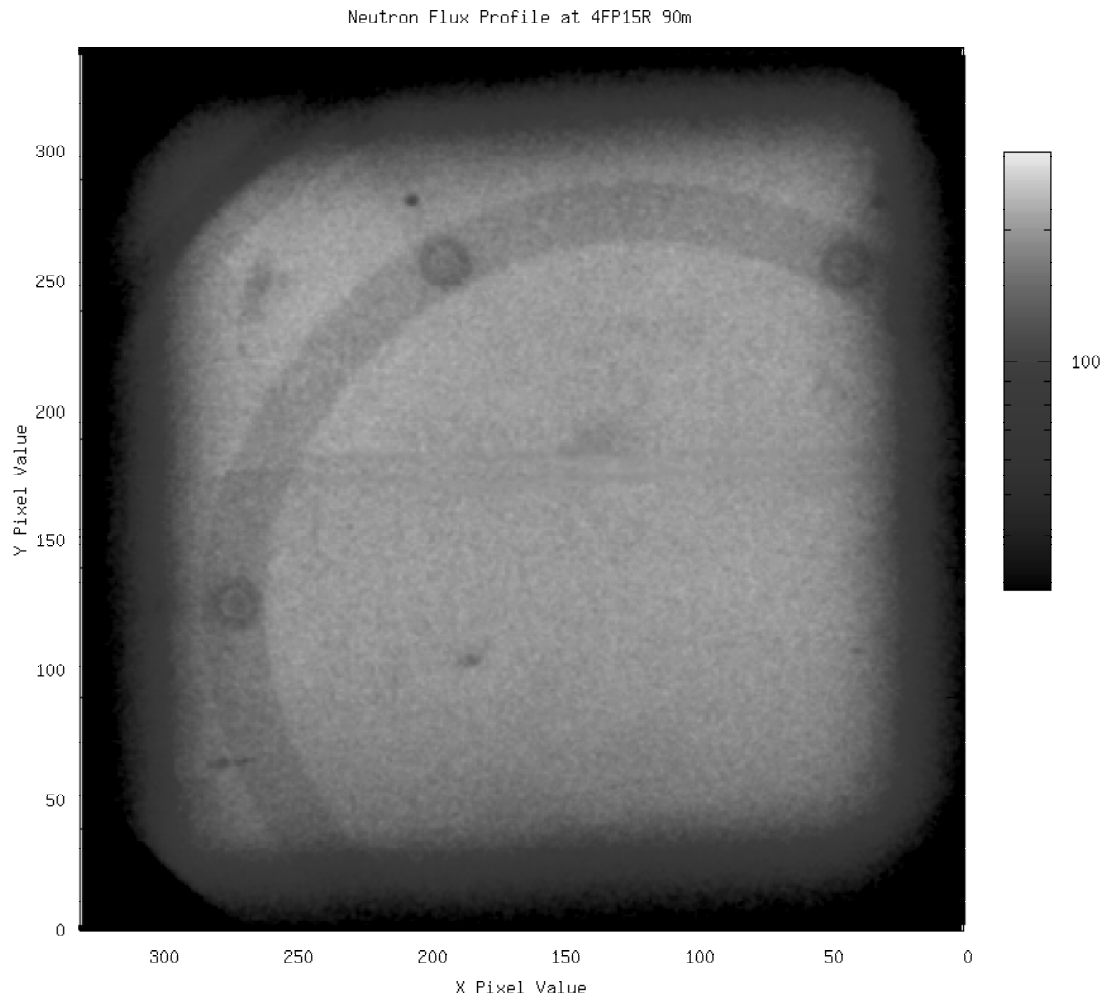


Figure 47. The July 2007 spatial neutron flux profile. The pixel values ranged from 0 to 255.

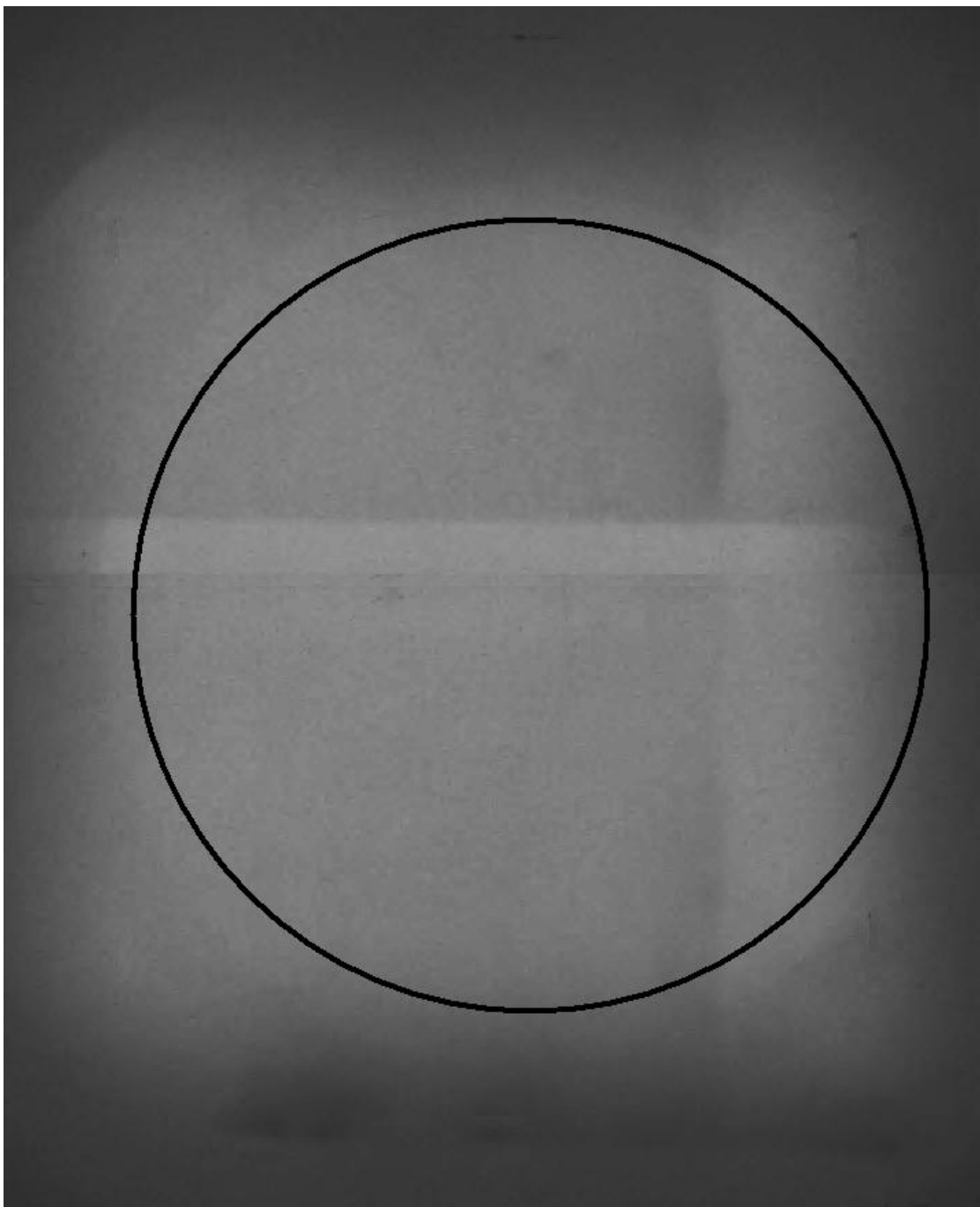


Figure 48. The September 2007 neutron flux profile image.

A computer code was written to extract the spatial flux density using the image plate intensities. This was used to determine the percentage of the flux that was incident through the fission foil area. The image plate data were used to calculate correction factors which are necessary because the ^{238}U foil inside the TOF chamber has as a finite size and the beams were large. The scaling factor is fraction of the neutron beam that was counted by the fission counter as a ratio of the total beam area. This value can be multiplied by the fluence rate recorded by the fission chamber to determine the absolute fluence rate incident on the detector. These correction factors for the flux recorded by the fission chamber to the total flux were found to be 2.06 in July 2007 and 1.88 in September 2007. These values were obtained by taking the net integral of the pixel value under the area subtended by the fission foil to the net area of the total spectrum. The area of the foil was found by locating the flux depression caused by the fission chamber retaining brackets.

Unfolding Considerations

During the unfolding process, the high energy tail should be forced down. All of the BSE spheres have increasing sensitivities as the energy increases and places neutrons at higher energies. Extra care must be taken to ensure that during the unfolding process that the high energy tail artifacts do not appear in the unfolded spectra. This can be ensured by constraining the unfolding process to unfold into energies below the maximum energy. By use of a carefully selected starting spectrum in which the spectra has a downward sweeping lethargy flux, a more realistic spectrum can be obtained. This is based on *a priori* information and is not imposing artificial information on the problem.

CHAPTER 6

EXPERIMENTAL RESULTS

Both the active LiI(Eu) detector and passive gold foil detector were analyzed. The gold foil data Y-direction irradiation are shown in all figures in this chapter and the remainder of the Z and YZ data are provided in Appendix C. The recorded gold foil activation rate obtained from the HPGe 411-keV counts can be seen in Figure 49. These activities were corrected for beam fluctuations. If the beam was off for more than 5 minutes, the data point was discarded and repeated. The beam off correction was made by simply removing the time in which there was no beam from the irradiation time. This same approach was used for the LiI(Eu) measurements. If the beam intensity switched during a run, the production rate was normalized to the higher number and the summation of the production and decay periods was used.

Production Rate in Gold Foil for Y-Direction

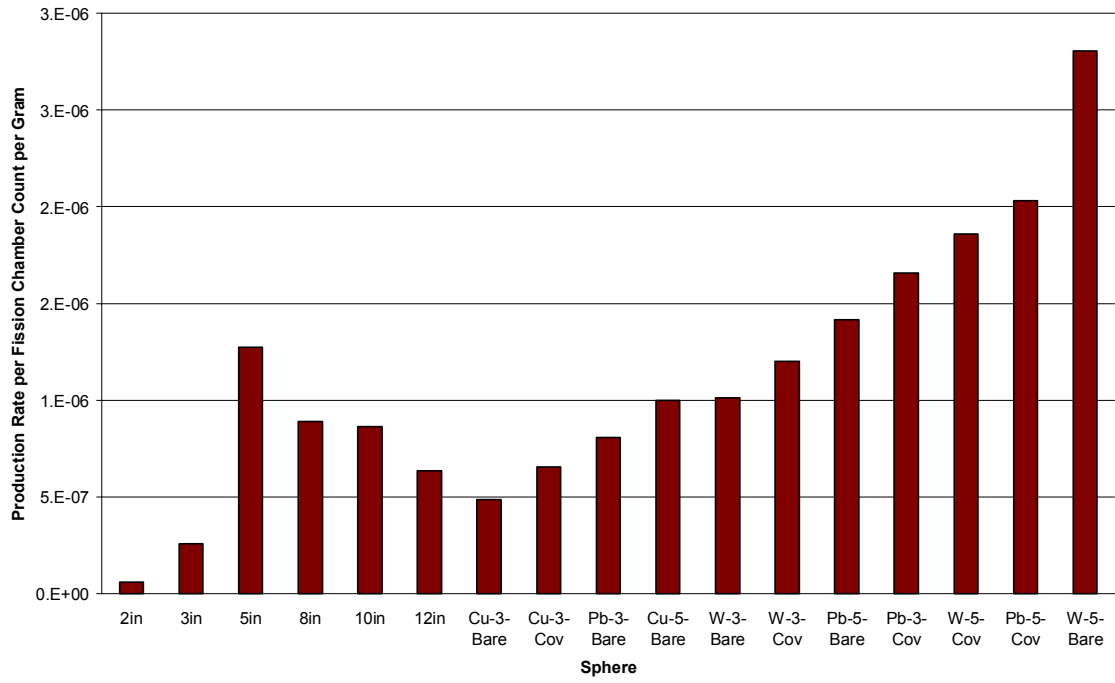


Figure 49. ^{198}Au production rate for the different spheres in the Y-direction irradiation configuration.

Table 6. The measured mass and ^{198}Au production rate of the gold foils for the unfiltered beam.

LANSCCE Run Number	Foil Numbers	Combined Mass	Ball	Production Rate / Fission Chamber Count
381	9B,9C	0.2527	2 inch	1.47456E-08
381	7A,7C	0.2541	3 inch	6.52703E-08
381	EB1, EB2	0.2158	5 inch	2.74531E-07
381	7E,7F	0.2553	8 inch	2.27059E-07
377	9G,9H	0.256	10 inch	2.20714E-07
377	9I,9J	0.2557	12 inch	1.62534E-07
377	4I,9A	0.2537	Small Cu Bare	1.23581E-07
377	3J,3H	0.2572	Small Cu Covered	1.68503E-07
381	9D,9E	0.2548	Small Pb Bare	2.05152E-07
377	2H,2J	0.2569	Large Cu Bare	2.56723E-07
377	4A,4B	0.2561	Small W Bare	2.58682E-07
377	4C,4D	0.2536	Small W Covered	3.04705E-07
379	12I,12G	0.2541	Large Pb Bare	3.5946E-07
379	12E,12D	0.2537	Small Pb Covered	4.19916E-07
377	4G,4H	0.2559	Large W Covered	4.75685E-07
379	2A,12F	0.2526	Large Pb Covered	5.12644E-07
377	4E,EF	0.2559	Large W Bare	7.18142E-07
377	2B,2C	0.2558	Large Cu Covered	4.57678E-08

These ^{198}Au production rates were unfolded using the MAXED_FC33 computer code. The unfolded neutron spectra was found to be in good agreement with the experimental TOF data. To validate the shape of the unfolded spectra, two conservative starting spectra were selected for comparison. The first conservative spectra is the flat starting spectra which seeds the unfolding process with equal fluence in each group from 1e-9 MeV to 800 MeV. The second conservative spectra that was selected was the unit

lethargy spectra. This spectra starts with a unit lethargy fluence in each group in the lethargy of energy. A best approximation was produced by using the TOF data above 50 MeV with the spectral data obtained in MCNPX for the calculated results and normalizing it to one source neutron. The comparison between these two conservative spectra and the best approximation spectra can be seen in Figure 50.

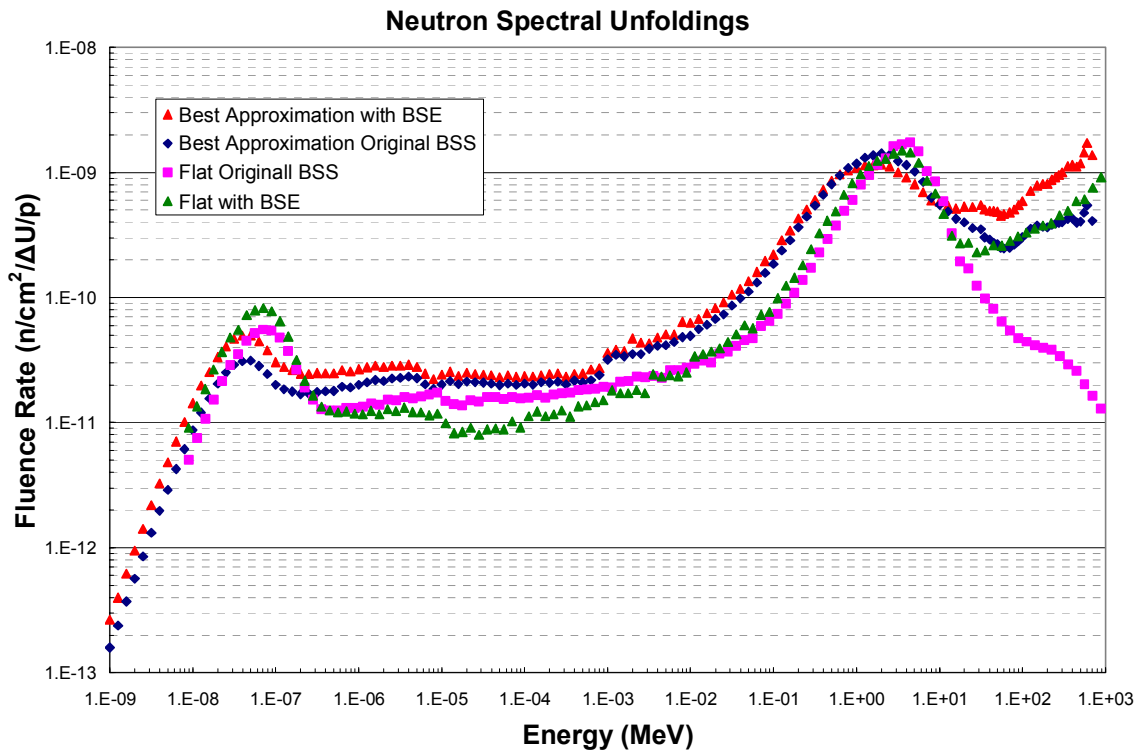


Figure 50. A comparison between the spectral unfoldings with the the flat and lethargy starting spectra and the best approximation spectrum.

To obtain the best approximation spectrum, the unfolding code was forced to unfold into energy bins that more closely resembled the TOF data. The spectra was also constrained to unfold into energies below 800 MeV, the maximum energy available at WNR. Only one outlier data point (sphere response) was discarded, which was the bare 5 inch sphere. A comparison between the calculated spectra, measured TOF data, and the

unfolded spectra can be seen in Figure 51. In Figure 51, a cell tally in the simplified model, a cell tally in the detailed model, the TOF data, and the unfolded neutron spectra are all compared. Reasonable agreement can be seen in Figure 51. Shown in Figure 55 is a comparison between the unfolded neutron spectrum with the entire BSE system verses the unfolded spectra of only the original BSS. Energy binned responses can be seen in Table 7. Shown in Table 9 is the ratio of the TOF system neutron spectrum to the unfolded neutron spectrum. Averaging the ratio of the count rates above 50 MeV, it has been found that the system has a scaling factor of 1. Shown following the tables is the poly filtered beam at WNR. 32.4 cm of polyethylene was inserted into the beam near the shutter. The poly is intended to knock out the neutrons below 10 MeV. The unfolding process is dominated by the high energy response and continues to tail up over predicting above 500 MeV. Shown also are only the BSE system and the only the original BSS system. Without using the a priori information, the original BSS system (using the flat starting spectrum) grossly under predicts the neutron spectrum. In the case for the pure poly example, it cannot predict the higher energy responses at all.

Neutron Energy Distribution from LANSCE

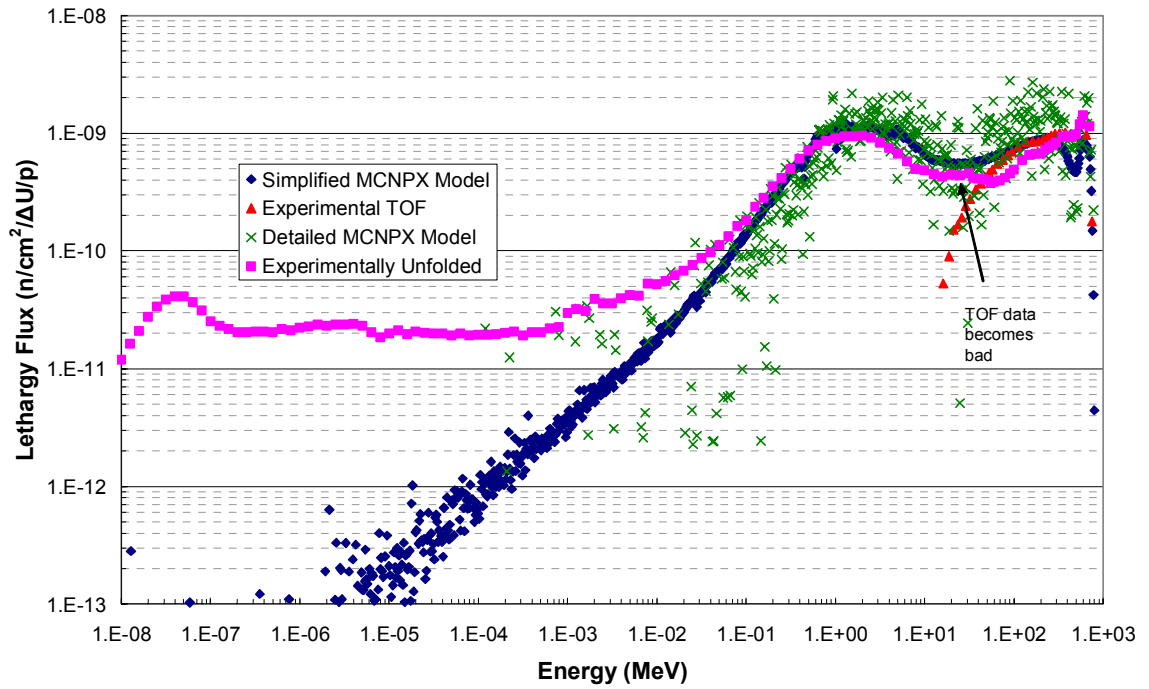


Figure 51. A comparison of the calculated and measured neutron fluxes as well as the unfolded neutron flux.

Neutron Energy Distribution from LANSCE

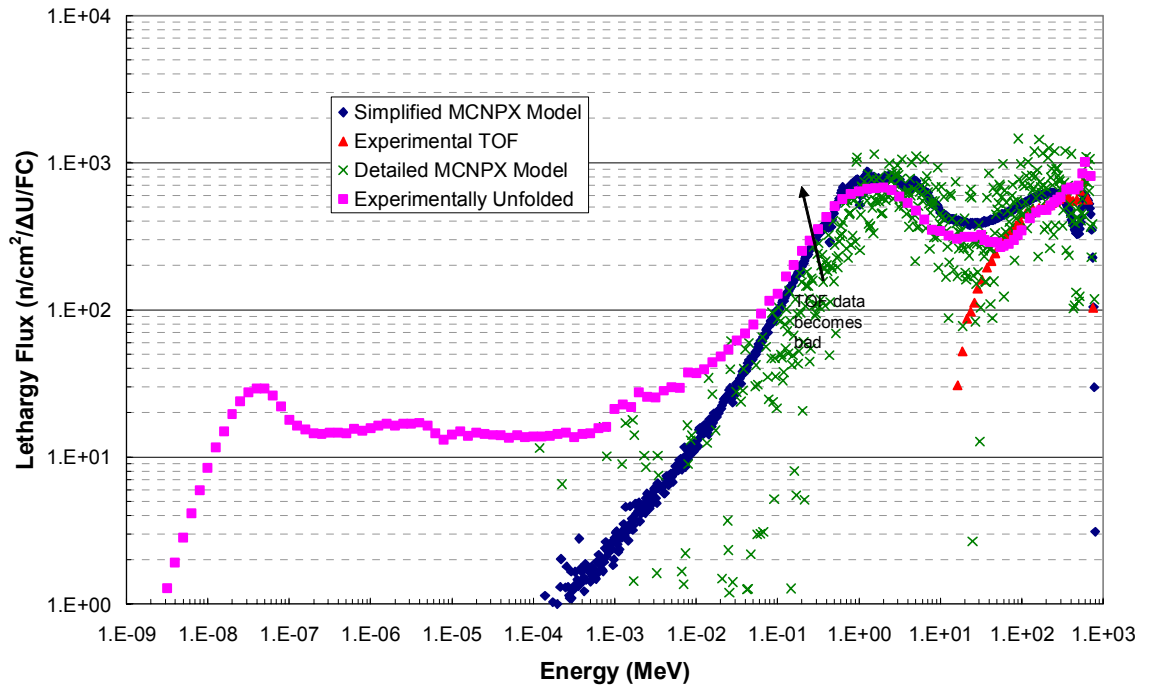


Figure 52. A comparison of the calculated and measured neutron fluxes as well as the unfolded neutron flux with respect to fission counts.

Neutron Energy Distribution from LANSCE

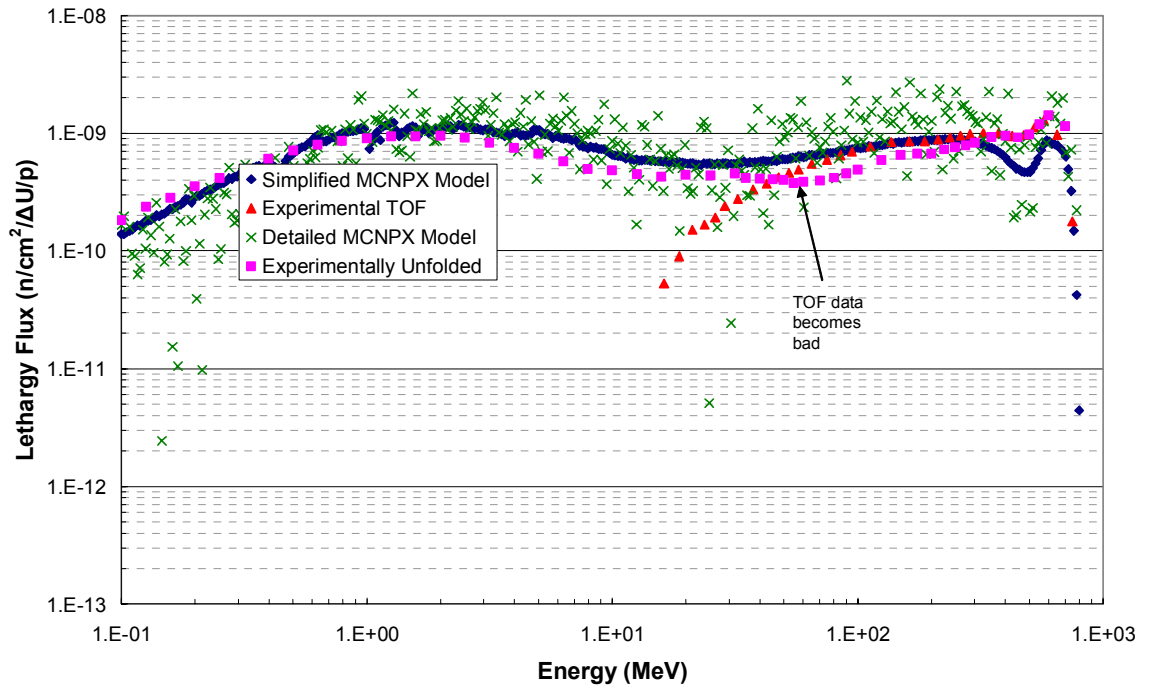


Figure 53. A comparison of the calculated and measured neutron fluxes as well as the unfolded neutron flux shown blown up from Figure 51.

Neutron Energy Distribution from LANSCE

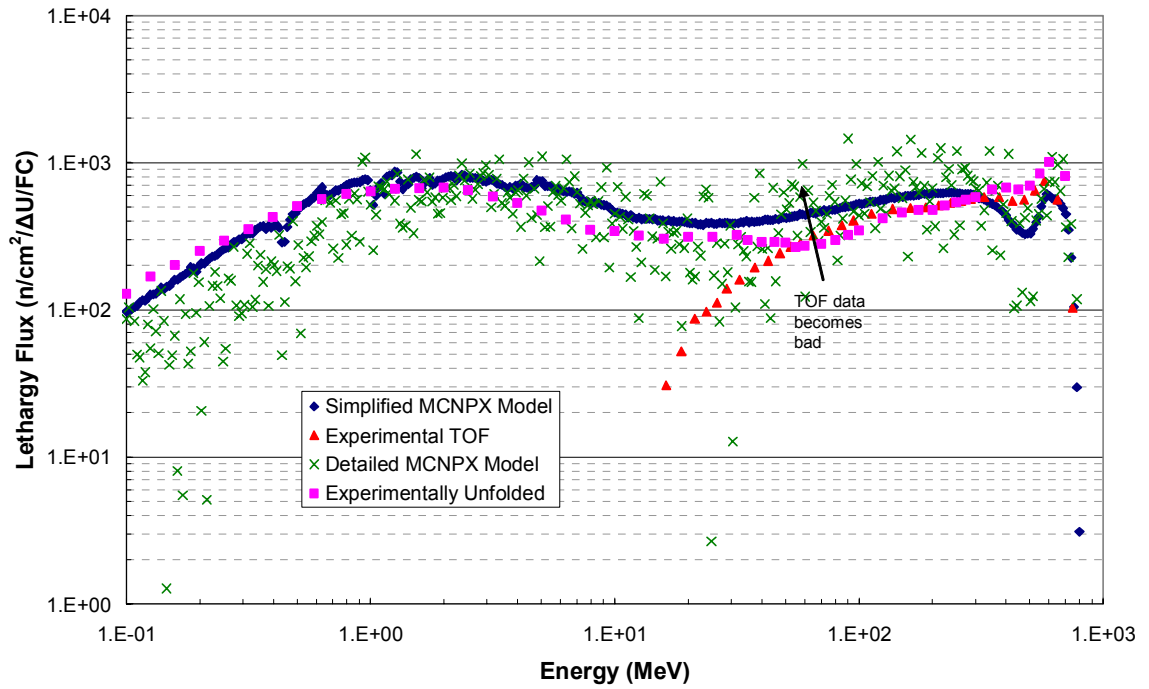


Figure 54.. A comparison of the calculated and measured neutron fluxes as well as the unfolded neutron flux shown blown up from Figure 51 with respect to the number of fission counts.

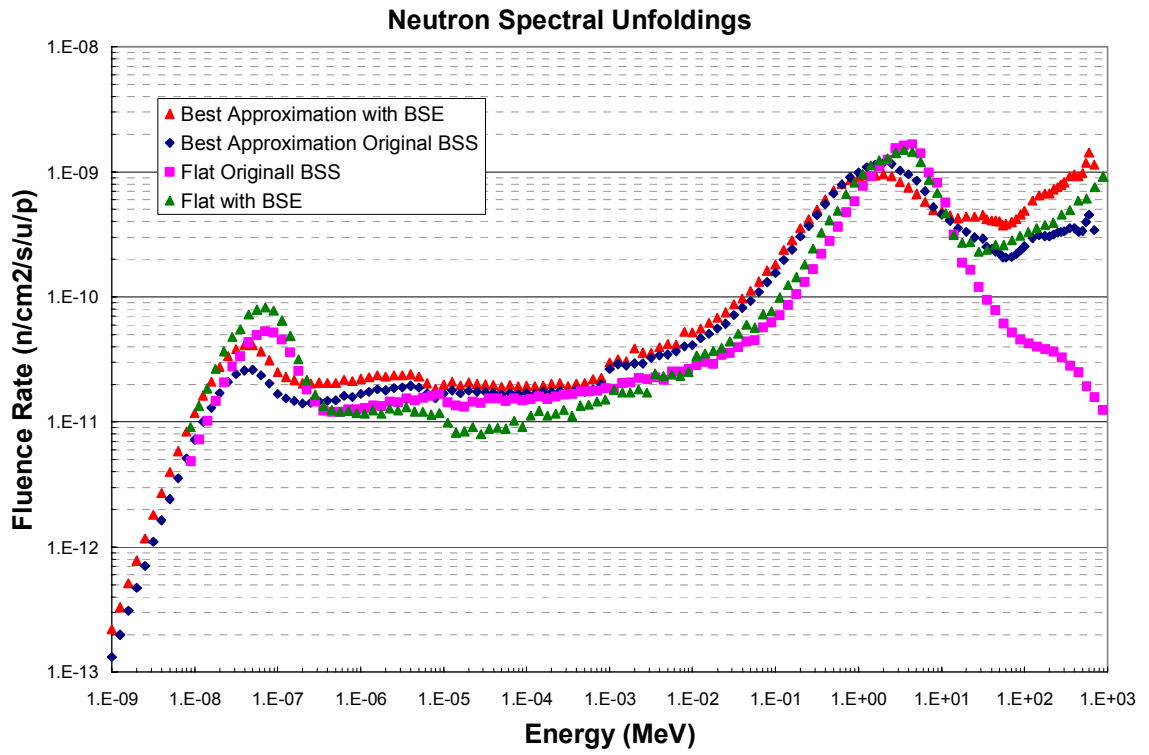


Figure 55. A comparison between spectral unfolding of only the original BSS and the new system with the BSE contributions compared.

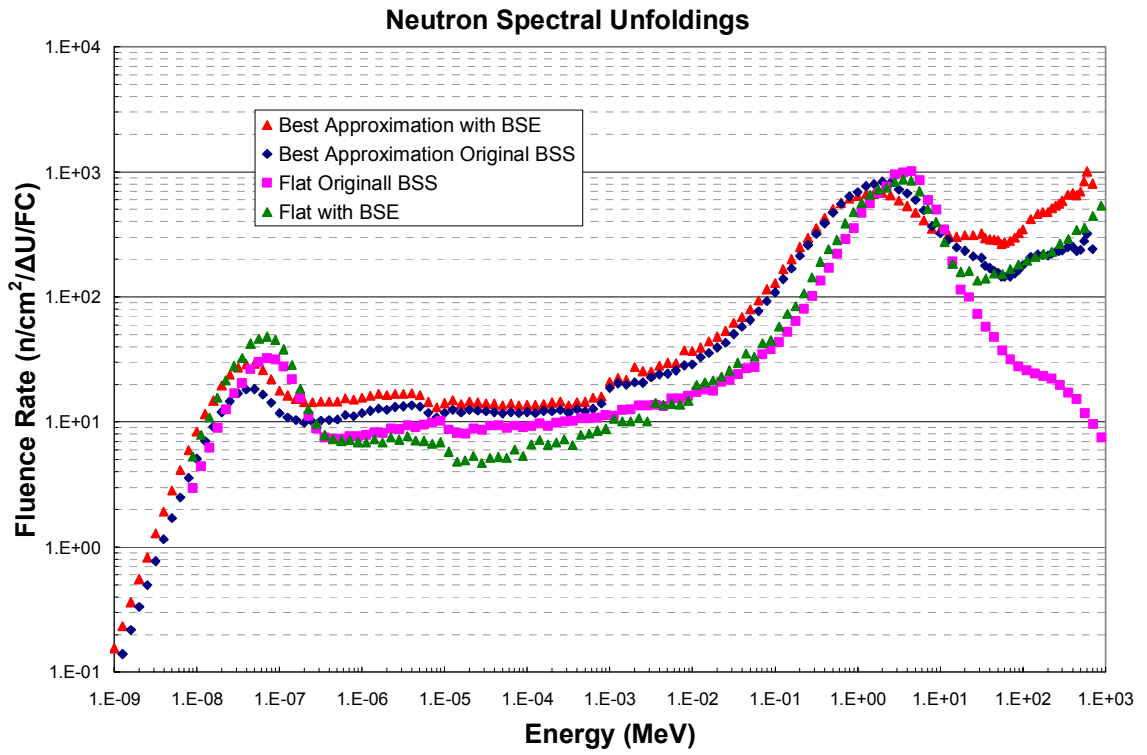


Figure 56. A comparison between spectral unfolding of only the original BSS and the new system with the BSE contributions compared shown with respect to fission counts.

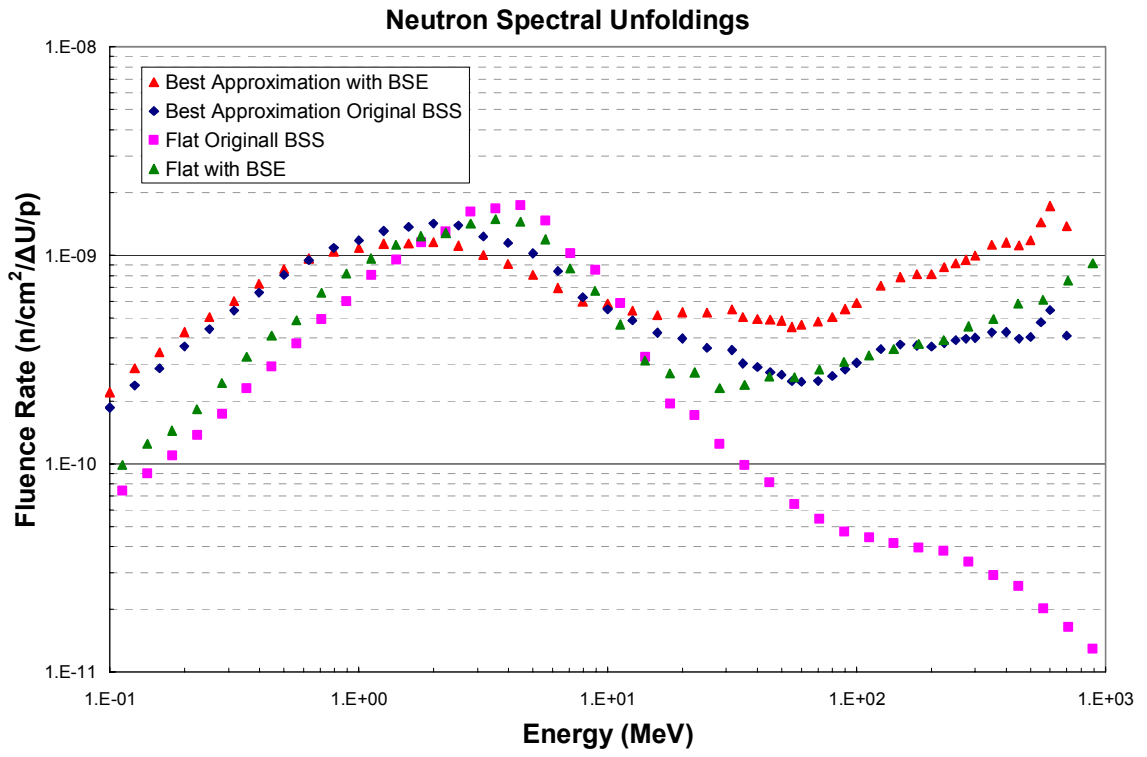


Figure 57. A blown up version of Figure 55 zoomed in on the energies above 100 keV.

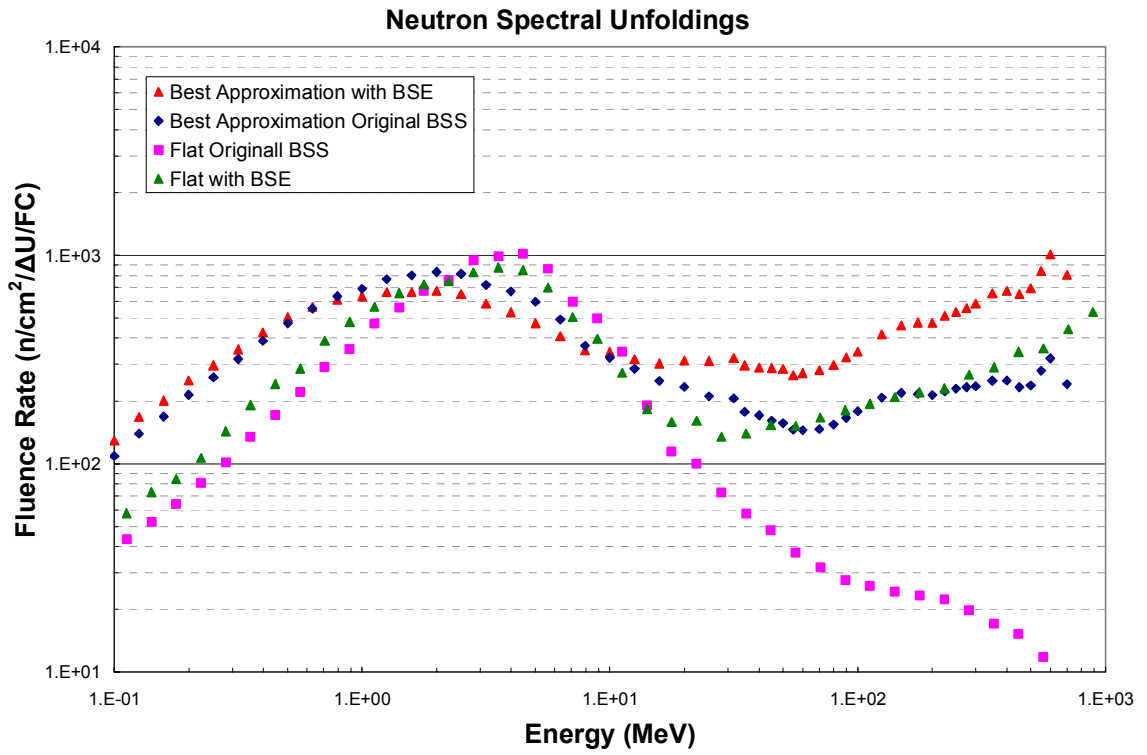


Figure 58. A blown up version of Figure 55 zoomed in on the energies above 100 keV plotted with respect to the number of fission counts.

Table 7. The neutron fluence rates per fission count for the MCNPX model, the unfolded neutron spectrum, and the TOF spectrum.

Upper Energy Bin (MeV)	Simplified Cell Tally MCNPX (n/cm ² /ΔU/FC)	Detailed Cell Tally MCNPX (n/cm ² /ΔU/FC)	Unfolded Neutron Spectrum (n/cm ² /ΔU/FC)	Unfolded Neutron Spectrum Only BSS (n/cm ² /ΔU/FC)	Time of Flight (n/cm ² /ΔU/FC)
1.00E-08	1.00E+00	3.00E+00	2.66E+01	1.61E+01	---
1.00E-07	0.00E+00	0.00E+00	2.21E+02	1.39E+02	---
1.00E-06	5.25E-01	0.00E+00	1.50E+02	1.07E+02	---
1.00E-05	1.64E+00	0.00E+00	1.58E+02	1.26E+02	---
1.00E-04	6.90E+00	0.00E+00	1.41E+02	1.21E+02	---
1.00E-03	2.92E+01	0.00E+00	1.52E+02	1.31E+02	---
1.00E-02	1.27E+02	4.48E+01	2.85E+02	2.36E+02	---
1.00E-01	5.60E+02	1.55E+02	7.34E+02	6.03E+02	---
1.00E+00	3.26E+04	1.91E+04	4.01E+03	3.84E+03	---
2.00E+01	1.17E+04	1.00E+04	9.32E+02	7.69E+02	---
3.00E+01	6.17E+03	4.36E+03	3.12E+02	2.11E+02	4.90E+02
4.00E+01	4.33E+03	3.19E+03	9.07E+02	5.54E+02	3.98E+02
5.00E+01	3.70E+03	2.95E+03	5.73E+02	3.18E+02	5.17E+02
6.00E+01	3.03E+03	4.30E+03	5.38E+02	2.91E+02	6.22E+02
7.00E+01	2.71E+03	2.41E+03	2.81E+02	1.46E+02	6.79E+02
8.00E+01	2.83E+03	3.04E+03	2.97E+02	1.54E+02	3.88E+02
9.00E+01	1.97E+03	1.51E+03	3.23E+02	1.66E+02	4.24E+02
1.00E+02	2.04E+03	3.67E+03	2.94E+03	1.60E+03	4.56E+02
2.00E+02	1.55E+04	1.87E+04	1.35E+03	6.43E+02	2.16E+03
3.00E+02	9.88E+03	1.21E+04	2.19E+03	9.20E+02	2.44E+03
4.00E+02	5.86E+03	6.44E+03	1.33E+03	5.01E+02	1.31E+03
5.00E+02	3.29E+03	3.64E+03	1.35E+03	4.70E+02	1.25E+03
6.00E+02	3.18E+03	2.75E+03	1.85E+03	5.99E+02	1.57E+03
7.00E+02	3.29E+03	5.24E+03	8.07E+02	2.41E+02	6.34E+02
8.00E+02	1.16E+03	1.09E+03	9.23E+01	2.71E-04	1.16E+02

Table 8. The neutron fluence rates per proton for the MCNPX model, the unfolded neutron spectrum, and the TOF spectrum.

Upper Energy Bin (MeV)	Simplified Cell Tally MCNPX (n/cm ² /ΔU/p)	Detailed Cell Tally MCNPX (n/cm ² /ΔU/p)	Unfolded Neutron Spectrum (n/cm ² /ΔU/p)	Unfolded Neutron Spectrum Only BSS (n/cm ² /ΔU/p)	Time of Flight (n/cm ² /ΔU/p)
1.00E-08	0.00E+00	2.00E+00	4.55E-11	2.74E-11	---
1.00E-07	0.00E+00	0.00E+00	3.78E-10	2.37E-10	---
1.00E-06	4.11E-13	0.00E+00	2.57E-10	1.82E-10	---
1.00E-05	1.28E-12	0.00E+00	2.70E-10	2.14E-10	---
1.00E-04	5.39E-12	0.00E+00	2.40E-10	2.06E-10	---
1.00E-03	2.28E-11	0.00E+00	2.59E-10	2.24E-10	---
1.00E-02	9.94E-11	2.14E-15	4.86E-10	4.02E-10	---
1.00E-01	4.38E-10	7.39E-15	1.25E-09	1.03E-09	---
1.00E+00	2.55E-08	9.11E-13	6.85E-09	6.56E-09	---
1.00E+01	4.95E-08	2.65E-12	9.14E-09	1.09E-08	---
2.00E+01	9.12E-09	4.78E-13	1.59E-09	1.31E-09	---
3.00E+01	4.82E-09	2.08E-13	5.32E-10	3.59E-10	8.36E-10
4.00E+01	3.39E-09	1.52E-13	1.55E-09	9.45E-10	6.79E-10
5.00E+01	2.89E-09	1.41E-13	9.78E-10	5.42E-10	8.82E-10
6.00E+01	2.37E-09	2.05E-13	9.18E-10	4.96E-10	1.06E-09
7.00E+01	2.12E-09	1.15E-13	4.80E-10	2.50E-10	1.16E-09
8.00E+01	2.21E-09	1.45E-13	5.06E-10	2.63E-10	6.63E-10
9.00E+01	1.54E-09	7.18E-14	5.52E-10	2.83E-10	7.23E-10
1.00E+02	1.59E-09	1.75E-13	5.02E-09	2.73E-09	7.79E-10
2.00E+02	1.22E-08	8.80E-13	2.31E-09	1.10E-09	3.69E-09
3.00E+02	7.84E-09	5.68E-13	3.74E-09	1.57E-09	4.16E-09
4.00E+02	4.64E-09	3.03E-13	2.27E-09	8.55E-10	2.24E-09
5.00E+02	2.61E-09	1.71E-13	2.30E-09	8.02E-10	2.13E-09
6.00E+02	2.52E-09	1.29E-13	3.16E-09	1.02E-09	2.69E-09
7.00E+02	2.61E-09	2.46E-13	1.38E-09	4.11E-10	1.08E-09
8.00E+02	9.17E-10	5.14E-14	1.58E-10	4.62E-16	1.99E-10

Table 9. Shown is the ratio of the TOF neutron fluence rate in each bin to the fluence rate of the unfolded spectra.

Energy	Time of Flight (n/cm ² /ΔU/FC)	Unfolded Neutron Spectrum (n/cm ² /ΔU/FC)	Ratio of TOF Fluence Rate to Unfolded Fluence Rate	Unfolded Neutron Spectrum Only BSS (n/cm ² /ΔU/FC)	Ratio of TOF Fluence Rate to Unfolded Fluence Rate
1.00E-08	---	2.66E+01		1.61E+01	
1.00E-07	---	2.21E+02		1.39E+02	
1.00E-06	---	1.50E+02		1.07E+02	
1.00E-05	---	1.58E+02		1.26E+02	
1.00E-04	---	1.41E+02		1.21E+02	
1.00E-03	---	1.52E+02		1.31E+02	
1.00E-02	---	2.85E+02		2.36E+02	
1.00E-01	---	7.34E+02		6.03E+02	
1.00E+00	---	4.01E+03		3.84E+03	
1.00E+01	---	5.36E+03		6.39E+03	
2.00E+01	---	9.32E+02		7.69E+02	
3.00E+01	4.35E+02	3.12E+02		2.11E+02	
4.00E+01	3.53E+02	9.07E+02	2.57E+00	5.54E+02	1.57E+00
5.00E+01	4.59E+02	5.73E+02	1.25E+00	3.18E+02	6.92E-01
6.00E+01	5.52E+02	5.38E+02	9.76E-01	2.91E+02	5.27E-01
7.00E+01	6.03E+02	2.81E+02	4.66E-01	1.46E+02	2.43E-01
8.00E+01	3.45E+02	2.97E+02	8.61E-01	1.54E+02	4.48E-01
9.00E+01	3.76E+02	3.23E+02	8.60E-01	1.66E+02	4.42E-01
2.00E+02	1.92E+03	1.35E+03	7.05E-01	6.43E+02	3.35E-01
3.00E+02	2.16E+03	2.19E+03	1.01E+00	9.20E+02	4.26E-01
4.00E+02	1.17E+03	1.33E+03	1.14E+00	5.01E+02	4.30E-01
5.00E+02	1.11E+03	1.35E+03	1.21E+00	4.70E+02	4.24E-01
6.00E+02	1.40E+03	1.85E+03	1.32E+00	5.99E+02	4.29E-01
7.00E+02	5.62E+02	8.07E+02	1.44E+00	2.41E+02	4.29E-01
8.00E+02	1.03E+02	9.23E+01	8.93E-01	2.71E-04	2.62E-06

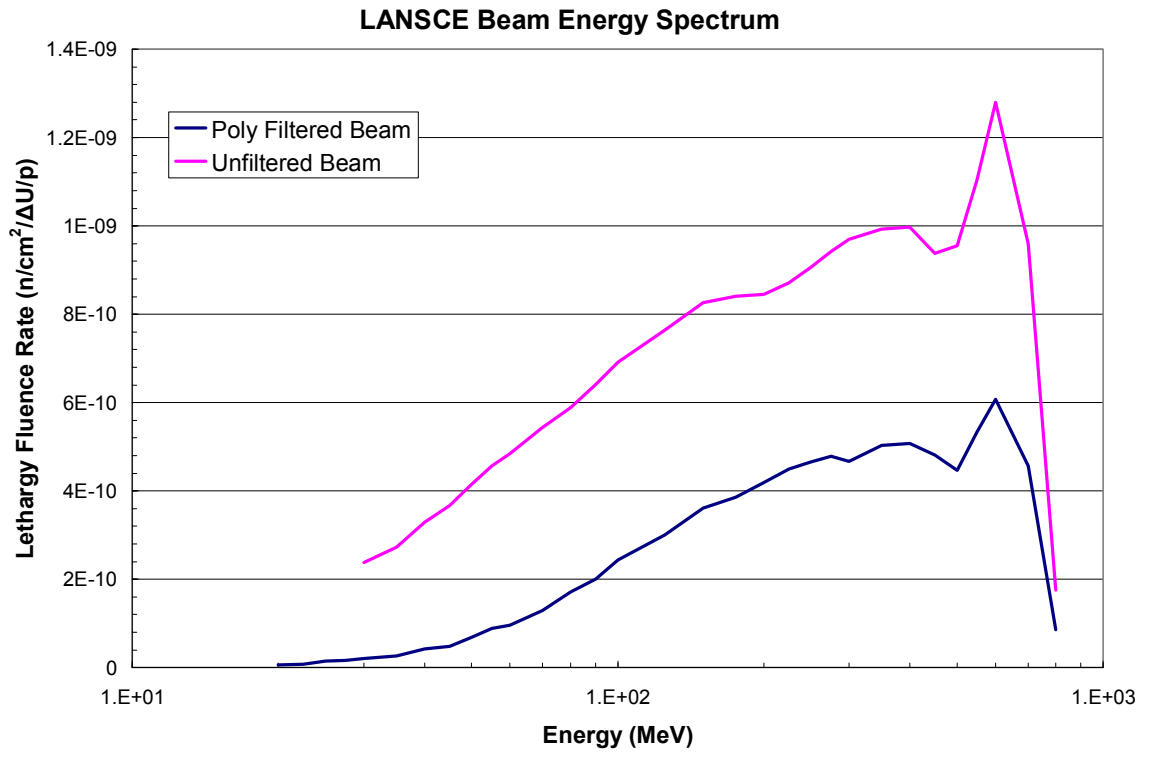


Figure 59. A comparison of the filtered and unfiltered neutron beams measured by the TOF system.

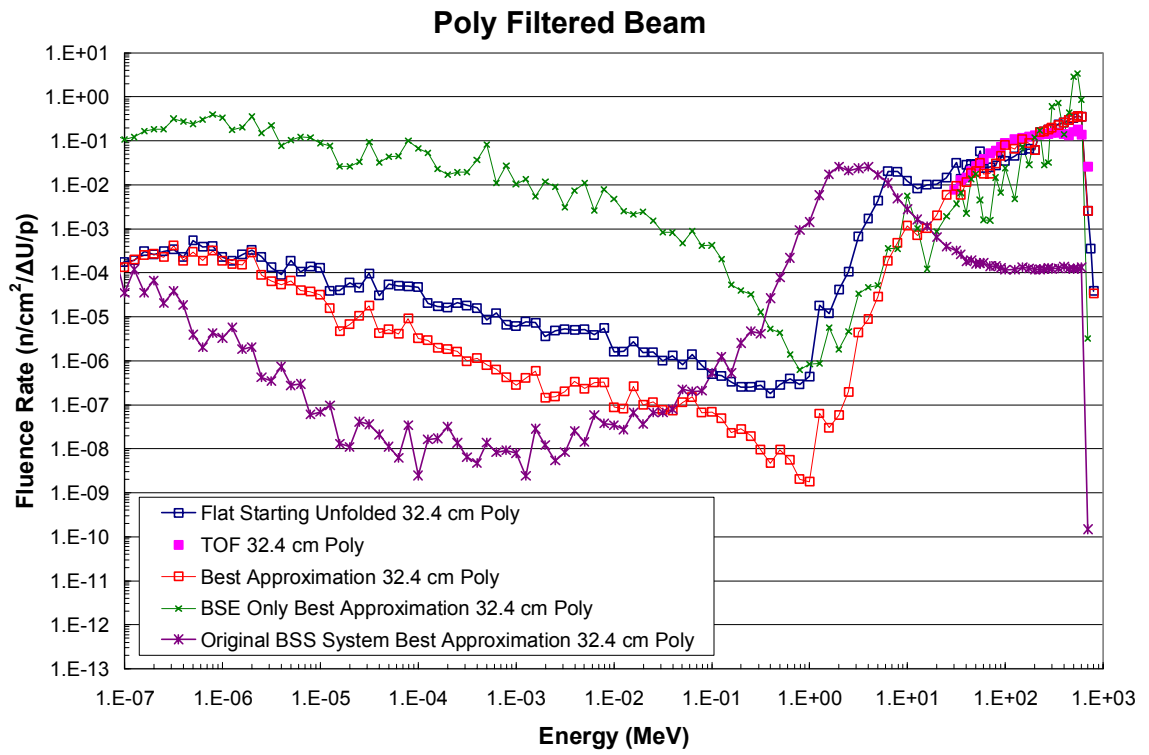


Figure 60. 32.4 cm of poly filtration in the WNR beam. Shown is the TOF, a flat starting spectrum and the best approximation unfoldings.

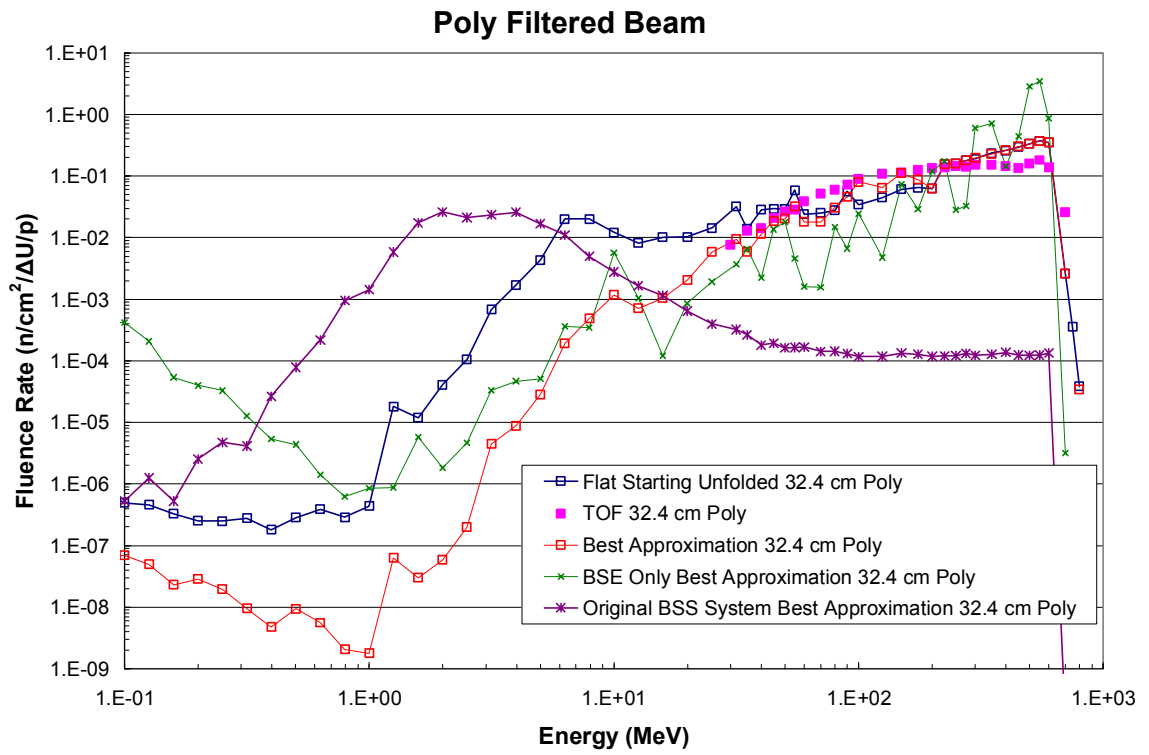


Figure 61. 32.4 cm of poly filtration in the WNR beam blown up above 100 keV. Shown is the TOF, a flat starting spectrum and the best approximation unfoldings.

CHAPTER 7

CONCLUSIONS

In our current work, the MCNPX^{xlvi} code was used to investigate design modifications to increase the high-energy neutron response of the standard Bonner spheres with cost as a consideration. The system selected uses the existing commercially available BSS as a basis and then extends it by adding concentric shells of copper, tungsten, and lead which are used in various combinations with the existing spheres. The design incorporates passive and active detection techniques, namely ¹⁹⁷Au activation foils and the standard Ludlum ⁶Li(Eu) scintillator. The modeled BSE was fabricated (with the exception of the smaller 3.25", 3.5", 3.75", 4" and 4.5" spheres) and tested. Measurements were performed with the BSE at LANSCE. The additional detector spheres provide a more accurate measure of the neutron spectra in the energy regions above 10-MeV than the BSS system alone. In places, the original BSS system under predicts by more than a factor of three thousand for the poly filtered beam. Vastly improved agreement was seen between the measured spectrum and the LANSCE spectrum. The BSE spectrum deviates by a maximum of a factor of 2 while holding no net deviation from the measured spectrum (the under-predictions are offset by the over-predictions). An overall robust detector system has been found to have a good sensitivity over 13 decades in energy, maintain a nearly isotropic angular response and be a versatile high and low flux detector.

CHAPTER 8

FUTURE WORK

Future work on this project should entail the fabrication of four additional spheres to further improve the energy structure of the system. Some preliminary work indicates that a 12" heavy water and 12" light water sphere set in addition to the 15" and 18" spheres. These spheres have the unique shapes that are not present with the other detectors. The most improvement to the detector system should come from the 12" heavy water sphere, as it provides the most unique data. This is seen in the following figure. This sphere does not have a discernable peak in the high energy region and has an even higher smooth energy continuum response through the low energy region because of the low absorption cross section of the deuterium. Preliminary MCNPX models of the responses show these added spheres that have no high energy upward swinging responses, so the unfolding program likely constrains the unfolded fluence in that energy range. Another suitable alternative is deuterated polyethylene. This should produce a similar response to the heavy water version.

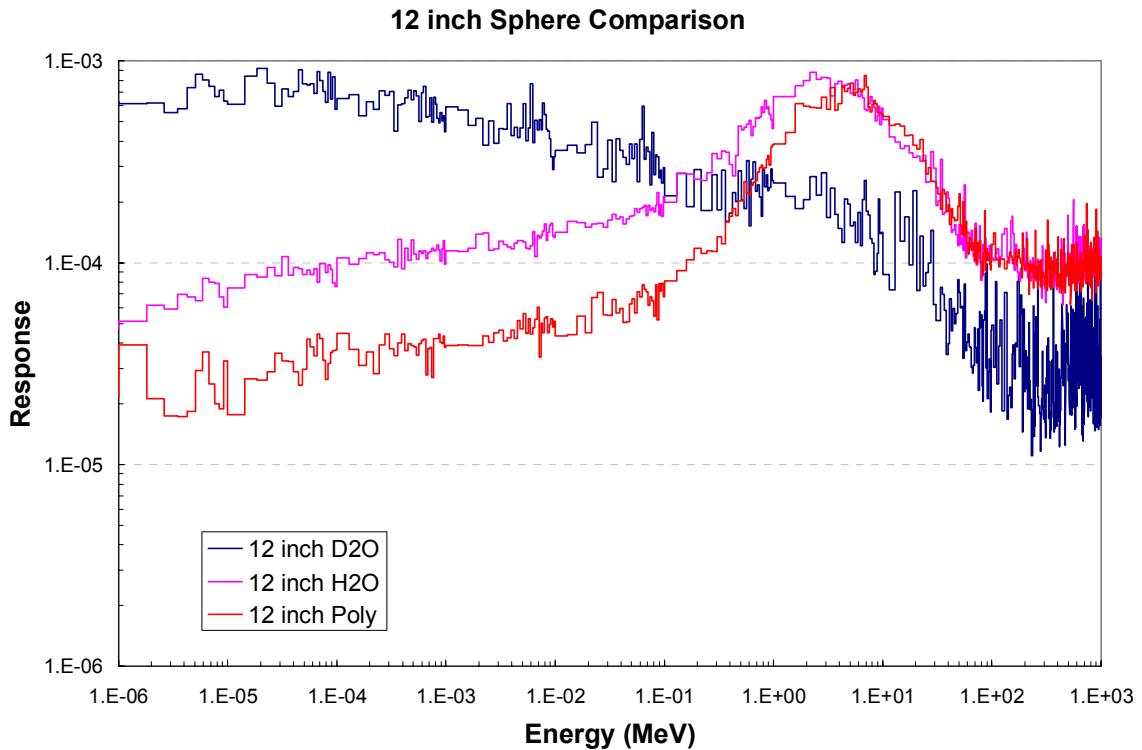


Figure 62. 12” sphere comparison for heavy water, light water and poly spheres. These spectra have the unique feature that they do not tail up at the high end of the spectra.

The second item that should further be investigated is the use of Bayesian Statistics^{liv} as a starting spectrum generator. With *a-priori* information, the starting spectrum can be guessed with much higher confidence. Since this *a-priori* information is developed from the irradiation conditions, no artificial guessing is introduced. This artificial information can come from computer models, MCNP simulations, or problem specifics. Once spectrum details such as peak shapes and positions are specified with flexibility of position, shape and magnitude, a Bayesian Statistics package can fit these spectral conditions with the detector responses producing a starting spectrum with more energy structure than is available from a flat starting spectra with no artificial assistance.

Third place to continue researching is the use of smaller spheres to produce unique energy structure in the 100 eV to 10 keV region. One possible way to do this is use smaller spheres. This solution is viable for the gold foil passive detector, but not for the active LiI(Eu) detector. The crystal housing is too large for a uniform response. Even in the foil method, the smaller spheres become very directional dependant which is a downfall of the system. Preliminary responses can be seen in Figure 63. This method investigated was using acrylic PMMA half spheres. These are a commercially available product for minimal cost. Not all of the spheres would be needed since they do not provide that much additional structure. The system does add structure in this region and should be investigated as a further supplement.

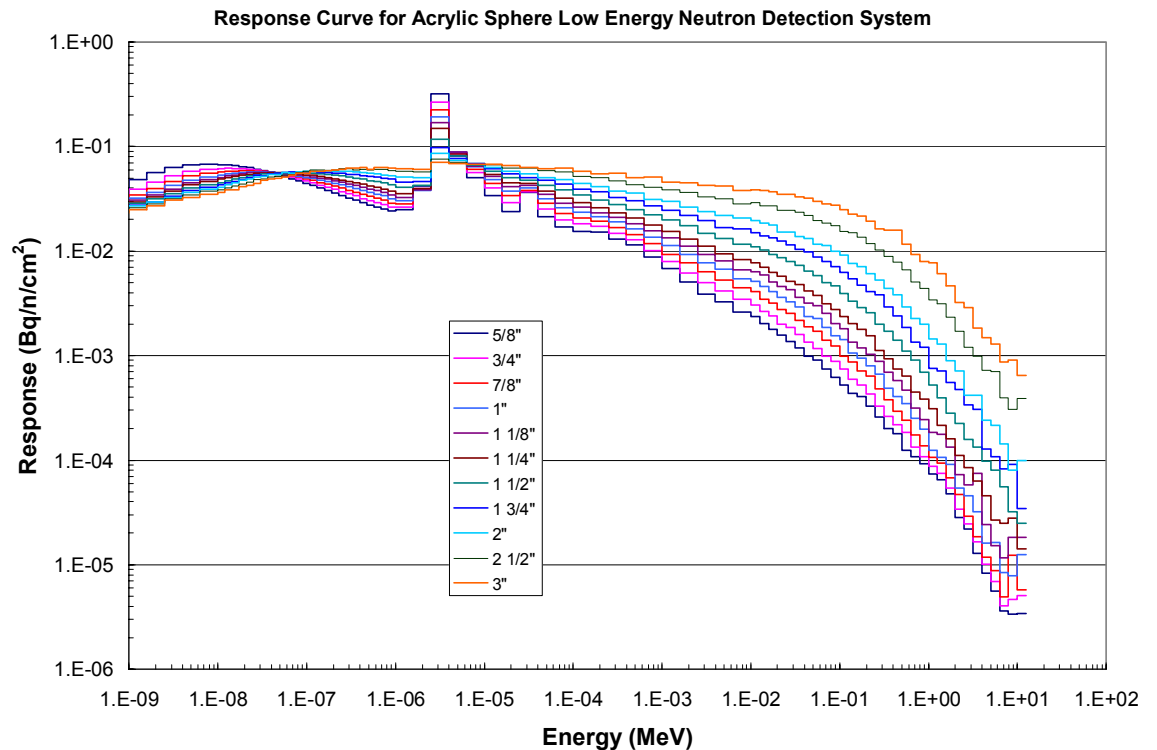


Figure 63. Preliminary responses for small acrylic moderating spheres covering gold foils.

APPENDIX A

GOLD FOIL RESPONSE DATA

Z-Directional Responses

In this appendix, the gold foil response data will be presented. As before, the plots are the production rate as a function of neutron energy. In Figure 64 through Figure 68, the response matrices are shown for the Z-direction.

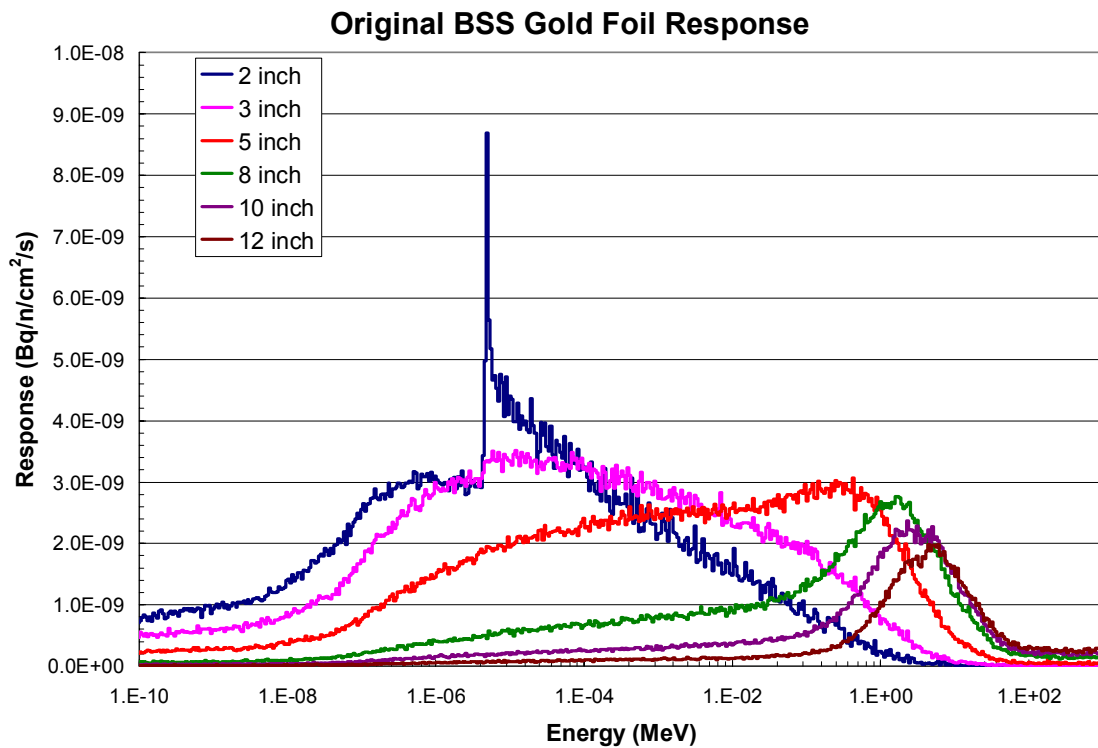


Figure 64. The response of the original BSS system is shown for the Z-direction neutron source.

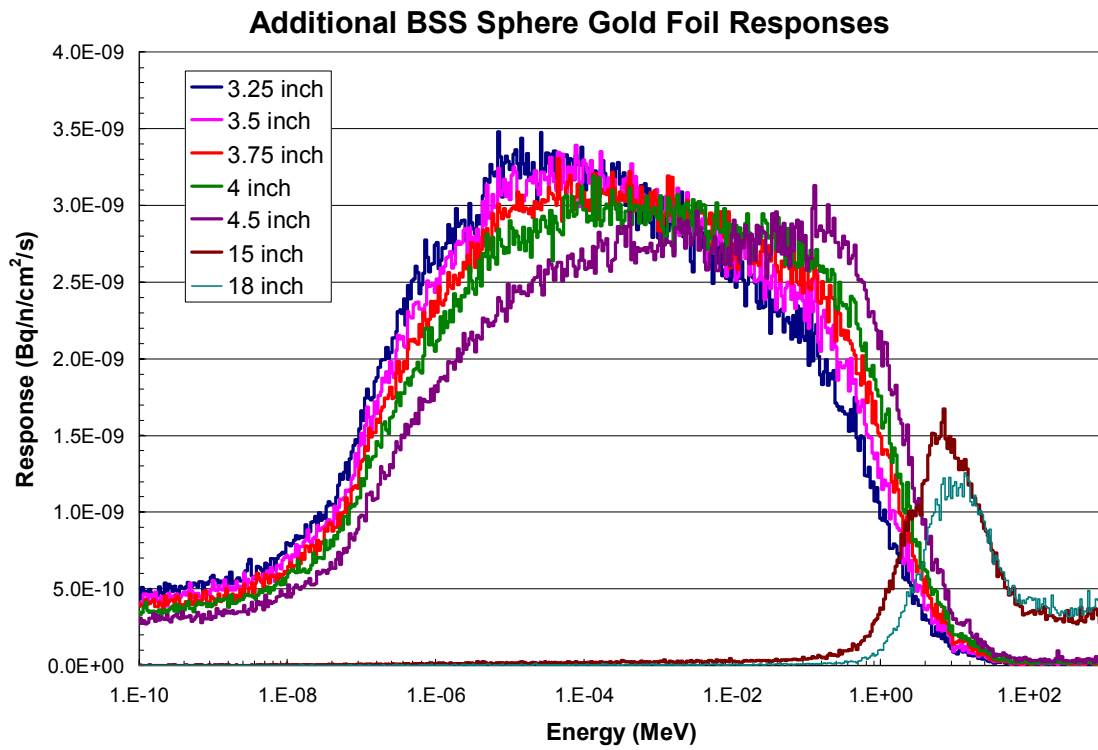


Figure 65. The response of the BSE polyethylene spheres and polyethylene holder is shown for the Z-direction neutron irradiation.

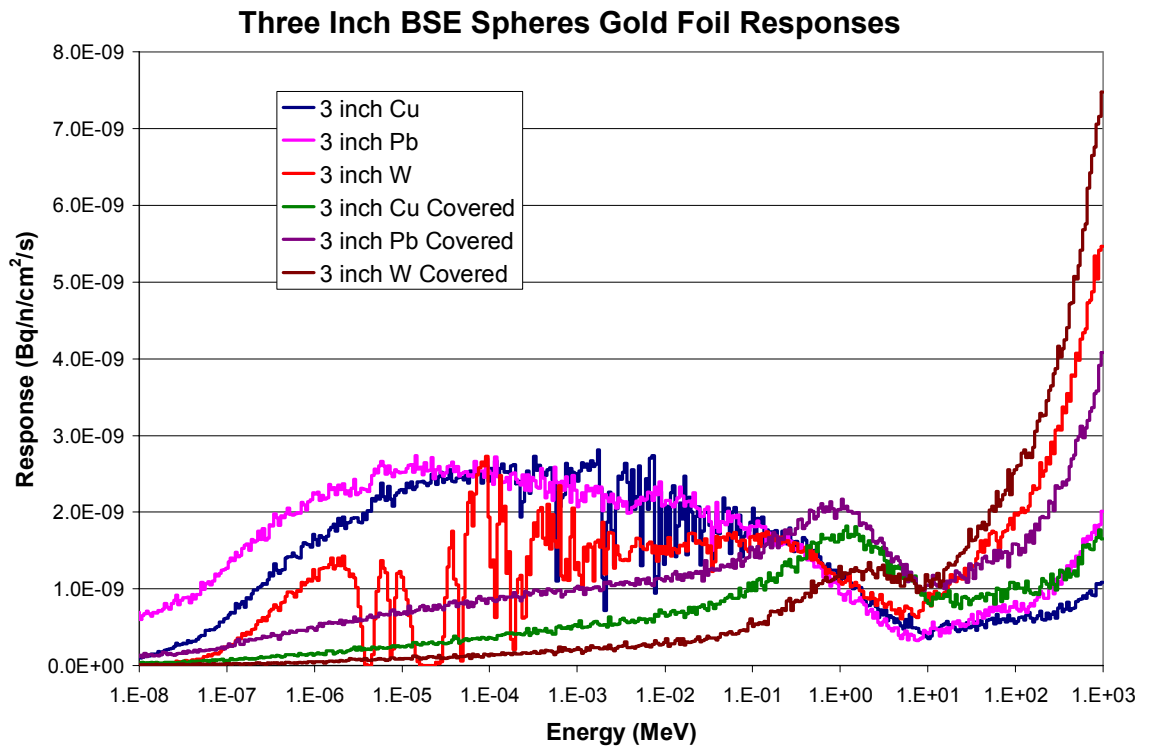


Figure 66. The small assembly (three inch inner sphere) BSE spheres gold foil detector response for the Z-direction neutron source.

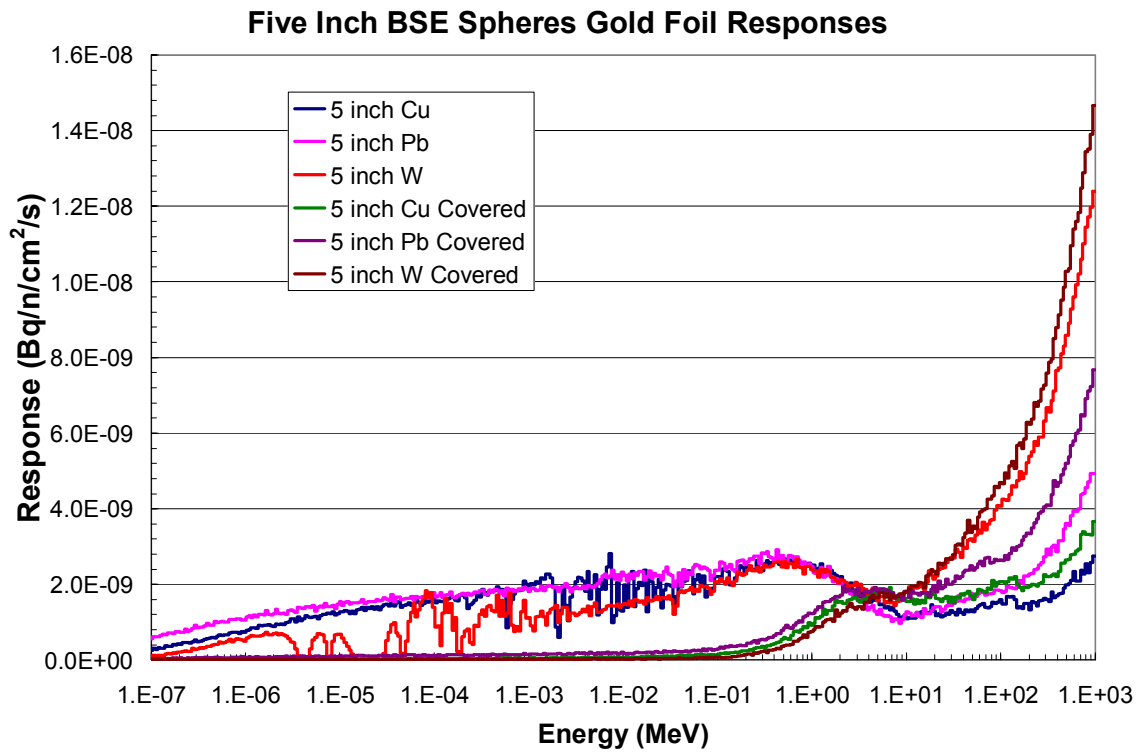


Figure 67. The large assembly (five inch inner sphere) BSE spheres gold foil detector response for the Z-direction neutron source.

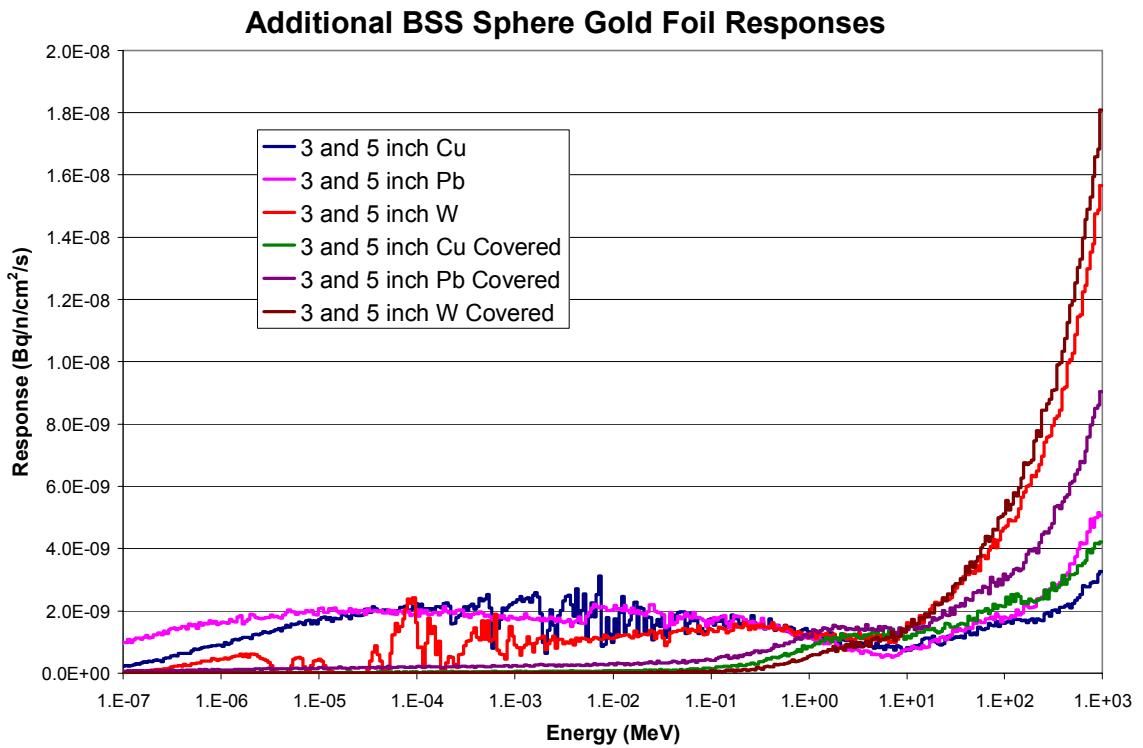


Figure 68. The BSE gold foil detector system is shown which utilizes both the 3” and 5” shells simultaneously for the Z-direction neutron source.

YZ-Directional Responses

In this portion of the appendix, the gold foil response data will be presented for the YZ-direction neutron field. As before, the plots are the production rate as a function of neutron energy. These responses are shown in Figure 69 through Figure 73.

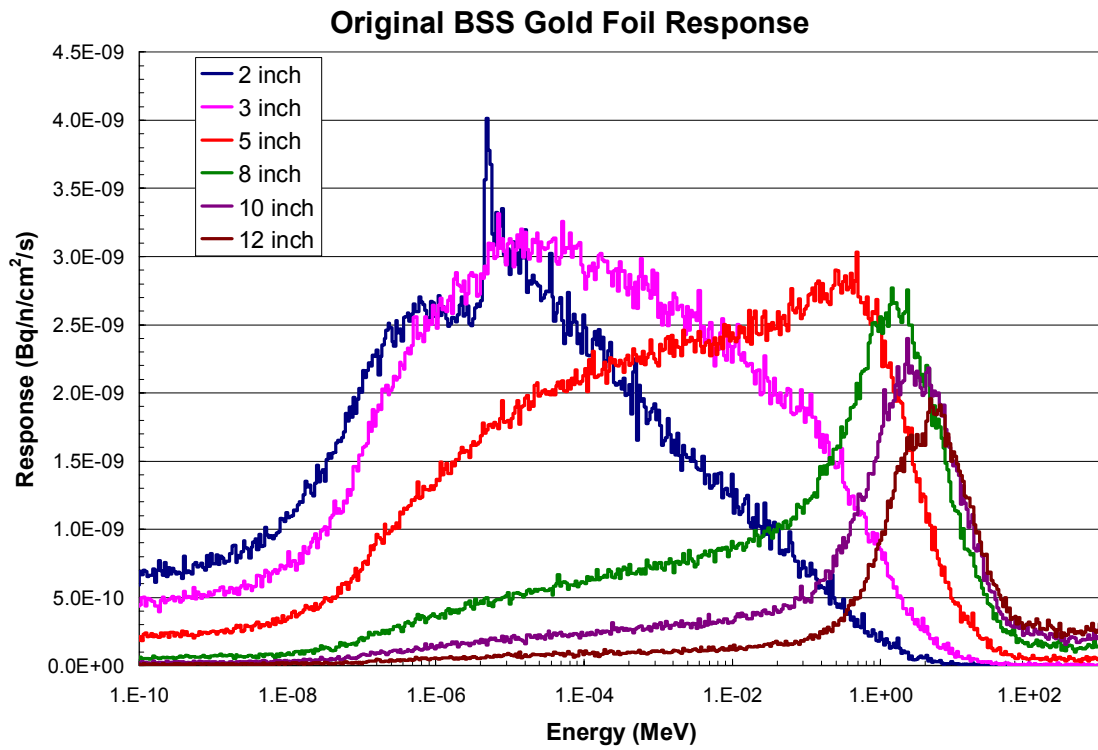


Figure 69. The response of the original BSS system is shown for the YZ-direction neutron source.

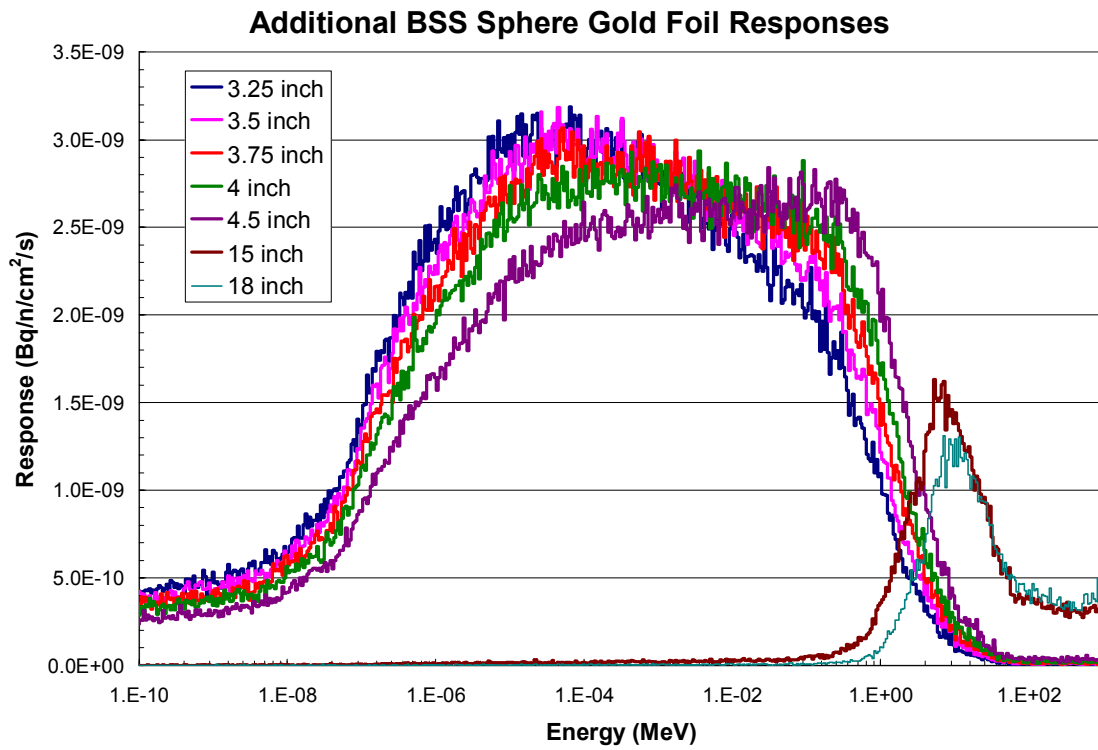


Figure 70. The response of the BSE polyethylene spheres and polyethylene holder is shown for the YZ-direction neutron irradiation.

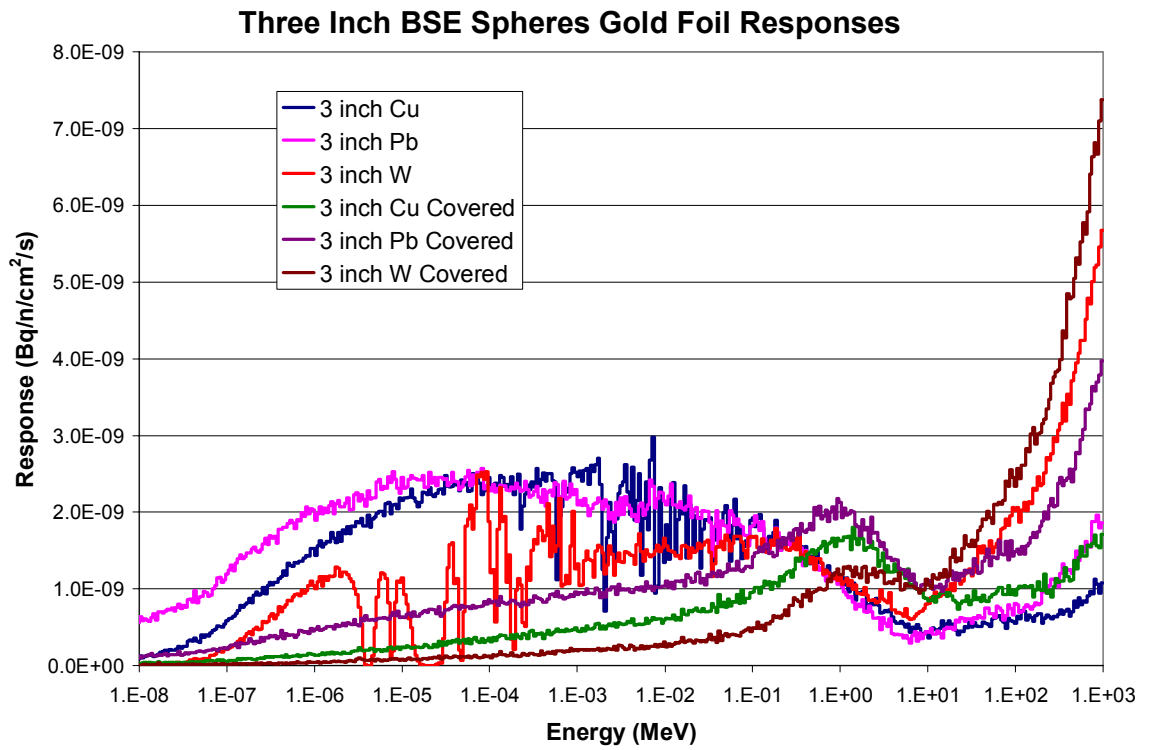


Figure 71. The small assembly (three inch inner sphere) BSE spheres gold foil detector response for the YZ-direction neutron source.

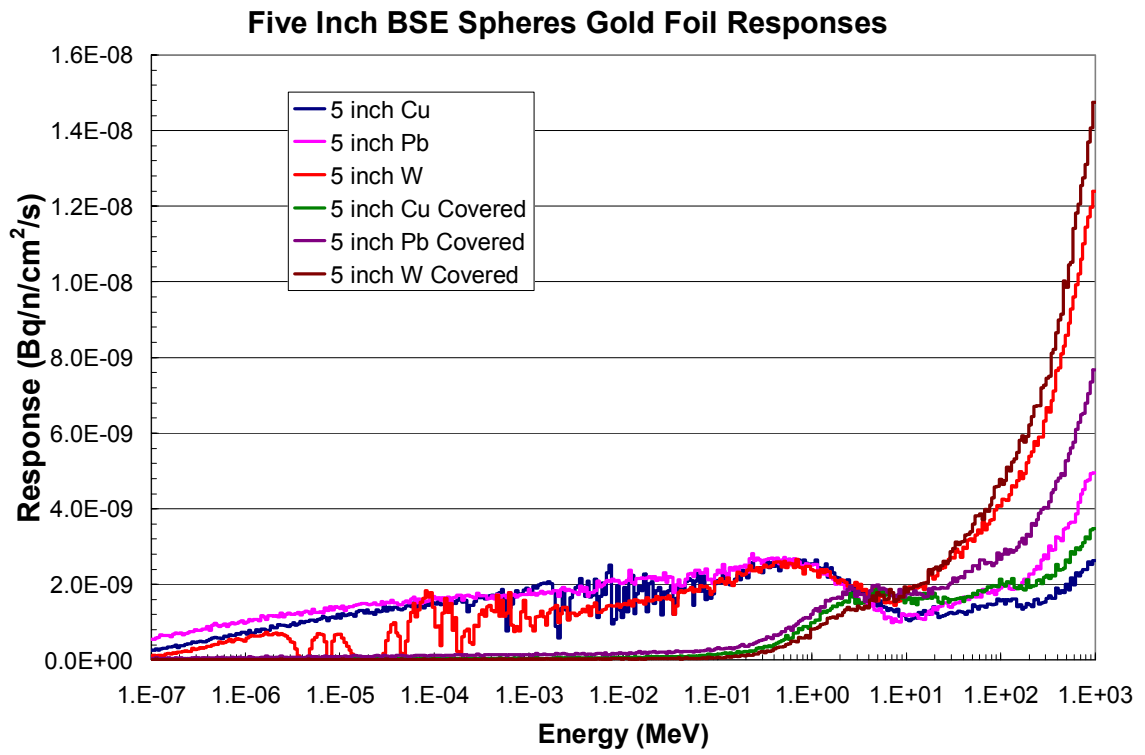


Figure 72. The large assembly (five inch inner sphere) BSE spheres gold foil detector response for the YZ-direction neutron source.

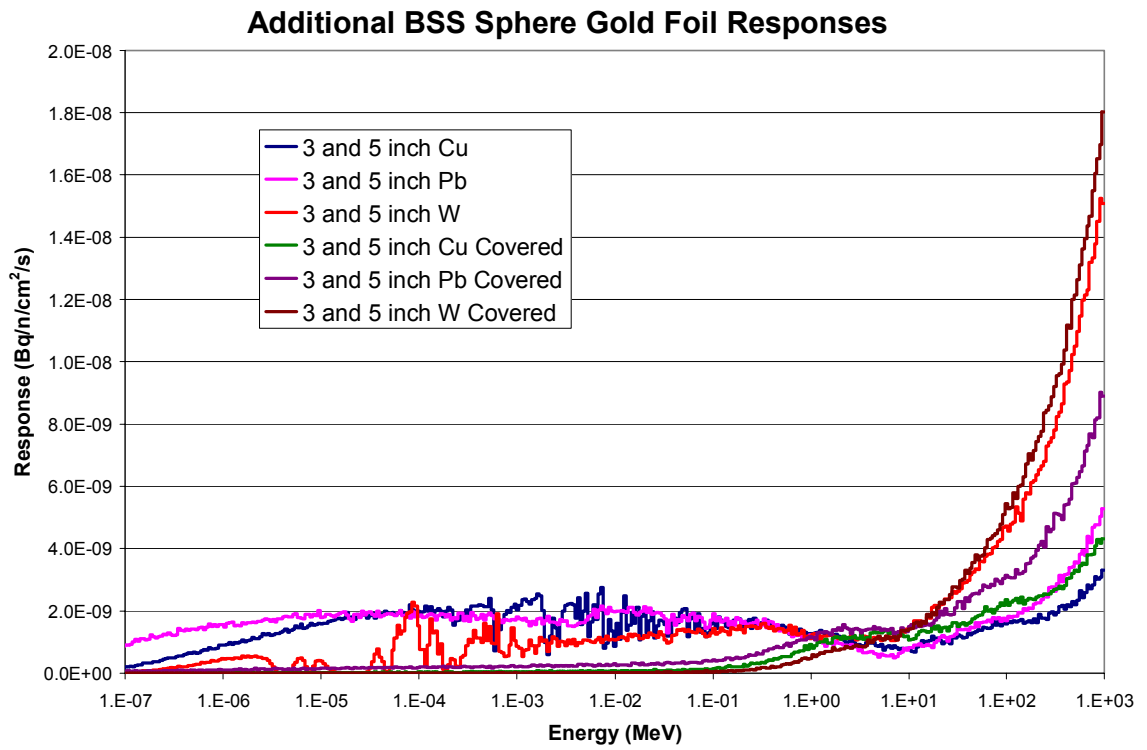


Figure 73. The BSE gold foil detector system is shown which utilizes both the 3” and 5” shells simultaneously for the Z-direction neutron source.

APPENDIX B

LiI(EU) DETECTOR RESPONSE DATA

Z-Directional Responses

In this appendix, the active LiI(Eu) detector data will be presented. As before, the plots are the reaction rate (n,α) per unit neutron fluence as a function of neutron energy.

In Figure 74 through Figure 78, the response matrices are shown for the Z-direction.

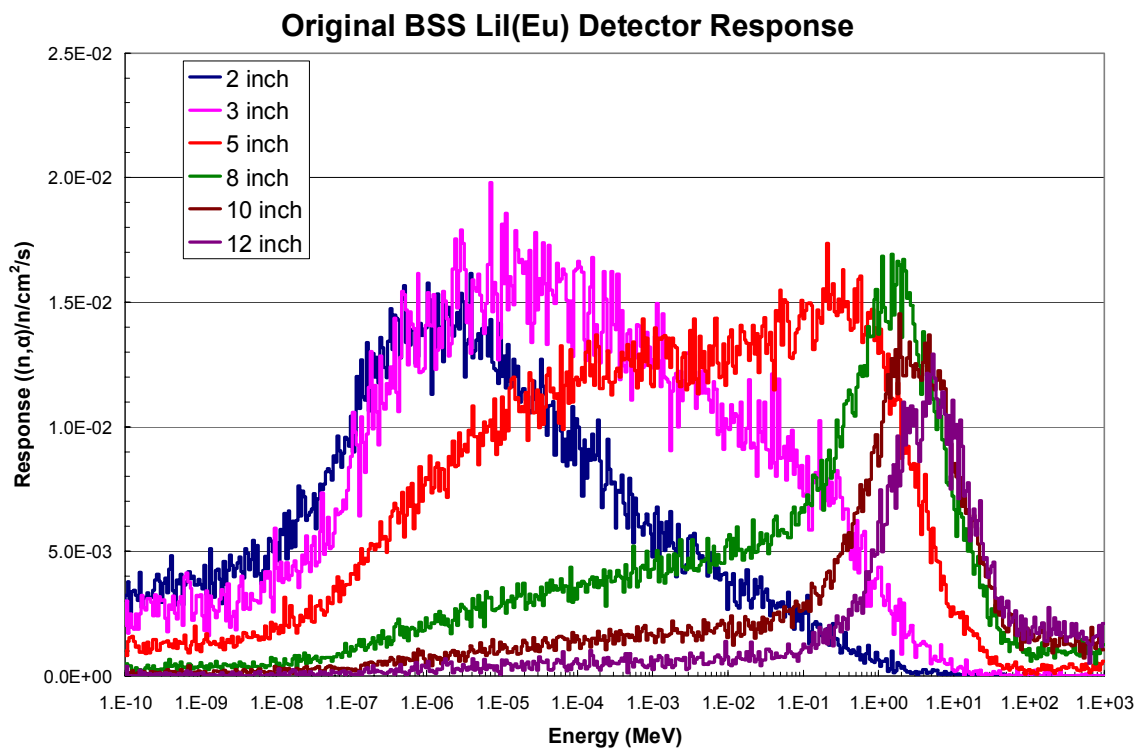


Figure 74. The response of the original BSS system is shown for the Z-direction neutron source for the LiI(Eu) detector.

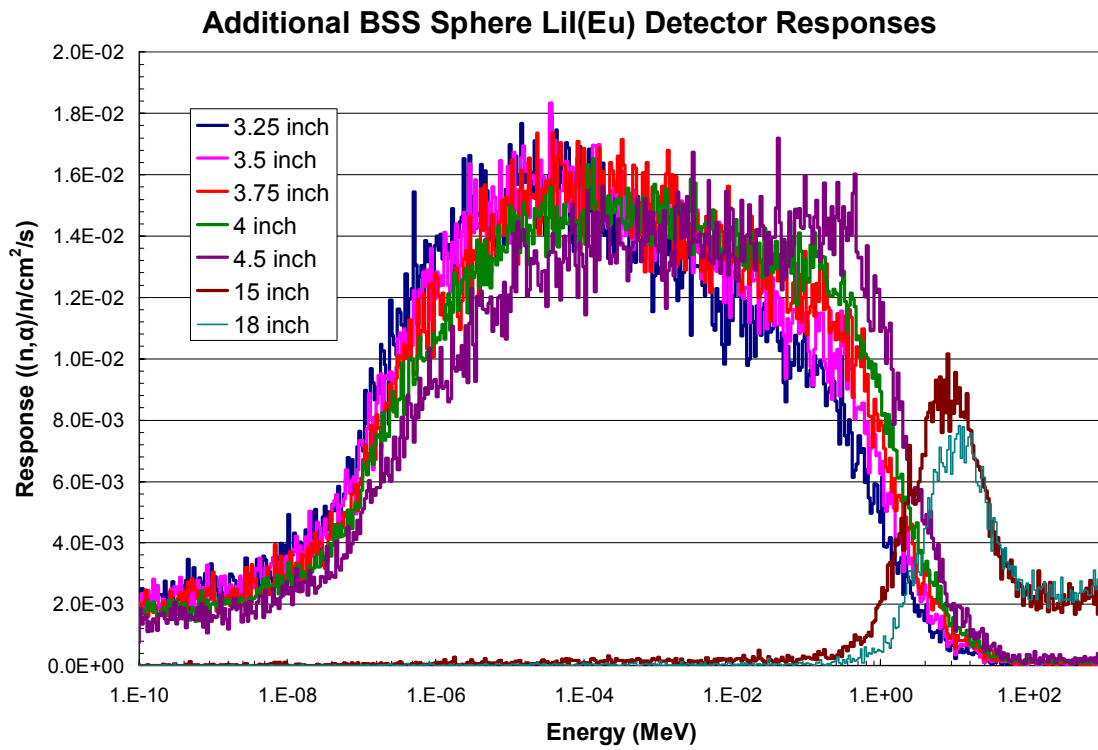


Figure 75. The response of the BSE polyethylene spheres and active LiI(Eu) detector is shown for the Z-direction neutron irradiation.

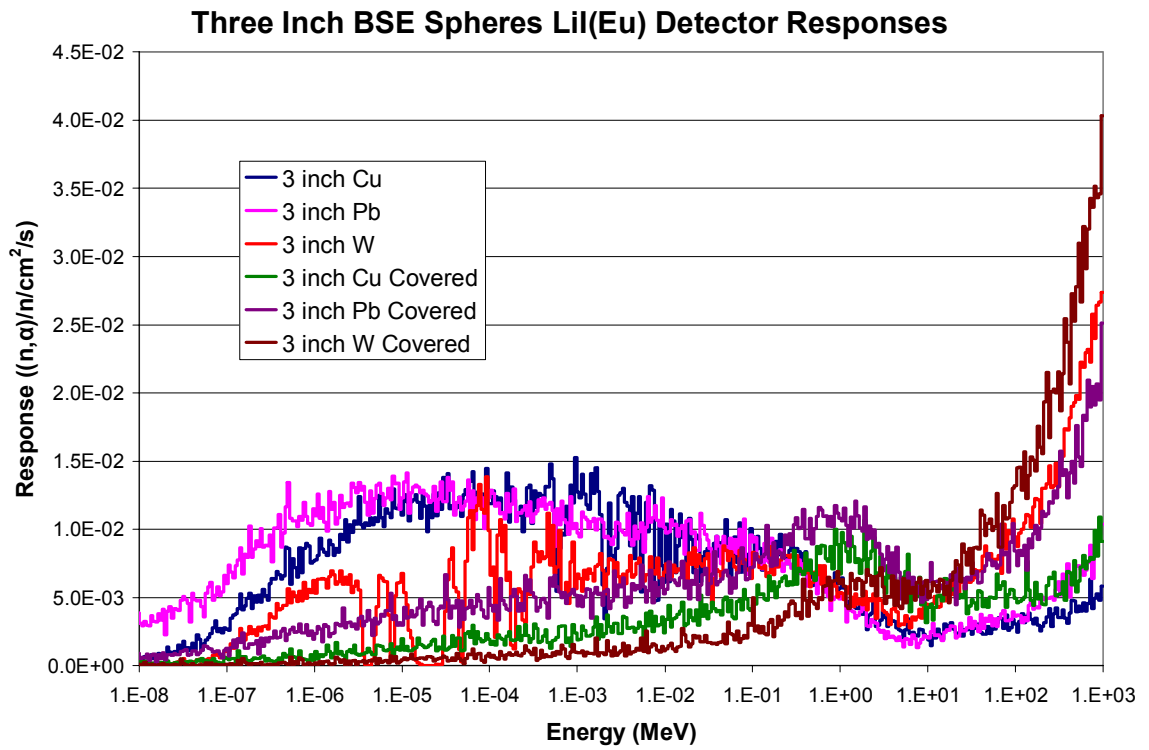


Figure 76. The small assembly (three inch inner sphere) BSE spheres active LiI(Eu) detector response for the Z-direction neutron source.

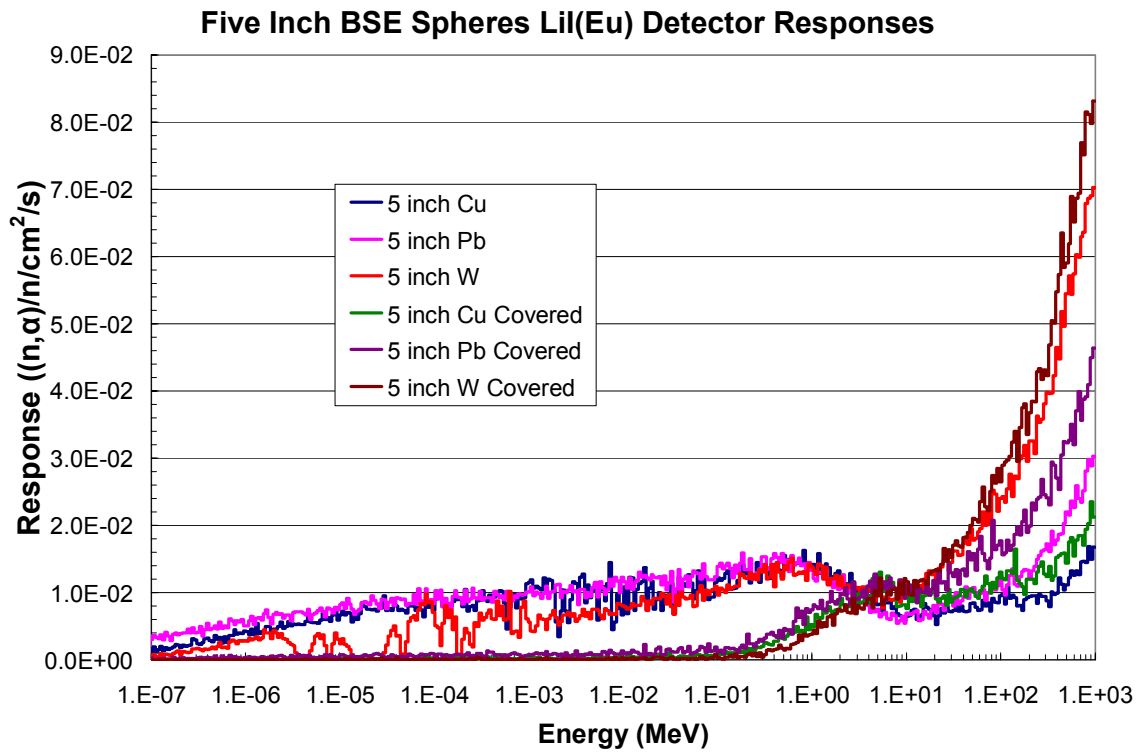


Figure 77. The large assembly (five inch inner sphere) BSE spheres active LiI(Eu) detector response for the Z-direction neutron source.

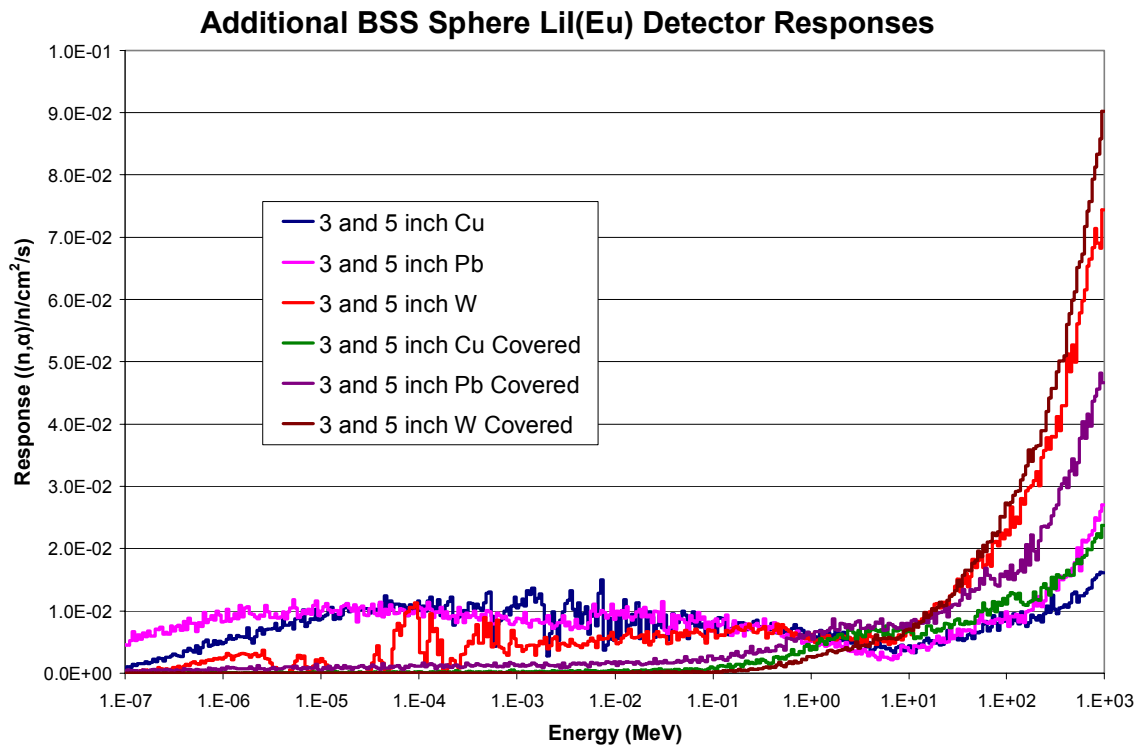


Figure 78. The BSE LiI(Eu) detector system is shown which utilizes both the 3” and 5” shells simultaneously for the Z-direction neutron source.

YZ-Directional Responses

In this portion of the appendix, the active LiI(Eu) detector response data will be presented for the YZ-direction neutron field. As before the data is shown as the reaction rate (n,α) per unit neutron fluence as a function of neutron energy. These responses are shown in Figure 79 through Figure 83.

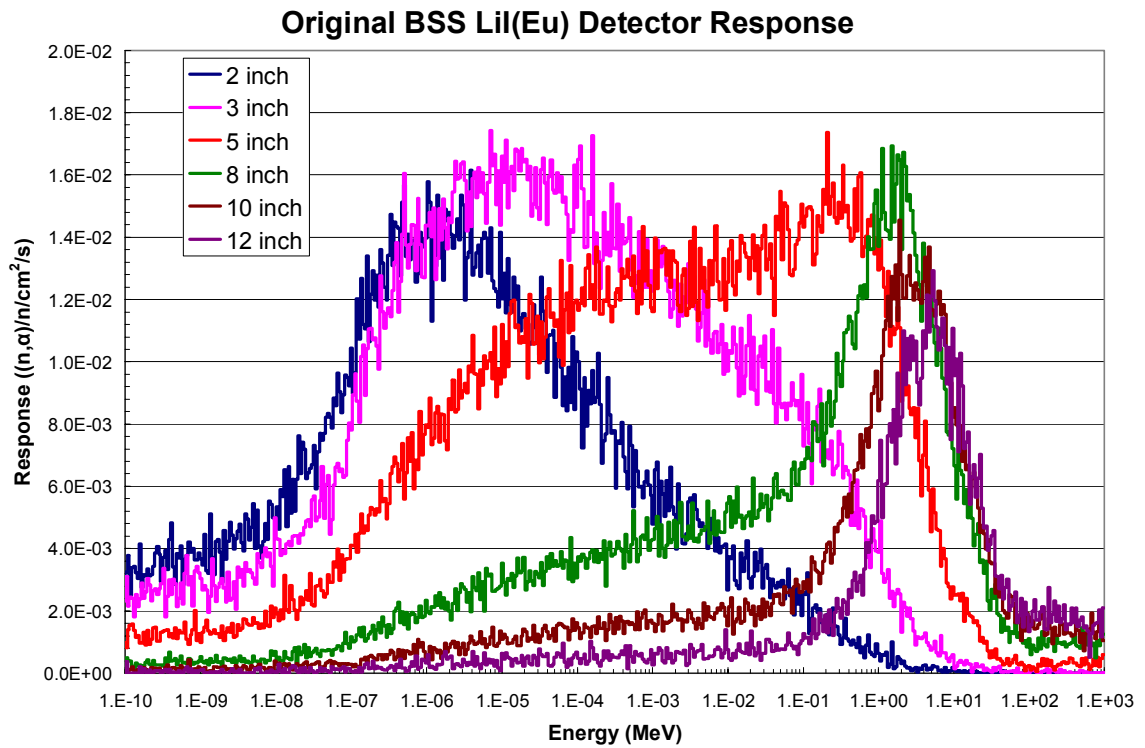


Figure 79. The response of the original BSS system is shown for the YZ-direction neutron source with the active LiI(Eu) detector.

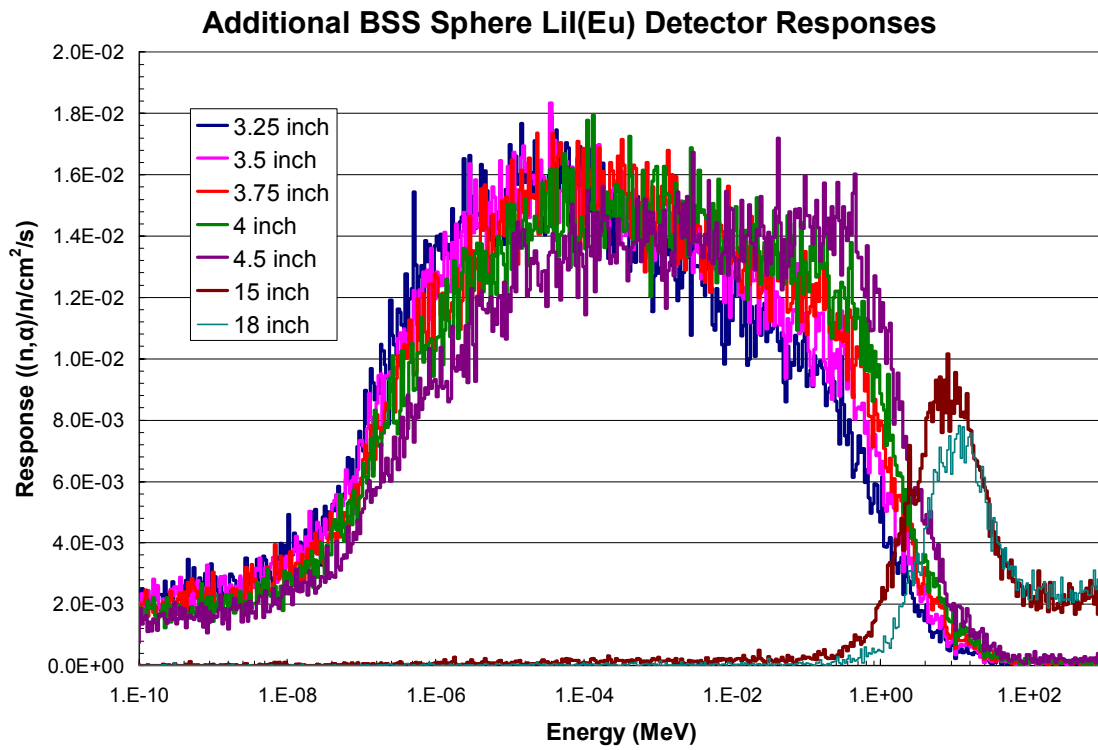


Figure 80. The response of the BSE polyethylene spheres and active LiI(Eu) detector is shown for the YZ-direction neutron irradiation.

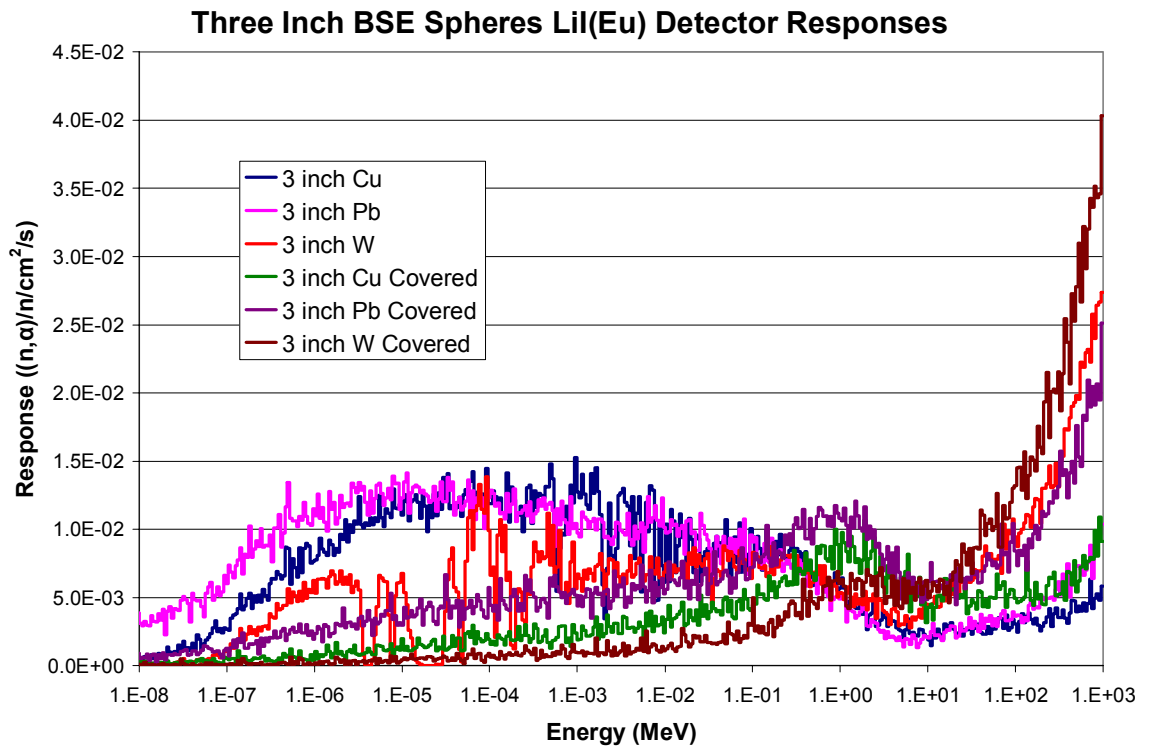


Figure 81. The small assembly (three inch inner sphere) BSE spheres active LiI(Eu) detector response for the YZ-direction neutron source.

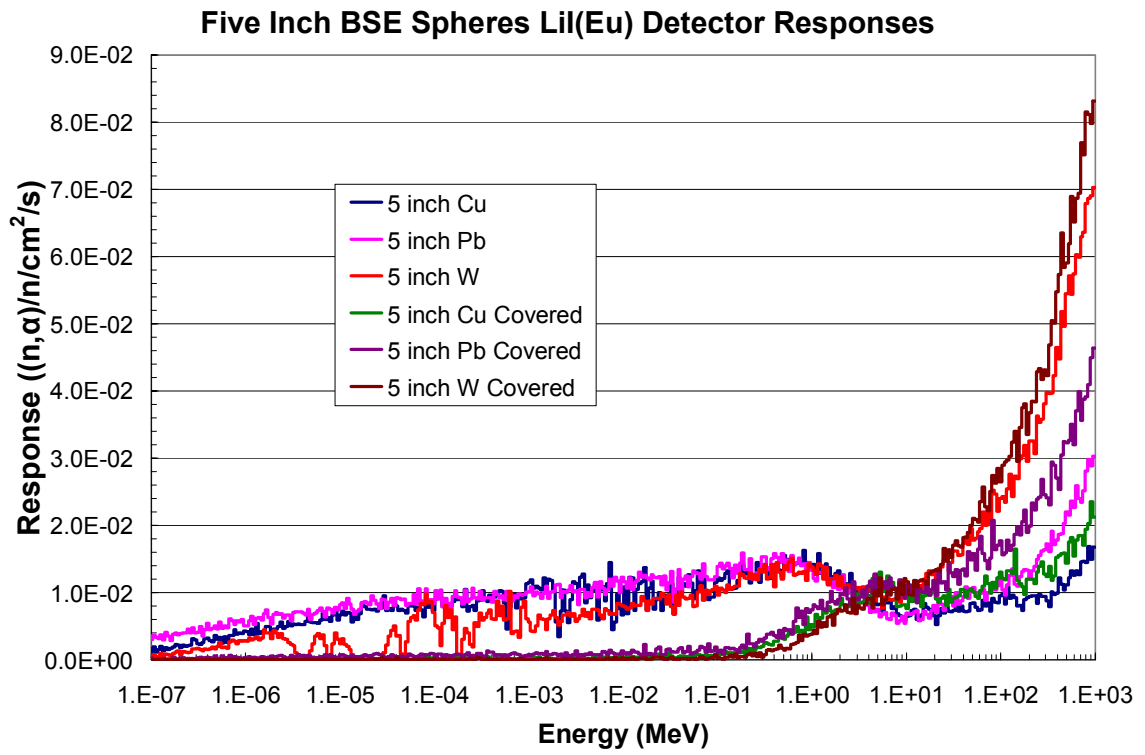


Figure 82. The large assembly (five inch inner sphere) BSE spheres active LiI(Eu) detector response for the YZ-direction neutron source.

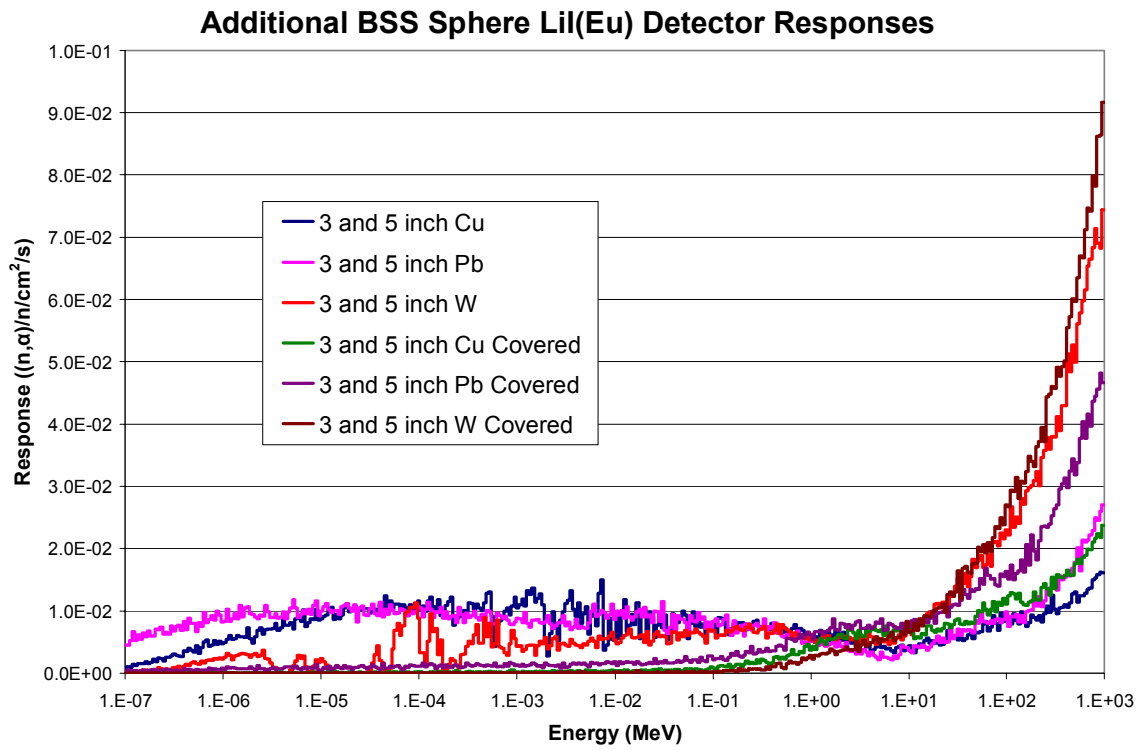


Figure 83. The BSE active LiI(Eu) detector system is shown which utilizes both the 3” and 5” shells simultaneously for the Z-direction neutron source.

APPENDIX C

FLUENCE RATE NORMALIZATION

The fluence rate unfolding process described above was normalized in the following fashion. The TOF data was obtained from the WNR staff. This provided a total fluence over a given run. This fluence was divided by the area of the detector which is 181.45 cm^2 . For the July 2007 measurements, this area was corrected by the 0.877 correction factor to account for partial illumination of the fission foil. This provides units of neutrons per square centimeter. Dividing this number by the number of fission counts recorded by the TOF system produces units of neutrons per square centimeter per fission count. To convert to lethargy fluence rate, the previous fluence rate is divided by the natural logarithm of the ratio of the upper and lower bin energies. This can be seen in Equation 13 through Equation 15

In a similar manner, the fluence rate per proton can be calculated. The number of micropulses that were sent through target 2 is logged in the TOF data. 98% of these pulses^{li} hit target 4. Using 3×10^8 protons per micropulse, the neutron fluence rate can be found per proton. This is done by dividing the total fluence by the area as before applying the 0.877 correction factor for the July measurements. This produces units of neutrons per cm^2 . This number is then divided by the total number of micropulses, and the number of protons per micropulse. This produces units of neutrons per centimeter squared per proton. This can be seen in Equation 16 and Equation 17. This unit is useful for comparison to the MCNPX results since they are normalized to a unit proton source.

The MCNPX results can be scaled to match the TOF system in a similar manner. This is done by multiplying by the number of protons per fission count. Since the units

of the MCNPX solutions are in neutrons per square centimeter per source proton, the units cancel and the remaining units are neutrons per square centimeter per fission count.

This number was found experimentally to be 8.86×10^{11} protons/fission count

$$Total_fluence(n(E)) \times \frac{1}{FC_foil_area(cm^2)} = \frac{fluence_rate}{unit_area} = \frac{n(E)}{cm^2}$$

Equation 13. The energy dependant fluence rate per unit area.

$$\frac{fluence_rate}{unit_area} \times \frac{1}{\#of_Fission_Counts} = \frac{n(E)}{cm^2 / FC}$$

Equation 14. The energy dependant fluence rate per unit area per fission count.

$$\frac{fluence_rate(E)}{unit_area / FC} \times \frac{1}{\ln\left(\frac{E_g}{E_{g+1}}\right)} = \frac{n}{cm^2 / FC / \Delta U}$$

Equation 15. The energy dependant fluence rate per unit area per fission count per unit lethargy.

$$\frac{fluence_rate}{unit_area} \times \frac{1}{\#of_micropulses} \times \frac{1}{\#of_protons / micropulse} = \frac{n(E)}{cm^2 / p}$$

Equation 16. The energy dependant fluence rate per unit area per proton.

$$\frac{fluence_rate(E)}{unit_area / p} \times \frac{1}{\ln\left(\frac{E_g}{E_{g+1}}\right)} = \frac{n}{cm^2 / p / \Delta U}$$

Equation 17. The energy dependant fluence rate per unit area per proton per unit lethargy.

APPENDIX D

GOLD FOIL RESPONSE COMPARISONS

In this section a comparison between the different irradiation geometries will be presented. Since the gold foil is optically thin in the Y-direction case, and the incident flux is highly anisotropic, the response is lower for this direction. This can be seen in the following figures. It should be noted that the low energy spheres have insignificantly small responses at the higher energies, and therefore large variations have little effect. The same holds true for the high energy spheres have insignificantly small responses in the low energy region and large variations here have little effect.

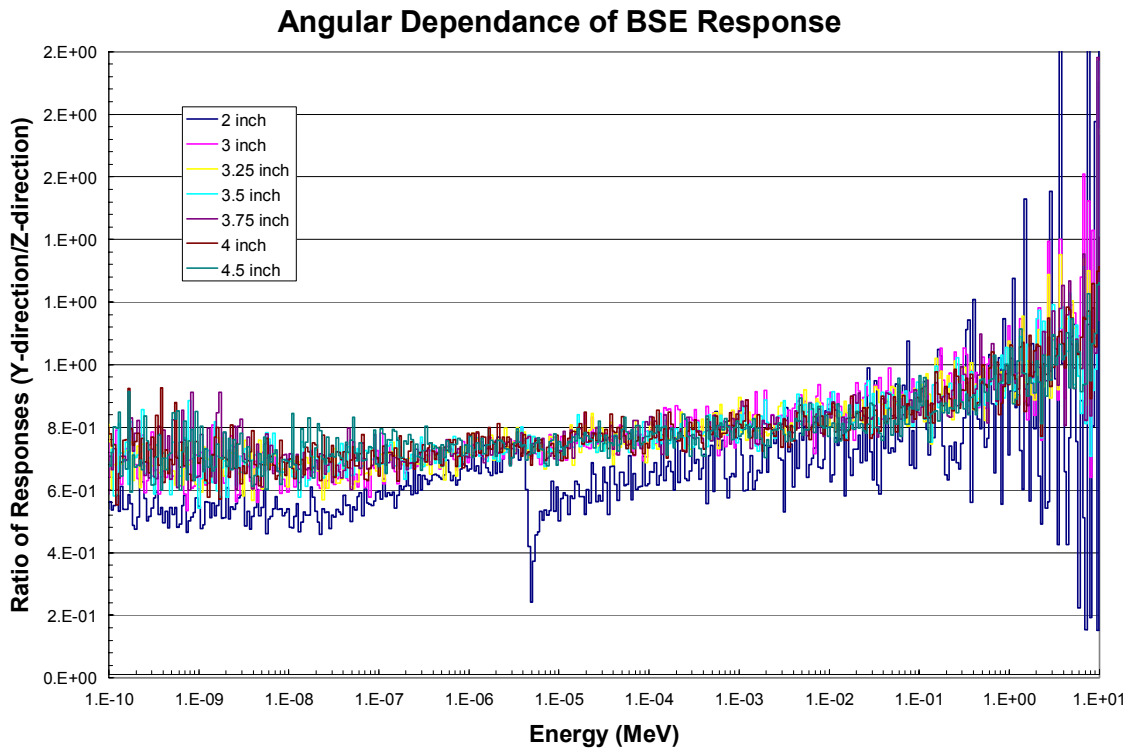


Figure 84. The ratio of the angular response of the low energy spheres.

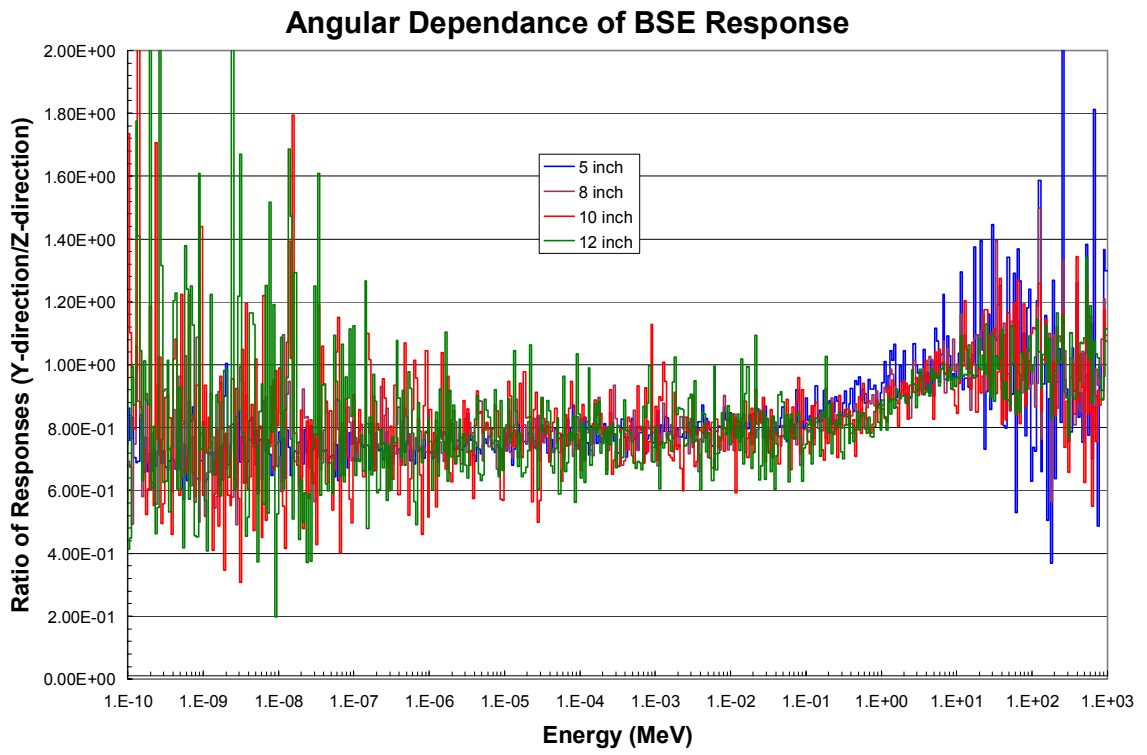


Figure 85. The ratio of the angular response of the intermediate energy spheres.

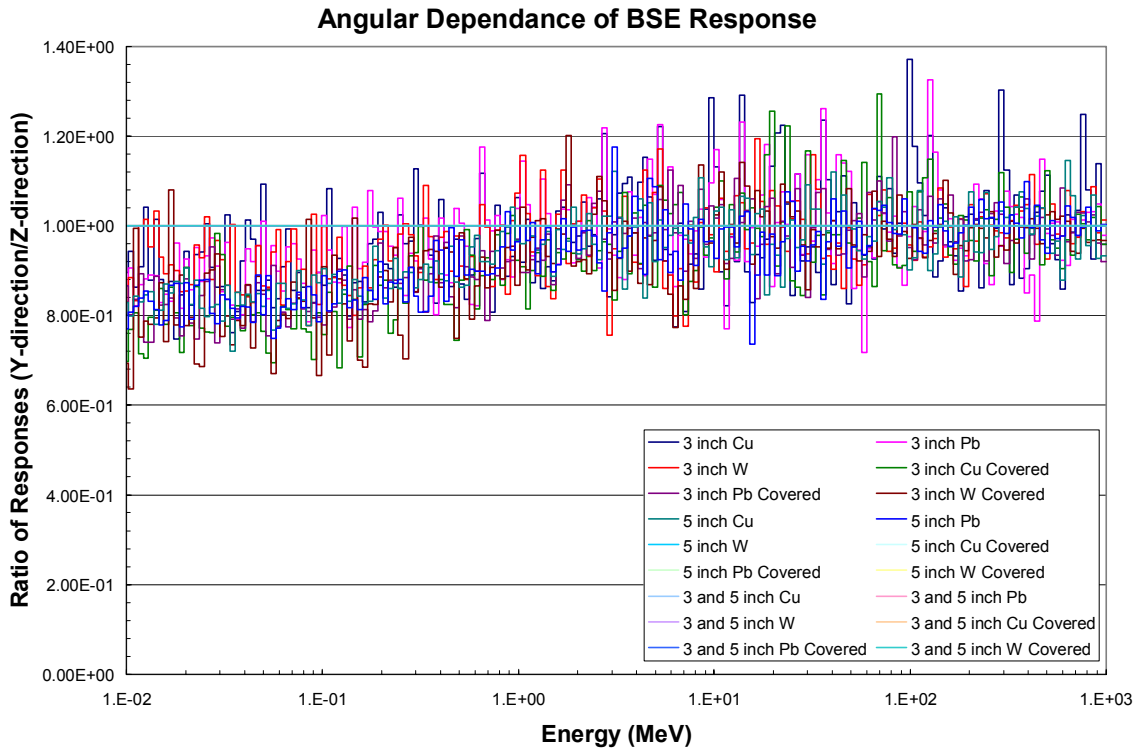


Figure 86. The ratio of the angular response of the high energy spheres.

REFERENCES

- ⁱ Glasstone, S., Sesonske, A., **Nuclear Reactor Engineering** Van Nostrand Reinhold Company 1967 pg 92.
- ⁱⁱ Thwaites, D., Tuohy, J., *Back to the Future: The History and Development of the Clinical Linear Accelerator. Physics in Medicine and Biology* 51 pg R343-R362 (2006).
- ⁱⁱⁱ T-2 ENDF-VII evaluation of Li-6 cross section available from <http://t2.lanl.gov>.
- ^{iv} R.L. Bramblett, R. I. Ewing, and T. W. Bonner, "A New Type of Neutron Spectrometer." *Nuclear Instruments and Methods* 9, pg 1-12 (1960).
- ^v Ludlum Model 42-143 neutron ball cart Manual.
- ^{vi} Centronics SP9 3He tube detector.
- ^{vii} J.W. Leake, *Nuclear Instruments and Methods* 63, 329 (1968).
- ^{viii} Johnson, T. L., Lee, Y., Lowry, K. A., Gorbics, S. G., "Recent Advances in Bonner Sphere Neutron Spectrometry", Proceedings Theory and Practices in Radiation Protection and Shielding Symposium, Knoxville, TN, pp. 83-84, (1987).
- ^{ix} N. E. Hertel and J. W. Davidson, "The Response of Bonner Spheres from Thermal Energies to 17.3 MeV", *Nuclear Instruments and Methods* A238, 509-516 (1985).
- ^x Olko, P., et. al. "Modeling of the Thermoluminescence Response of LiF:Mg,Cu,P (MCP-N) Detectors After Doses of Low Energy Photons" *Radiation Protection Dosimetry* 84 pg 103-108 (1999)
- ^{xi} Sweezy, J., Hertel, N., Veinot, K., Karam, R. "Performance of Multisphere Spectrometry Systems" *Radiation Protection Dosimetry* 78 pg 263-272 (1998).
- ^{xii} Y. Uwamino, et al., "Two Types of Multi-Moderated Neutron Spectrometers: Gamma-ray Insensitive Type and High-Efficiency Type" *Nuclear Instruments and Methods* 239 pg 299 (1985).
- ^{xiii} Thomas, D.J., Bardell, A.G., Macaulay, E.M., "Characterisation of a Gold Foil Based Bonner Sphere Set and Measurements of Neutron Spectra at a Medical Accelerator" *Nuclear Instruments and Methods* 476 pg 31-35 (2002).
- ^{xiv} Wang, Z, et al. "Study of a Gold Foil Based Multisphere Neutron Spectrometer" *Radiation Protection Dosimetry*. pg 1-5. (2007).
- ^{xv} Awschalom, M., Sanna, R.S., "Applications of Bonner Sphere Detectors in Neutron Filed Dosimetry," *Radiation Protection Dosimetry*, Volume 10 No 1-4. Pg 89-101, (1985).
- ^{xvi} Wang, C.K., Blue, T.E., "A Neutron Spectrometer for Neutrons with Energies Between 1 eV and 10 keV" *Nuclear Instruments and Methods* 290 1 Pg 237-241. (1990).
- ^{xvii} Curtiss, L., **Introduction to Neutron Physics** D. Van Nostrand Company Inc.(1959)
- ^{xviii} Forbes, S.G., *Phys. Rev.* 88, pg 1309 (1952).
- ^{xix} Kuijpers, L., et al., *Nuclear Instruments and Methods*. 144 pg 215 (1977).
- ^{xx} Ing, H., et al. "ROSPEC – A Simple Reliable High Resolution Neutron Spectrometer" *Radiation Protection Dosimetry* 70 pg 273-278 (1997).

-
- xxi ICRP-74 “Conversion Coefficients for use in Radiological Protection Against External Radiation, **ICRP Publication 74** Pergamon Press, Oxford (1996).
- xxii Birattari, C. Ferrari, A., Nuccetelli, C., Pelliccioni, M., Silari, M., *Nuclear Instruments and Methods* **297** pg 250 (1990).
- xxiii Olsher, R.H., et al. “WENDI: An Improved Neutron Rem Meter.” *Health Physics* **79-2** pg 170-181 (2000).
- xxiv Olsher, R.H., et al. “PRESCILA: A New, Lightweight Neutron Rem Meter”.
- xxv Model REM 500 Neutron Survey Meter Manual Revision A, September 1998.
- xxvi Wiegel, B., Alevra, A.B., “NEMUS – The PTB Neutron Multisphere Spectrometer: Bonner Spheres and More.” *Nuclear Instruments and Methods* **476** pg 36-41 (2002).
- xxvii Glasstone, B., Edlund, M., **The Elements of Nuclear Reactor Theory** D. Van Nostrand Company Inc. 1952.
- xxviii Birattari, C. Ferrari, A., Nuccetelli, C., Pelliccioni, M., Silari, M., *Nuclear Instruments and Methods* **297** pg 250 (1990).
- xxix Wiegel, B., Alevra, A.B., “NEMUS – The PTB Neutron Multisphere Spectrometer: Bonner Spheres and More.” *Nuclear Instruments and Methods* **476** pg 36-41 (2002).
- xxx Johnson, L.L., Lee, Y, Lowry, K.A., Gorbics, S.G., “Recent advances in Bonner Sphere Neutron Spectrometry.” Presented at **Theory and Practices in Radiation Protection and Shielding Symposium**, Knoxville, TN, Pg. 83-84, 1987.
- xxxi Reginatto, M. “The “Few Channel” Unfolding Programs in the UMG Package” MXD_FC33, GRV_FC33, and IQU_FC33 for UMG Package 3.3 released March 1st, 2004”.
- xxxii Reginatto, M., Goldhagen, P., “MAXED, A Computer Code for the Deconvolution of Multisphere Neutron Spectrometer Data Using the Maximum Entropy Method”, **USDOE report EML595** (1998).
- xxxiii Reginatto, M., Goldhagen, P., “MAXED, A Computer Code for Maximum Entropy Deconvolution of Multisphere Neutron Spectrometer Data”, *Health Physics* **77** (1999).
- xxxiv Reginatto, M., Goldhagen, P., Neumann, S., “Spectrum Unfolding, Sensitivity Analysis and Propagation of Uncertainties with the Maximum Entropy Deconvolution Code MAXED” *Nuclear Instruments and Methods* **476** (2002).
- xxxv Ludlum Model 42-5 Neutron Ball Cart Manual March 1989.
- xxxvi Wiegel, B., et al., ”Spectrometry using the PTB Neutron Multisphere Spectrometer (NEMUS) at Flight Altitudes and at Ground Levels” *Nuclear Instruments and Methods* **476** pg 52-57 (2002).
- xxxvii Knoll, Glenn, **Radiation Detention and Measurement** 3rd edition (2000).
- xxxviii GammaVision Pacakge Users Manual 1998.
- xxxix Wender, S.A., et al. “A Fission Ionization Detector for Neutron Flux Measurements at a Spallation Source” *Nuclear Instruments and Methods* **336** pg 226-231 (1993).

-
- ^{xi} Personal communication Art Bridge 2007.
- ^{xli} Geant4 Developments and Applications, J. Allison et al., IEEE Transactions on Nuclear Science **53** No. 1 (2006) 270-278.
- ^{xlii} Geant4 - A Simulation Toolkit, S. Agostinelli et al., Nuclear Instruments and Methods **A 506** (2003) 250-303.
- ^{xliiii} N.V. Mokhov, S.I. Striganov, A. Van Ginneken, S.G. Mashnik, A.J. Sierk and J. Ranft, MARS Code Developments, Fermilab-Conf-98/379 1998; LANL Report LA-UR-98-5716 (1998); nucl-th/9812038 v2 16 Dec 1998.
- ^{xliv} Fasso`, A., Ferrari, A., Ranft, J., Sala, P.R., "**FLUKA: a multi-particle transport code**", CERN-2005-10 (2005), INFN/TC_05/11, SLAC-R-773.
- ^{xliv} Fasso`, A., et al., "**The physics models of FLUKA: status and recent developments**", Computing in High Energy and Nuclear Physics 2003 Conference (CHEP2003), La Jolla, CA, USA, March 24-28, 2003, (paper MOMT005), eConf C0303241 (2003), arXiv:hep-ph/0306267.
- ^{xlvi} Gregg W. McKinney et al., "MCNPX 2.6.X Features (2006-2007)", LA-UR-07-2053 (272 KB), M&C/SNA 2007 Conference Workshop, Monterey, CA, April 15-19, 2007.
- ^{xlvii} Hendricks, J., et al. "MCNPX, Version 26E", **LA-UR-07-6632** november 17th, 2007.
- ^{xlviii} M. B. Chadwick, P. G. Young, S. Chiba, S. C. Frankle, G. M. Hale, H. G. Hughes, A. J. Koning, R. C. Little, R. E. MacFarlane, R. E. Prael, and L. S. Waters, "Cross Section Evaluations to 150 MeV for Accelerator-Driven Systems and Implementation in MCNPX," *Nuclear Science and Engineering* 131, Number 3 (March 1999) 293.
- ^{xliv} Drawings 14-11, 14-29, 12-38, 7014-376, 7014-399 by Ludlum Inc.
- ^l Ziegler, J. F. Biersack, J. P., and Littmark, U. (1985). *The Stopping and Range of Ions in Solids*. Vol. 1 of *The Stopping and Ranges of Ions in Matter* (Pergamon Press, New York).
- ^{li} Fotiadis, Nikolia Personal Communication 2007.
- ^{lii} User Facility Administrators, Brookhaven National Laboratory, BNL.
http://www.bnl.gov/nufo/images/facilities/Lansce_lg.jpg (accessed March 2007).
- ^{liii} Lisowski, P.W., et. al. "The Los Alamos National Laboratory Spallation Neutron Sources," *Nuclear Science and Engineering*, **106** pg 208-218 (1990).
- ^{liv} Regiatto, M. Personal Communication 2005.